RELIABILITY AND ROBUSTNESS OF DIRECT TORQUE CONTROLLED PERMANENT MAGNET SYNCHRONOUS MACHINES

By

Ibrahim M. Allafi

A DISSERTATION

Submitted to
Michigan State University
in partial fulfillment of the requirements
for the degree of

Electrical and Computer Engineering - Doctor of Philosophy

2023

ABSTRACT

Permanent magnet synchronous machines (PMSMs) are widely used in various industries such as transportation, manufacturing and renewable energy. The simple structure of direct torque control (DTC) coupled with its encoderless operation and fast dynamics are of great interest for PMSMs. Nevertheless, the occurrence of faults, such as turn-to-turn short circuit, high resistance contact, static eccentricity and partial demagnetization, remains a concern. Faults can prevent smooth drive operation of DTC and potentially lead to catastrophic losses if not detected and mitigated in their early phases. Hence, fault diagnosis of DTC driven PMSMs is paramount to ensuring reliable drive operation.

An essential aspect of developing effective fault diagnosis is to understand the impact of faults on drive operation and its corresponding reaction. A comprehensive examination of the nonlinear behavior of flux and torque hysteresis comparators in DTC driven PMSMs provides insight. It is shown that DTC can tolerate low-severity faults within the controller bandwidth while continuing to operate normally. However, when flux and torque errors exceed the bandwidth, DTC counteracts by introducing negative sequence voltages and torque angle variations which impacts fault diagnosis and control under faulty conditions.

Many existing fault diagnosis methods are based on field oriented control (FOC); however, it is not well understood how these methods translate to DTC driven PMSMs. Machine Voltage Signature Analysis (MVSA) is the most commonly used approach for fault diagnosis in electric machines. However, the use of DTC introduces challenges for adoption MVSA due to its nature of compensation, structure and regulation principle. A novel fault diagnosis approach for DTC driven PMSMs is developed. This approach maintains the simple structure of DTC, removes the need for complex signal processing tools, and relies solely on the available signals in the drive. The occurrence of faults results in unique deviations in the

direction and magnitude of the commanded voltages in the stator flux linkage (MT) frame enabling fault detection, classification, and severity assessment.

Ultimately, the fault diagnosis algorithm used for inverter driven PMSMs should be effective and applicable irrespective of the control type. A comprehensive fault diagnosis approach is developed based on active and reactive power signature analysis. This data driven algorithm uses spectral components of the power signals as fault indicators. It is shown that this developed algorithm is capable of fault diagnosis in both FOC and DTC driven PMSMs.

The reliability of inverter driven PMSMs depends on the ability to monitor its state of health during operation. It is necessary to detect that a fault occurred, identify fault type as well as estimate its severity. Classification algorithms are used to separate fault types and estimate fault severity. Here, the performance of three classification algorithms is evaluated for inverter driven PMSMs. The classification algorithms are linear discriminate analysis (LDA), k-nearest neighbor (k-NN), and support vector machines (SVM). The SVM classifier is shown to be a highly effective method for detecting and classifying faults in PMSMs controlled by either drive, even with limited training data and high noise levels.

This Dissertation is dedicated to the memory of my beloved mother, Nayfeh Gharaibeh who helped me throughout my life. I would like also to dedicate this work to my wife, Asala Altawiel. My motivation and inspiration came from her patience and support. There would have been no success without both of you.
A sincere gratitude to my loving father, Mahmood Allafi, and my family members, Amany, Mohammed, and Mustafa, who offered me unwavering love and support during my study.

ACKNOWLEDGMENTS

First and foremost, I praise God for blessing me with this opportunity to be where I am today and for giving me the health, ability, and strength to succeed.

I would like to express my special appreciation and thanks to my research advisor, Professor Shanelle N. Foster, for her support, assistance, guidance, and motivation to earn my doctorate and grow as a scholar and researcher. Also, I would like to thank the members of my graduate committee; Prof. Guoming Zhu, Prof. Selin Aviyente, and Prof. Joydeep Mitra, for their guidance, insights, and support. I would also like to express my sincere appreciation to Professor Elias Stranags, whose guidance and experience helped me master the skills needed for my growth as an engineer.

A special thanks to my colleagues at Michigan State University from the Electric Machines and Power Electronics Research (EMPowER) Laboratory. I am grateful to have had the opportunity to meet these amazing people, who helped me during my studies at the Graduate School. I would like to thank Dr. Steve Hayslett, Dr. William Jensen, Dr. Shaopo Huang, Dr. Thang Pham, Matt Meier, Tiraruek Ruekamnuaychok, Prathima Nuli, Mathis Allen, Orwell Madovi, Bhuvan Khoshoo, and Khan Jazib Islam. Their help, support, and advice made this work possible.

I would also like to thank Karl Dersch, Roxanne Peacock, Christina Kent, Brian Wright, Meagan Kroll, Laurie Rashid, Lisa Clark, and Michelle Stewart from the ECE department at Michigan State University for all of their assistance. Additionally, I would like to thank the Jordan University of Science and Technology for their financial support during my study.

This endeavor would not have been possible without the assistance and encouragement from my friend, Saad Alzahrani. Words cannot express my gratitude to you.

I would like to thank my father and my family members, who encouraged me to start my

Ph.D. and continue to support me throughout my future goals and career. Without their unending support, I never would have made it this far.

Last but not least, I am deeply indebted to my wife, Asala Altawiel. I could not have undertaken this journey without you. I am more grateful to you than you will ever know.

TABLE OF CONTENTS

LIST OF TABLES

LIST OF FIGURES

Chapter 1

Introduction

Highly reliable and efficient electric driven permanent magnet synchronous machines (PMSMs) are required for critical applications where safety is a compulsory part of their operation. However, due to the limitations of material lifetime, assembly defects, poor installation, or improper operation, an unexpected malfunction may happen and can lead to production shutdowns and catastrophic loss in human lives [1, 2]. Therefore, health monitoring and fault identification algorithms should be integrated into the inverter driven PMSMs for improved safety and enhanced reliability. It is worth noting that the compensating nature of the electric drive system impacts fault detectability [3].

The two most common drives for PMSMs are Field oriented control (FOC) and Direct torque control (DTC). Both control schemes have a simple structure and provide satisfactory performance; however, FOC offers better steady-state behaviour and DTC provides faster torque dynamics. The selection of the appropriate control scheme is based on the drive requirements for the desired application.

Different types of health monitoring techniques for electric machines are applied in the field:

- Electrical Monitoring through voltage, current, or power signals [3–10]
- Mechanical Monitoring through accelerometer or proximity probes [11–13]
- Thermal Monitoring through thermocouple sensors or thermography [14–16]
- Flux Monitoring through airgap, leakage, or stray magnetic flux [17, 18]
- Chemical Monitoring through tagging compound [19]

Electrical monitoring of the machine receives increasing attention from academia and industry due to its low implementation cost and continuous/remote monitoring capability in comparison with the other monitoring types. Several electrical monitoring techniques are proposed in the literature for FOC driven PMSMs considering single or multiple fault occurrence [4–8]. However, fault diagnosis methods of PMSMs that exist in the literature based on the FOC scheme may not be suitable for DTC driven PMSMs as they have different compensation nature, structure, and regulation principle.

The motor voltage or current signature analysis (MVSA/MCSA) is widely adopted at high loads for the most accurate fault diagnosis at different operating conditions. The advantage of this technique is that it does not require any additional hardware for implementation and the machine monitoring can be done remotely through the Motor control Center (MCC). The sideband harmonics in stator current are used as features to detect turn-to-turn short circuit (TTSC) fault in [8] and to detect eccentricity fault in [20]. However, the detection accuracy degrades at high noise levels since the features used have low signal-to-noise ratio (SNR). In order to use detection indicators with higher SNR, the main spectral components in the commanded phase voltage or measured phase current are selected to detect and classify TTSC, eccentricity, and demagnetization faults using linear discriminate analysis (LDA) classifier [4]. Although the results are promising, the present harmonics in stator current waveform are heavily dependent on the controller bandwidth [1,3]. If the controller is able to attenuate them due to high bandwidth, they will vanish in the stator current signal and be imposed in the voltage signal. Therefore, the detection accuracy becomes a function of the selected bandwidth and the selected signal for detection. Additionally, this approach could not be implemented for DTC since the amplitude variations in the spectrum are affected by the variable switching frequency in DTC under different faults.

Authors in [6] use the transform coefficients based on the short time Fourier transform and wavelet analysis of the torque producing current in dq frame to detect and classify three faults: TTSC, high resistance contact (HRC), and missing gear tooth. However, this approach is not applicable for DTC as signals in dq frame are not available. According to [5], the shift in commanded dq-voltages can be used to detect and separate between TTSC, eccentricity, and demagnetization faults. These voltage signals are readily available in the FOC drives and their magnitude variation under different faults could be utilized in a non-intrusive diagnosis method. Once again, this approach could not be extended to DTC since the drive is implemented in the stationary ($\alpha\beta$) frame where the position signal is not required. Therefore, the dq-voltages are not always available in DTC drives. Moreover, the dq-voltages shift in FOC under different faults, whereas the currents are assumed to be fixed and regulated to follow the dq-current commands. While in DTC, the currents are not assumed to be constant and vary under different faults. Hence, fault diagnosis techniques developed for FOC driven PMSMs are not applicable for DTC; indicating there is an immense need for condition monitoring in the DTC driven PMSMs.

Few recent investigations explore condition monitoring for DTC driven PMSMs [1,21,22]. Authors in [21] suggest using the magnitude and initial phase of the zero-sequence voltage component (ZSVC) to detect TTSC fault. A torque injection and improved flux observer are then proposed to tolerate the TTSC effect on DTC performance. However, neutral point access is needed to compute the zero sequence network by adding three-phase resistors in parallel with the motor-inverter connections. HRC fault is identified in [22] by imposing a constant flux offset in the flux estimation loop of a DTC driven PMSMs. Since DTC relies on the flux estimation, additional analysis is required to guarantee stable DTC operation. Although DTC is proposed as the next generation of universal ac motor drives, it is evident

that the reliability of DTC driven PMSMs is not thoroughly investigated in the literature and fault diagnosis becomes a necessity to improve the drive performance under faulty operation.

1.1 Objectives & Contributions

Faults manifest themselves in the drive signals in inverter driven PMSMs. The fault types can result in distinct or similar trends. Proper utilization of these trends assists in fault detection, classification, and severity estimation. However, the hysteresis comparators in DTC pose challenges in fault detection and separation for PMSMs. The compensating nature of DTC and variations in the switching frequency, determined by the hysteresis band, may result in unobservable fault effects in DTC drives. Consequently, the faulty operation of DTC driven PMSMs may turn out to be unstable control if the faults are not detected and mitigated properly at their premature stages. Condition monitoring techniques are required for DTC driven PMSM in order to maintain a safe and reliable drive operation.

This work addresses the research gap in reliability and robustness of DTC driven PMSM under faulty conditions. The contributions of this work are:

- Identification and delineation of the challenges of adoption of several FOC based techniques for DTC driven PMSMs.
- Comprehensive understanding of the impact of faults on the operation of DTC driven PMSMs.
- Development of a non-intrusive fault identification and severity estimation algorithm suitable for the scheme of DTC driven PMSMs.
- Development of a comprehensive fault identification and severity estimation algorithm for inverter driven PMSMs irrespective of the control type.

1.2 Organization

Chapter 2 presents the theoretical background for PMSM modeling in stationary, stator flux linkage, and rotor flux linkage frames in healthy condition. These different PMSM models are used to design the drive systems and analyze machine operation under healthy and faulty conditions. The performance of PMSM driven by FOC and DTC is then studied and compared. The stator and rotor faults in PMSM are also discussed.

Chapters 3–6 are the core chapters of this work. Chapter 3 presents a comprehensive assessment of the impact of faults on DTC driven PMSM and the corresponding drive reaction to the fault occurrence. It provides in-depth explanation of the tolerance capability of DTC drive under fault conditions as well as its compensation response.

Chapter 4 presents the geometric model and the parameters for the tested machine. It also provides detailed electromagnetic modeling in FEA for the tested machine under healthy and faulty conditions. These models are then coupled with a drive circuit. The experimental implementation of the driven PMSM system under healthy and faulty conditions is then described.

Chapter 5 presents an analysis for the usage of the MVSA approach in fault diagnosis for PMSM driven by FOC and DTC. The supervised classification is discussed and then utilized in designing the diagnostic approach.

Chapter 6 discusses the faulty operation of DTC driven PMSM. Two diagnostic approaches are then proposed based on the power signature analysis and commanded voltage shifts in the stator flux linkage frame.

Finally, Chapter 7 brings the conclusions and future work of this dissertation.

Chapter 2

Theoretical Background

2.1 PMSM Modeling

The usage of PMSMs has immensely increased during the last three decades. This is due to the development of new magnets with high residual flux density, high energy product, and considerable demagnetization resilience, such as the Neodymium-Iron-Boron (NdFeB) magnet [23]. These magnets are used instead of windings to take over the rotor field production in the machine. Therefore, PMSMs achieve higher torque density, lighter rotor mass, and higher efficiency in comparison with induction machines [24, 25]. According to magnets location in the rotor design, PMSM can be categorized mainly into interior buried rotor magnets (IPMSM) or surface mounted rotor magnets (SPMSM). Fig. 2.1 shows both PMSM typologies.

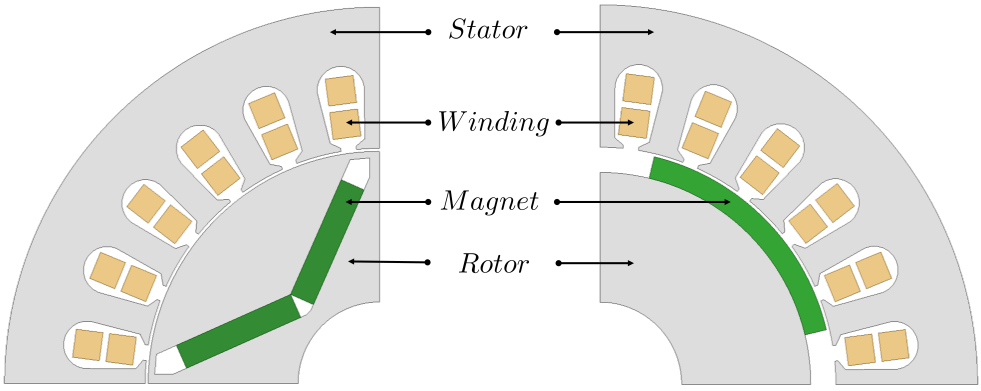

Figure 2.1: PMSM typologies: IPMSM(Left) and SPMSM(Right).

PMSMs utilize the reluctance torque caused by the rotor saliency in addition to the magnet torque. This results in obtaining a wider constant power speed range which is an important feature for high-speed applications. Such advantages make PMSMs more prevalent in different critical industries such as automotive, aerospace, and renewable energy applications [26].

The mathematical model of PMSM can be expressed in three different reference frames, namely, the stator flux linkage (MT) frame, the rotor flux linkage (dq) frame, and the stationary ($\alpha\beta$) frame [27, 28]. In the stator flux linkage frame, the M-axis is synchronized with the stator flux linkage vector ($\lambda_s \angle \theta_s$), and the T-axis refers to the torque component. In the rotor flux linkage frame, the d-axis is aligned with the magnet flux linkage vector ($\lambda_{PM} \angle \theta_r$), which lags the M-axis by the torque angle (δ). Fig. 2.2 shows these reference frames along with the stationary ($\alpha\beta$) frame where α-axis is fixed to the stator phase A-axis.

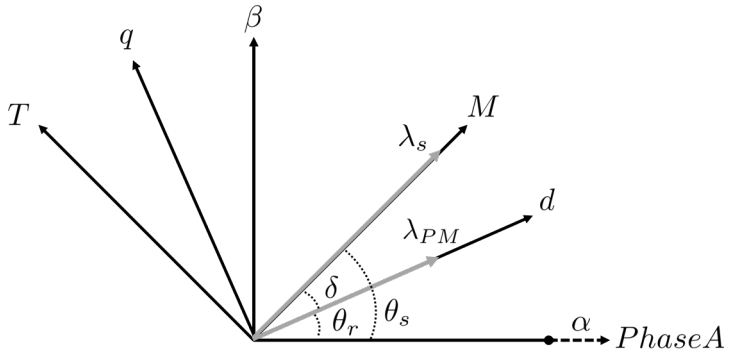

Figure 2.2: Vector diagram for rotor flux, stator flux, and stationary frames.

The PMSM models in the aforementioned frames can be generated through a transformation from a general PMSM model in a stator reference (ABC) frame, assuming the machine has three-phase winding connected in wye to a common neutral point. The stator winding in PMSM is typically distributed sinusoidally over the machine stator with a ($\frac{2\pi}{3} rad$) phase

shift between the three windings in order to have nearly sinusoidal back electromotive force (back-EMF). In the stator reference frame, electrical phase quantities can be visualized as they are fixed in space along their phase axes with time-varying magnitudes. Fig. 2.3 shows PMSM with sinusoidal distributed winding and the generated back-EMF.

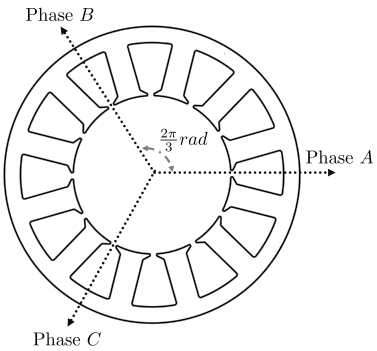

(a) Machine stator layout with sinusoidally distributed winding.

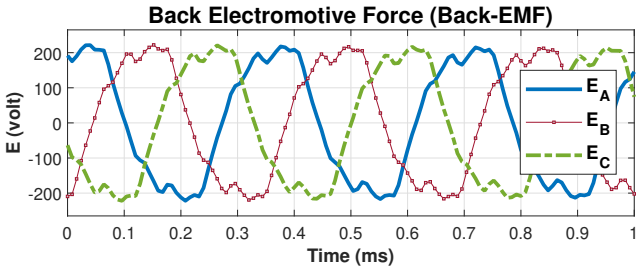

(b) Generated back-EMF of the three phase winding.

Figure 2.3: PMSM with sinusoidally distributed winding.

The PMSM model in stator reference frame is represented by (2.1) where v_{abc}, i_{abc}, and λ_{abc} are the three phase voltages, currents, and flux linkages in stator frame. r_s is the phase resistance which is assumed to be the same for all phases in case of a healthy PMSM.

$$v_{abc} = r_s i_{abc} + \frac{d\lambda_{abc}}{dt} \tag{2.1}$$

The voltage vector (v_{abc}) will consist of the phase resistive drop ($r_s i_{abc}$) and the change in flux linkage ($\frac{d\lambda_{abc}}{dt}$) due to the time-varying currents passing through phase winding inductance and rotating of the permanent magnets. Assuming the mutual inductance is negligible in concentrated winding machine which is the studied machine in this work, the flux linages are represented by (2.2). Where L_s is the self phase inductance and $\lambda_{PM}(\theta_r)$ represents the

permanent magnet flux linkage (λ_{PM}) as a function of the rotor position (θ_r).

$$\lambda_{abc} = L_s i_{abc} + \lambda_{PM}(\theta_r) = L_s \begin{bmatrix} i_a \\ i_b \\ i_c \end{bmatrix} + \begin{bmatrix} \lambda_{PM}\cos(\theta_r) \\ \lambda_{PM}\cos\left(\theta_r - \frac{2\pi}{3}\right) \\ \lambda_{PM}\cos\left(\theta_r + \frac{2\pi}{3}\right) \end{bmatrix} \tag{2.2}$$

Therefore, the PMSM model in the stator reference frame is represented by (2.3) where the last term represent the induced voltages (e_{abc}) on the machine winding due to the rotating permanent magnets.

$$\begin{bmatrix} v_a \\ v_b \\ v_c \end{bmatrix} = r_s \begin{bmatrix} i_a \\ i_b \\ i_c \end{bmatrix} + L_s \begin{bmatrix} \frac{di_a}{dt} \\ \frac{di_b}{dt} \\ \frac{di_c}{dt} \end{bmatrix} + \lambda_{PM} \begin{bmatrix} \sin(\theta_r) \\ \sin\left(\theta_r - \frac{2\pi}{3}\right) \\ \sin\left(\theta_r + \frac{2\pi}{3}\right) \end{bmatrix} \tag{2.3}$$

Fig. 2.4 shows the equivalent electrical circuit of PMSMs in the stator reference frame.

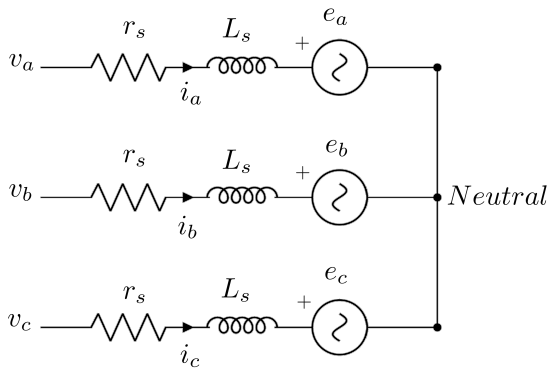

Figure 2.4: Equivalent electrical circuit of PMSM in stator reference frame.

Finding machine parameters as well as the machine control could be complicated if the machine is modeled in the stator reference frame using three-phase quantities. The calculations required for parameter estimation and control could be simplified by representing the ma-

chine model using two orthogonal quantities. In this section, a brief description is given of PMSM modeling in the different reference frames of two orthogonal coordinate system.

2.1.1 Stationary Frame

Transformation of the machine variables (voltages, currents, and flux linkages) from the stator (ABC) reference frame into the stationary ($\alpha\beta$) reference frame is accomplished by using a constant transformation matrix called Clark transform, given in (2.4).

$$x_{\alpha\beta} = \begin{bmatrix} \frac{2}{3} & -\frac{1}{3} & -\frac{1}{3} \\ 0 & \frac{1}{\sqrt{3}} & -\frac{1}{\sqrt{3}} \end{bmatrix} x_{abc} \tag{2.4}$$

The PMSM model can be represented in the orthogonal ($\alpha\beta$) frame by transforming (2.3) using Clark transformation, shown in (2.5).

$$\begin{bmatrix} v_\alpha \\ v_\beta \end{bmatrix} = r_s \begin{bmatrix} i_\alpha \\ i_\beta \end{bmatrix} + \frac{d}{dt} \begin{bmatrix} \lambda_\alpha \\ \lambda_\beta \end{bmatrix} = r_s \begin{bmatrix} i_\alpha \\ i_\beta \end{bmatrix} + L_s \begin{bmatrix} \frac{di_\alpha}{dt} \\ \frac{di_\beta}{dt} \end{bmatrix} + \lambda_{PM} \begin{bmatrix} \cos(\theta_r) \\ \sin(\theta_r) \end{bmatrix} \tag{2.5}$$

Where $v_{\alpha\beta}$, $i_{\alpha\beta}$, and $\lambda_{\alpha\beta}$ represent the voltages, currents, and flux linkages in the stationary frame. This transformation reduces machine variables into two variables with same sinusoidal nature, as the α-axis is aligned with the phase A axis. In control theory, it is preferred to regulate dc reference signals in lieu of sinusoidal ones, and therefore, further simplification is needed to ease the control task.

2.1.2 Rotor Flux Linkage Frame

Transformation of the machine variables from the stationary ($\alpha\beta$) reference frame into the rotor flux linkage (dq) reference frame is accomplished by using a transformation matrix

called Park transform given in (2.6).

$$x_{dq} = \begin{bmatrix} \cos(\theta_r) & \sin(\theta_r) \\ -\sin(\theta_r) & \cos(\theta_r) \end{bmatrix} x_{\alpha\beta} \tag{2.6}$$

If the rotor position (θ_r) is known using position sensor or estimated, then the PMSM model can be represented in the orthogonal (dq) frame by transforming (2.5) using Park transformation as shown in (2.7).

$$\begin{bmatrix} v_d \\ v_q \end{bmatrix} = r_s \begin{bmatrix} i_d \\ i_q \end{bmatrix} + \begin{bmatrix} L_d & 0 \\ 0 & L_q \end{bmatrix} \begin{bmatrix} \frac{di_d}{dt} \\ \frac{di_q}{dt} \end{bmatrix} + \omega_r \begin{bmatrix} -\lambda_q \\ \lambda_d \end{bmatrix} \tag{2.7}$$

Where v_{dq}, i_{dq}, and L_{dq} represent the voltages, currents, and inductances in the rotor flux linkage frame. ω_r is the electrical rotating speed of the rotor flux linkage. Flux linkages (λ_{dq}) in this frame are described in (2.8).

$$\begin{bmatrix} \lambda_d \\ \lambda_q \end{bmatrix} = \begin{bmatrix} L_d & 0 \\ 0 & L_q \end{bmatrix} \begin{bmatrix} i_d \\ i_q \end{bmatrix} + \begin{bmatrix} \lambda_{PM} \\ 0 \end{bmatrix} \tag{2.8}$$

Fig. 2.5 shows the equivalent dq electrical circuit of PMSM in rotor flux linkage frame.

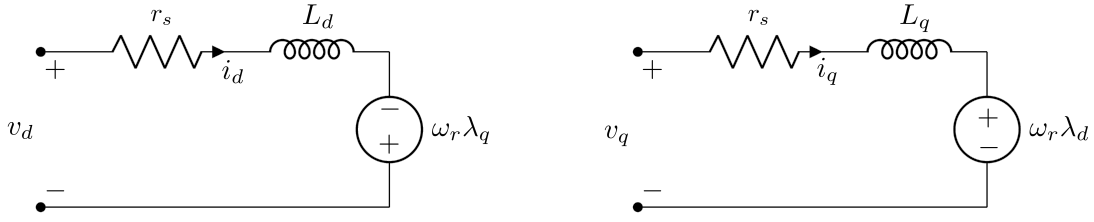

(a) PMSM equivalent circuit in d-axis. (b) PMSM equivalent circuit in q-axis.

Figure 2.5: Equivalent electrical circuit of PMSM in rotor flux linkage reference frame.

This transformed model is simplified by neglecting the iron core loss and the cross-saturation coupling, but it is useful for basic machine representation. This transformation would help in reducing machine variables into two variables with dc nature as the (dq) coordinate system is fixed to the rotor. The physical meaning of the d-axis is the direct flux path across the permanent magnet while the q-axis is the quadrature magnetizing path. The permanence path difference between the machine parts (stator and rotor) is a result of the asymmetrical magnetic properties of PMSM. Usually, it is referred to as machine saliency and it can be observed in the PMSM inductances in the dq frame (L_d and L_q). The PMSM saliency can be improved through varying the rotor geometry by adding flux barriers or using cavities for the embedded magnets. For SPMSM, the machine inductances are identical since the flux reluctance is the same along both direct and quadrature axes. However, L_q in IPMSM is larger than L_d since the flux path in the quadrature axis is less reluctant than the direct axis due to the use of magnet cavities in the latter axis. Fig. 2.6 shows the rotor configuration of SPMSM and IPMSM with the dq axes.

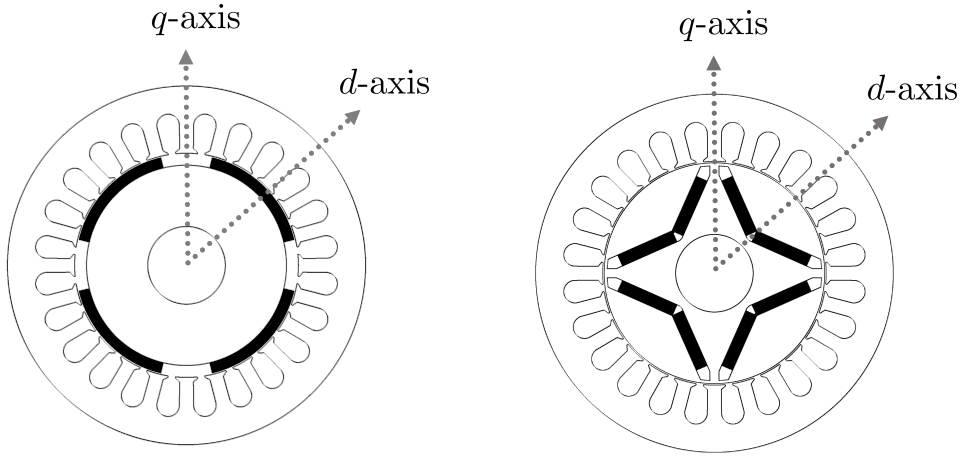

(a) SPMSM ($L_d = L_q$). (b) IPMSM ($L_d < L_q$).

Figure 2.6: Rotor configuration of PMSM typologies with the dq frame.

2.1.3 Stator Flux Linkage Frame

Transformation of the machine variables from the stationary ($\alpha\beta$) reference frame into the stator flux linkage (MT) reference frame is accomplished by using a transformation matrix similar to Park transform but with using the stator flux linkage angle as shown in (2.9).

$$x_{MT} = \begin{bmatrix} \cos(\theta_s) & \sin(\theta_s) \\ -\sin(\theta_s) & \cos(\theta_s) \end{bmatrix} x_{\alpha\beta} \tag{2.9}$$

The stator flux linkage position (θ_s) is estimated using (2.10) .

$$\theta_s = \tan^{-1}\left(\frac{\lambda_\beta}{\lambda_\alpha}\right) \tag{2.10}$$

The PMSM model can be represented in the orthogonal (MT) frame by transforming (2.5) using (2.9), shown in (2.11).

$$\begin{bmatrix} v_M \\ v_T \end{bmatrix} = r_s \begin{bmatrix} i_M \\ i_T \end{bmatrix} + \begin{bmatrix} \frac{d\lambda_M}{dt} \\ \frac{d\lambda_T}{dt} \end{bmatrix} + \begin{bmatrix} \omega_s \lambda_T \\ \omega_s \lambda_M \end{bmatrix} \tag{2.11}$$

Where v_{MT}, i_{MT}, and λ_{MT} represent the voltages, currents, and flux linkages in stator flux linkage frame. The machine variables in MT frame have dc nature where ω_s is the electrical rotating speed of the stator flux linkage. Since the M-axis is aligned with the stator flux linkage vector (λ_s) as shown in Fig. 2.2, the magnetizing flux linkage (λ_M) equal λ_s and the

flux linkage (λ_T) in T-axis is null. The simplified PMSM model is given in (2.12)

$$\begin{bmatrix} v_M \\ \\ v_T \end{bmatrix} = r_s \begin{bmatrix} i_M \\ \\ i_T \end{bmatrix} + \begin{bmatrix} \frac{d\lambda_s}{dt} \\ \\ 0 \end{bmatrix} + \begin{bmatrix} 0 \\ \\ \omega_s \lambda_s \end{bmatrix} \tag{2.12}$$

Another transformation can be done from dq frame into MT frame by using the transformation matrix given in (2.13).

$$x_{MT} = \begin{bmatrix} \cos(\delta) & \sin(\delta) \\ \\ -\sin(\delta) & \cos(\delta) \end{bmatrix} x_{dq} \tag{2.13}$$

The torque angle required for the transformation (δ) is estimated by (2.14).

$$\delta = tan^{-1}\left(\frac{\lambda_q}{\lambda_d}\right) \tag{2.14}$$

This transformation is useful in obtaining the relationship between the MT and dq flux linkages using (2.13) to transform (2.8) as shown in(2.15).

$$\begin{bmatrix} \lambda_M \\ \\ \lambda_T \end{bmatrix} = \begin{bmatrix} L_{MM} & L_{MT} \\ \\ L_{TM} & L_{TT} \end{bmatrix} \begin{bmatrix} i_M \\ \\ i_T \end{bmatrix} + \lambda_{PM} \begin{bmatrix} \cos(\delta) \\ \\ -\sin(\delta) \end{bmatrix} \tag{2.15}$$

Where the inductance matrix is calculated using (2.16).

$$\begin{bmatrix} L_{MM} \\ L_{MT} \\ L_{TM} \\ L_{TT} \end{bmatrix} = \begin{bmatrix} L_d \cos^2(\delta) + L_q \sin^2(\delta) \\ -L_d \sin(\delta)\cos(\delta) + L_q \sin(\delta)\cos(\delta) \\ -L_d \sin(\delta)\cos(\delta) + L_q \sin(\delta)\cos(\delta) \\ L_d \sin^2(\delta) + L_q \cos^2(\delta) \end{bmatrix} \tag{2.16}$$

For SPMSM, the diagonal inductances (L_{MT} and L_{TM}) are zero since ($L_d = L_q = L_s$). Therefore, the resulting flux linkages are described in (2.17).

$$\begin{bmatrix} \lambda_M \\ \lambda_T \end{bmatrix} = \begin{bmatrix} L_s & 0 \\ 0 & L_s \end{bmatrix} \begin{bmatrix} i_M \\ i_T \end{bmatrix} + \lambda_{PM} \begin{bmatrix} \cos(\delta) \\ -\sin(\delta) \end{bmatrix} \tag{2.17}$$

Since $\lambda_T = 0$, then the torque component current (i_T) would be calculated using (2.18).

$$i_T = \frac{1}{L_s} \lambda_{PM} sin(\delta) \tag{2.18}$$

However, this is not the case in IPMSM as ($L_d \neq L_q$). By solving the second row in (2.15) where $\lambda_T = 0$, the magnetizing component current (i_M) is shown in (2.19).

$$i_M = \frac{2\lambda_{PM} sin(\delta) - \left[(L_q + L_d) - (L_q - L_d)\cos(2\delta)\right]}{(L_q - L_d)\sin(2\delta)} i_y \tag{2.19}$$

Using (2.19) in the first row of (2.15) results in (2.20).

$$i_T = \frac{1}{2L_d L_q} \left[2\lambda_{PM} L_q sin(\delta) + \lambda_M (L_d - L_q) sin(2\delta)\right] \tag{2.20}$$

2.2 PMSM Control

PMSM can be grid-connected or driven by an inverter. For the former type, the machine rotor should be designed with dampers to be self-starting like induction machines [29]. In the latter type, PMSM should be driven by Variable Frequency Drives (VFDs) to operate at different speed conditions. Two control strategies could be implemented to regulate the PMSM speed: scalar and vector control. The scalar control is considered the simplest

control algorithm since it is an open-loop regulation without any need for feedback on motor position or identifying its parameters. The PMSM speed is set and the voltage magnitude should be changed accordingly to maintain a constant voltage/frequency ratio. However, scalar-controlled PMSMs suffer from instability when there is a loss of synchronization at load/speed changes. This problem could be overcome by using closed feedback control or designing the PMSM rotor with dampers to maintain the rotor synchronization with the electrical supply frequency. Most of the PMSMs are manufactured without dampers and this would limit the applicability of scalar control to PMSMs.

Vector control achieves high dynamic performance, in comparison with scalar control, by controlling both the magnitude and angle of the stator flux linkage of PMSM. Field Oriented Control (FOC) and Direct Torque Control (DTC) are the most widely applied vector control schemes for alternating machines. FOC was introduced in the late 1960s for alternating current machines and then firstly adopted by the Toshiba industry one decade later. The main concept of FOC is to control the stator current vector in the rotor flux linkage frame [30, 31]. On the other hand, DTC aims to regulate the electromagnetic torque and stator flux linkage directly without any need for complex orientation [32]. It was proposed in the early 1970s and then commercialized by the ABB industry two decades later [33, 34].

It has not been made possible to implement vector control without integrating high-speed processors since the torque producing and flux magnetizing components need to be decoupled. Performance improvements of micro-controller/DSP will lead to better control implementation as more complex control computations and adaptive machine model estimation will be permitted. A brief description is given in this section of FOC and DTC drives to identify the differences between these high-performance controllers.

2.2.1 Field Oriented Control

Magnetizing and torque current components in the direct and quadrature axes (i_d and i_q) are regulated separately using a proportional-integral (PI) controllers in Field Oriented Control (FOC) to control the machine's torque and flux indirectly. Hence, FOC is also called indirect torque control. Fig. 2.7 shows the fundamental block diagram that is used for FOC where an encoder is needed to estimate the rotor position (θ_r) required for current vector decoupling. The widely applied modulation technique to control the inverter switching scheme in FOC is the Space Vector Pulse Width Modulation (SVPWM) due to its high utilization of the DC link and low harmonic distortion [35]. The principle behind SVPWM is to synthesize a reference space voltage vector using timely applied active and zero voltage vectors at a fixed switching frequency.

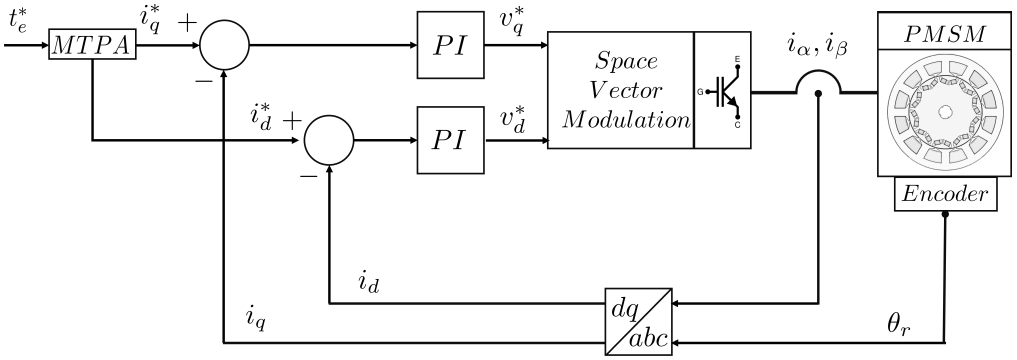

Figure 2.7: Inner current control loop in FOC.

The expressions of d and q currents and the corresponding machine torque as a function of both currents are shown in (2.21) and (2.22), respectively.

$$\begin{aligned} i_q &= |i_s| \cos(\beta) \\ i_d &= -|i_s| \sin(\beta) \end{aligned} \tag{2.21}$$

$$t_e = \frac{3P_n}{4} i_q \left[\lambda_{PM} + (L_d - L_q) i_d\right] \tag{2.22}$$

Where $|i_s|$ and β are the stator current magnitude and angle measured from the q-axis, respectively. t_e is the machine electromagnetic torque. P_n is the number of rotor poles in PMSM. By controlling $|i_s|$ and β, different (i_d,i_q) combinations can be generated and different control modes can be achieved, such as Maximum Torque Per Ampere (MTPA), Field Weakening (FW), Maximum Torque Per Voltage (MTPV), and Unity power factor (UPF) [36]. The control mode selection is based on the PMSM type and operating speed. Below the based speed, the MTPA control is utilized to generate the maximum torque for a given current in order to minimize the copper losses [37, 38]. The excitation angle (β) in MTPA region is described in (2.23)

$$\beta_{Tmax} = \sin^{-1}\left[\frac{\sqrt{8(L_q - L_d)^2 |i_s|^2 + \lambda_{PM}^2} - \lambda_{PM}}{4|i_s|(L_q - L_d)}\right] \tag{2.23}$$

For SPMSM, MTPA control can be achieved by applying the q-axis current component while keeping the d-axis current component equal to zero since there is no magnetic saliency ($L_q - L_d = 0$). However, the optimum current angle ($\beta_{T_{max}}$) should be found for IPMSM theoretically, if machine parameters are known, or experimentally to implement the MTPA control. The d-axis current component plays a significant role in torque generation for IPMSM in order to maximize the reluctance torque utilization. IPMSM control in MTPA region is the used method in this work where the optimum dq currents for a given torque is stored in a lookup table.

2.2.2 Direct Torque Control

The conventional Direct Torque Control (DTC) was first proposed in [28] for PMSMs. Fig. 2.8 shows the fundamental block diagram that is used for DTC implementation where δ_{t_e} and $\delta_{\lambda s}$ are the outputs of hysteresis comparators.

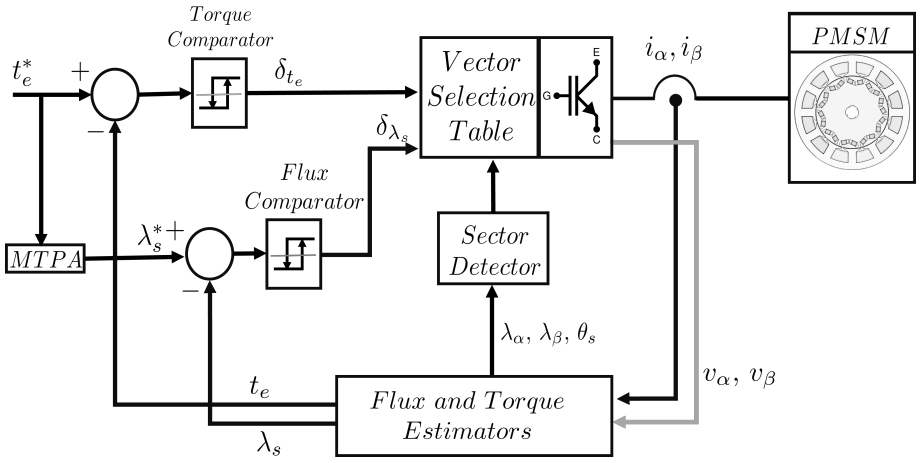

Figure 2.8: Torque control loop in DTC.

Two hysteresis comparators are utilized to regulate the produced torque and stator flux linkage magnitude. Therefore, the torque and flux estimation are required for use in the feedback loop. These quantities are usually estimated in the stationary ($\alpha\beta$) frame, as described in (2.24) and (2.25), to eliminate the need for the encoder.

$$t_e = \frac{3P_n}{4}\left(i_\beta \lambda_\alpha - i_\alpha \lambda_\beta\right) \tag{2.24}$$

$$\begin{aligned} \lambda_\alpha &= \int (v_\alpha - r_s i_\alpha)dt + \lambda_{\alpha_0} \\ \lambda_\beta &= \int (v_\beta - r_s i_\beta)dt + \lambda_{\beta_0} \end{aligned} \tag{2.25}$$

Where λ_{α_0} and λ_{β_0} represent the initial values of flux linkages in stationary frame based on the frame alignment. The voltages in ($\alpha\beta$) frame are estimated using the switching pulses

(s_a, s_b, s_c) of inverter legs and the DC link voltage (v_{dc}) as shown in (2.26).

$$\begin{aligned} v_\alpha &= \frac{v_{dc}}{3}[2s_a - s_b - s_c] \\ v_\beta &= \frac{v_{dc}}{\sqrt{3}}[s_b - s_c] \end{aligned} \tag{2.26}$$

At steady state, λ_s rotates at the same synchronous speed as λ_{PM} and the phase difference between them is the torque angle as shown in Fig. 2.2. DTC increases or decreases the speed of λ_s as more or less torque is required. By neglecting the resistive drop $r_s i_{\alpha\beta}$ in (2.25), the flux linkages are mainly influenced by the selected voltage vector. The null voltage vectors are removed from the selection table as they do not maintain the torque level, as they do in induction motors, instead they reduce the torque because λ_{PM} still rotates. The appropriate voltage vector is chosen as shown in Table 2.1, following the outputs of hysteresis controllers and the location of the stator flux linkage vector that could be found using (2.10). The switching states for the inverter switches are determined for each control cycle by the selected voltage vector and therefore the switching frequency is variable in DTC.

Table 2.1: Voltage Vector Selection in DTC driven PMSM.

		$\boldsymbol{\theta_s}$					
$\boldsymbol{\delta_{\lambda_s}}$	$\boldsymbol{\delta_{t_e}}$	$\left[-\frac{\pi}{6}, \frac{\pi}{6}\right)$	$\left[\frac{\pi}{6}, \frac{\pi}{2}\right)$	$\left[\frac{\pi}{2}, \frac{5\pi}{6}\right)$	$\left[\frac{5\pi}{6}, -\frac{5\pi}{6}\right)$	$\left[-\frac{5\pi}{6}, -\frac{\pi}{2}\right)$	$\left[-\frac{\pi}{2}, -\frac{\pi}{6}\right)$
Increase	Increase	V_2	V_3	V_4	V_5	V_6	V_1
	Decrease	V_6	V_1	V_2	V_3	V_4	V_5
Decrease	Increase	V_3	V_4	V_5	V_6	V_1	V_2
	Decrease	V_5	V_6	V_1	V_2	V_3	V_4

DTC driven PMSMs can operate in MTPA region by finding the optimum flux linkage that would result in the lowest current for a given torque. It could be found theoretically [39] or experimentally [40]. Then, the obtained stator flux linkages can be stored in a lookup table

for online implementation. Since the stator flux linkage angle (θ_s) is available in DTC, the DTC driven PMSM can be modeled in stator flux linkage (MT) frame as described earlier in this chapter. The electromagnetic torque for PMSM in MT frame is calculated by (2.27).

$$t_e = \frac{3P_n}{4}(\overrightarrow{i_s} \times \overrightarrow{\lambda_s}) \tag{2.27}$$

However, the T-axis flux linkage equals zero since the M-axis is oriented with the stator flux linkage as shown in Fig. 2.2. Therefore, the torque is governed only by T-axis current (i_t) and stator flux linkage (λ_s) as described in (2.28).

$$t_e = \frac{3P_n}{4} i_T \lambda_M = \frac{3P_n}{4} i_T \lambda_s \tag{2.28}$$

Substituting (2.18) in (2.28), the torque of SPMSM in MT frame is given by (2.29).

$$t_e = \frac{3P_n}{4L_s} \lambda_s \lambda_{PM} \sin(\delta) \tag{2.29}$$

By substituting (2.20) in (2.28), the torque of IPMSM in MT frame is given by (2.30).

$$t_e = \frac{3P_n}{8L_d L_q} \lambda_s \left[2\lambda_{PM} L_q \sin(\delta) + \lambda_M (L_d - L_q) \sin(2\delta) \right] \tag{2.30}$$

Where the first term of (2.30) represents the magnetic torque and the second part represents the reluctance torque due to saliency in IPMSM.

2.2.3 Performance Comparison

The control performance of FOC and DTC has been investigated within a MATLAB environment for two PMSM machines with low and high saliency. The parameters of both PMSMs are listed in Table 2.2.

Table 2.2: Parameters of driven machines.

Machine Parameter	**Symbol**	**PMSM [A]**	**PMSM [B]**	**Unit**
Number of phases	m	3	3	-
Number of pole pairs	P_n	4	5	-
Phase resistance	r_s	0.8	1.5	Ω
Magnet flux linkage	λ_{PM}	35	287	mWb
d-axis inductance	L_d	5	31.3	mH
q-axis inductance	L_q	10	62.4	mH
Maximum stator current	I_s	10	25	A
Rated torque	T_e	2	65	N.m
Rated speed	n_m	1000	800	rpm
Inverter				
Dc link voltage	V_{dc}	60	680	V

Both machines are controlled in torque regulation mode within the MTPA region while their shafts are connected to a constant speed load. The timing profile of torque and speed changes for both machines is shown in Table 2.3 where (T_1, T_2, T_3, T_4) time instants are at (0, 0.1, 0.25, 0.4) seconds, respectively, out of total (0.5) seconds as a simulation time.

Table 2.3: Timing profile of torque and speed changes for driven machines.

	PMSM [A]		**PMSM [B]**	
Time	n_m [rpm]	T_e [N.m]	n_m [rpm]	T_e [N.m]
T_1	350	1	350	10
T_2	500	1	500	10
T_3	500	1.5	500	30
T_4	600	0.5	600	15

The same reference torque and speed are used in FOC and DTC for the machine under test. Based on the reference torque, the commanded dq currents are generated in FOC

through a lookup table while the commanded stator flux linkage is generated in DTC. In order to make a fair comparison, the switching frequency of both control schemes was kept the same. The bandwidth for both FOC and DTC was separately adjusted to optimize their steady-state and dynamic performance [41]. The stator flux linkage locus in $\alpha\beta$ frame is compared of both drives. The frequency spectrum of phase A stator current is compared in both drives showing the switching frequency effect on the spectrum.

For PMSM [A] driven by FOC, the bandwidth of the PI controller is chosen to be 42 rad/s. Therefore, the controller integral gains ($k_{I_{dq}}$) are 33.5 and the controller proportional gains ($k_{p_{dq}}$) are (0.2, 0.4), respectively. The switching and sampling frequency are 10 kHz and 20 kHz, respectively. Fig. 2.9 shows the performance of FOC driven PMSM [A] in terms of speed, torque, flux linkage, and stator currents.

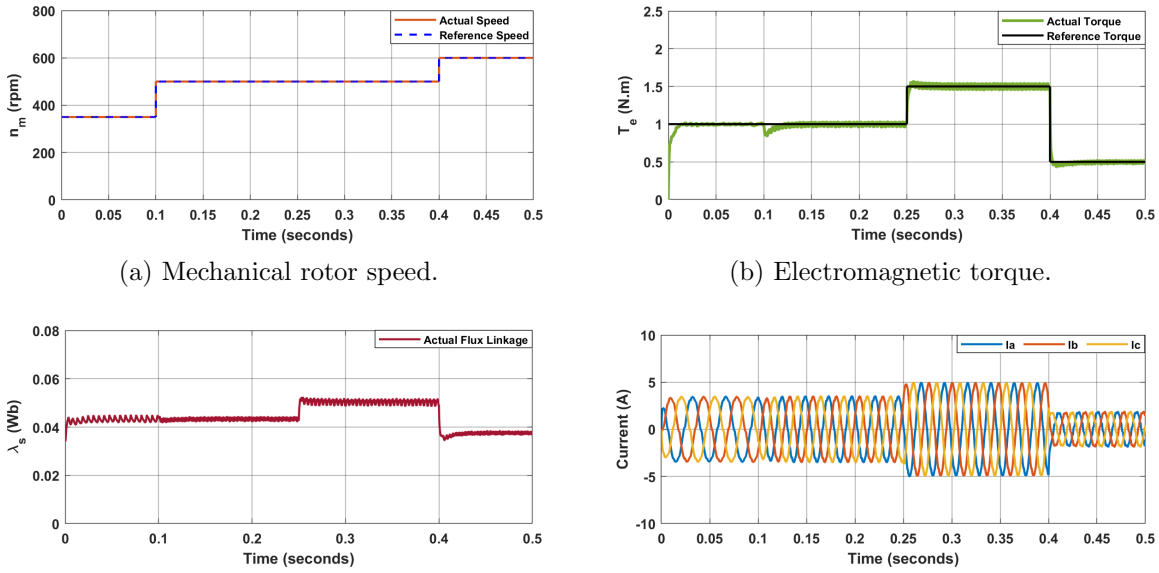

(a) Mechanical rotor speed.

(b) Electromagnetic torque.

(c) Stator flux linkage.

(d) Stator ABC currents.

Figure 2.9: Performance of PMSM [A] under FOC drives.

As can be noticed, the FOC controller is capable of achieving the desired torque of PMSM [A] at different speeds with good steady state performance. A smooth torque waveform and low distortion in the stator current can be achieved by FOC at steady state. The current

regulation performance in rotor flux linkage frame can be seen in Fig. 2.10.

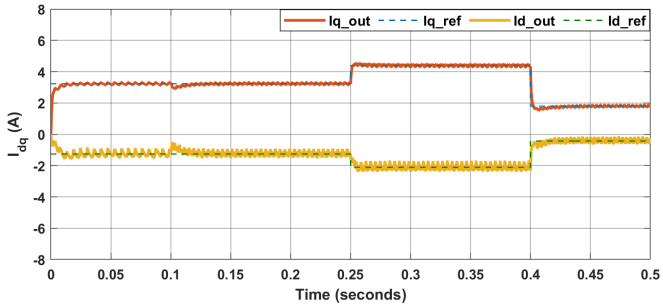

Figure 2.10: Rotor field oriented currents regulation of PMSM [A].

When PMSM [A] is driven by DTC, the sampling frequency is kept the same as in FOC even though DTC would exhibit better performance when high sampling frequency is used. The torque and flux hysteresis bands are 0.1 $N.m$ and 0.025 Wb, respectively. They are kept constant during the simulation regardless of the reference torque. Fig. 2.11 shows the control performance in terms of speed, torque, flux linkage, and stator currents.

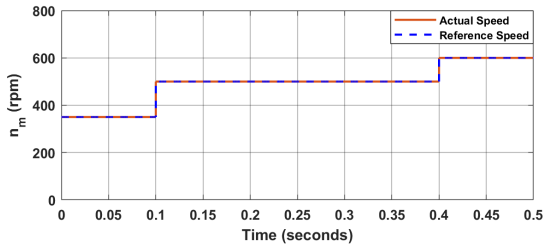

(a) Mechanical rotor speed.

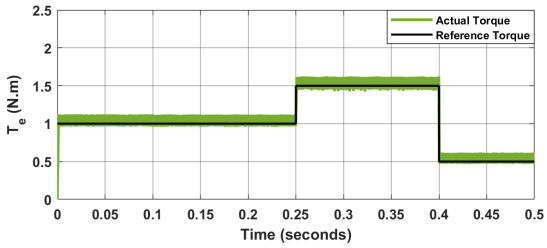

(b) Electromagnetic torque.

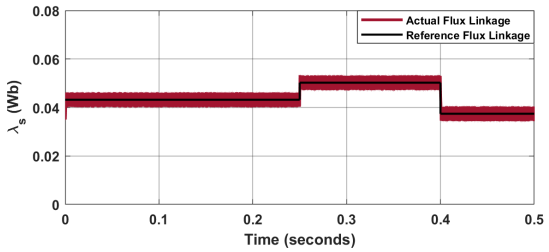

(c) Stator flux linkage.

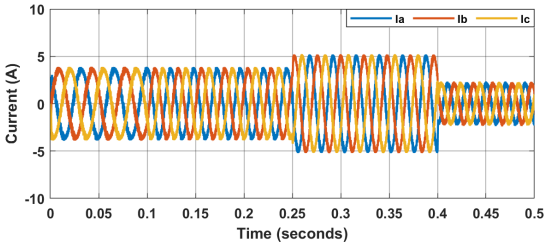

(d) Stator ABC currents.

Figure 2.11: Performance of PMSM [A] under DTC drives.

As can be noticed, the DTC controller is capable of achieving the desired torque of PMSM [A] at different speeds with good transient and steady state performance. The torque response

of FOC and DTC is compared in Fig. 2.12. It can be observed that both drives provide adequate control performance with better steady-state behavior in the case of FOC and quick torque dynamics in DTC. Therefore, one control scheme can be more suitable than the other based on the industrial application requirements.

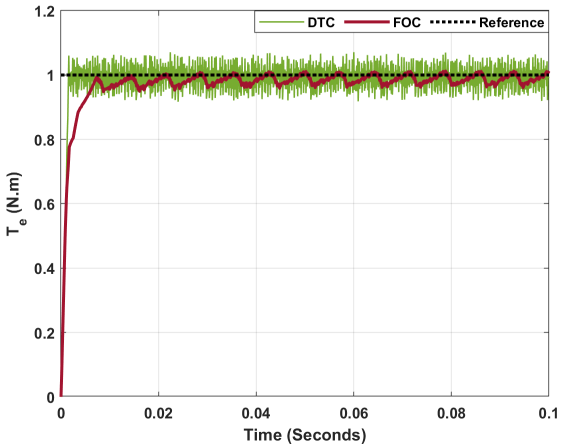

Figure 2.12: Torque response of PMSM [A] controlled by FOC and DTC.

The effect of using hysteresis bands in DTC driven PMSM, in comparison with FOC, can be better observed in the stator flux linkage locus in $\alpha\beta$ frame as shown in Fig. 2.13.

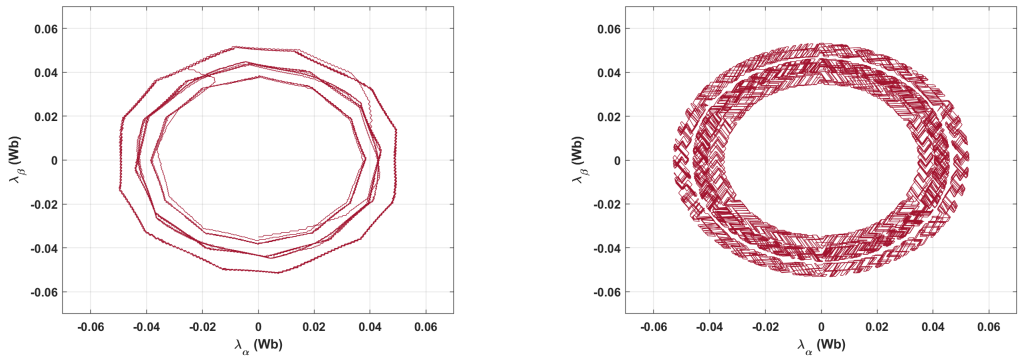

(a) FOC. (b) DTC.

Figure 2.13: Stator $\alpha\beta$ flux linkage locus of PMSM [A] controlled by FOC and DTC.

Variable switching frequency is expected in DTC drives based on the operating conditions while it is fixed in FOC drives. The frequency spectrum of stator phase A current in PMSM

[A] controlled by FOC and DTC is shown in Fig. 2.14 at the first time interval (T_1 to T_2).

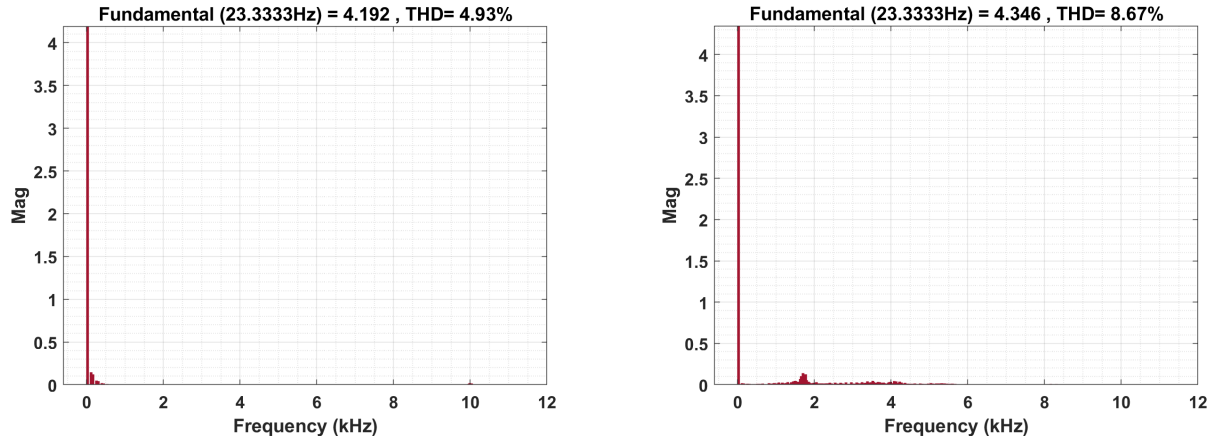

(a) FOC. (b) DTC.

Figure 2.14: Frequency spectrum of stator phase A current of PMSM [A] controlled by FOC and DTC during (T_1 to T_2).

The frequency spectrum of stator phase A current in FOC and DTC is shown in Fig. 2.15 at the second time interval (T_2 to T_3).

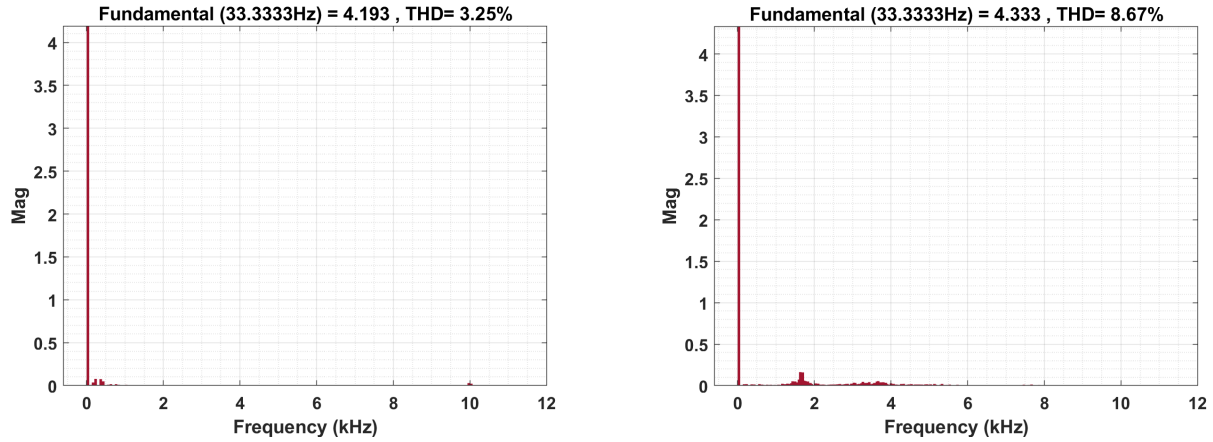

(a) FOC. (b) DTC.

Figure 2.15: Frequency spectrum of stator phase A current of PMSM [A] controlled by FOC and DTC during (T_2 to T_3).

It could be observed from the current spectrum that the switching frequency in FOC is set at 10 kHz and has negligible effect on the low frequency components around the fundamental component. However, the total harmonic distortion (THD) is increased in case of DTC and

the switching frequency has significant effect on the low frequency components around the fundamental component. This is due to the fact that the switching frequency in DTC has lower harmonic order close to the low frequency band around the fundamental and has higher magnitude in comparison with FOC case.

For PMSM [B] driven by FOC, the bandwidth of the PI controller is chosen to be 8 rad/s. Therefore, the controller integral gains ($k_{I_{dq}}$) are 11.78 and the controller proportional gains ($k_{p_{dq}}$) are (0.25, 0.5), respectively. The switching and sampling frequency are 10 kHz and 20 kHz, respectively. Fig. 2.16 shows the performance of FOC driven PMSM [B] in terms of speed, torque, flux linkage, and stator currents.

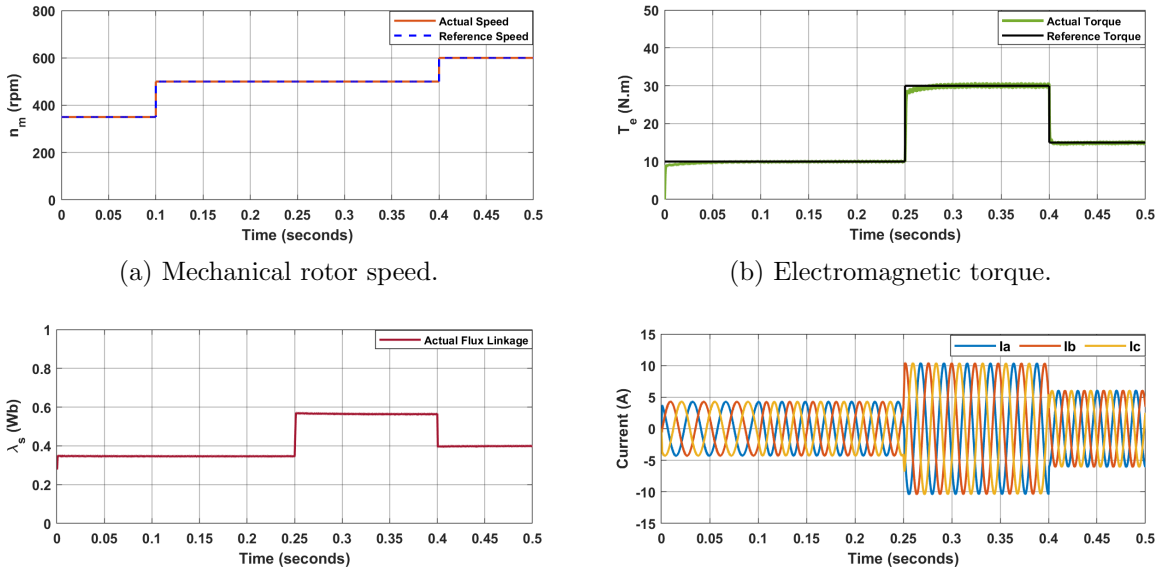

(a) Mechanical rotor speed.

(b) Electromagnetic torque.

(c) Stator flux linkage.

(d) Stator ABC currents.

Figure 2.16: Performance of PMSM [B] under FOC drives.

As can be noticed, the FOC controller is capable in achieving the desired torque of PMSM [B] at different speeds with good steady state performance. The current regulation performance in rotor flux linkage frame can be seen in Fig. 2.17.

When PMSM [B] is driven by DTC, the sampling frequency is kept the same as in FOC even though DTC would exhibit better performance when high sampling frequency is used.

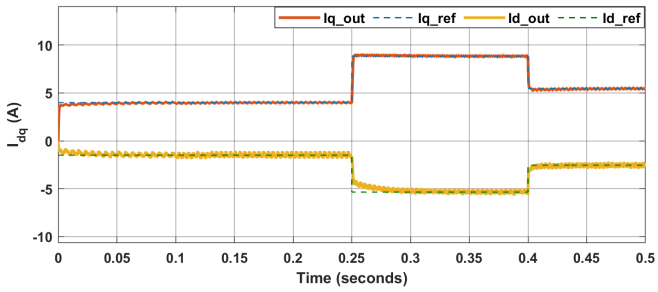

Figure 2.17: Rotor field oriented currents regulation of PMSM [B].

The torque and flux hysteresis bands are 2 $N.m$ and 0.1 Wb, respectively. They are kept constant along the simulation time regardless of the reference torque. Fig. 2.18 shows the performance of DTC driven PMSM [B] in terms of speed, torque, flux linkage, and stator currents.

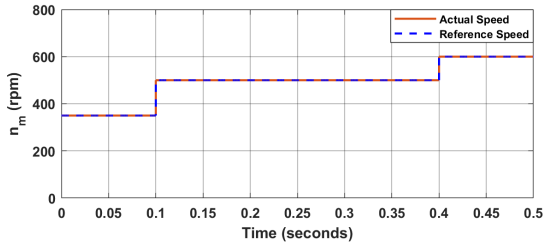

(a) Mechanical rotor speed.

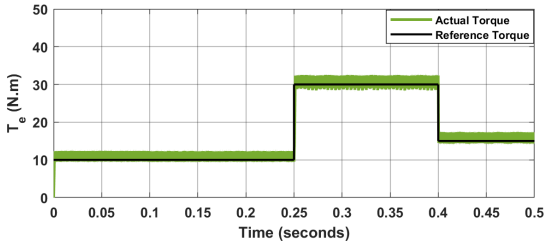

(b) Electromagnetic torque.

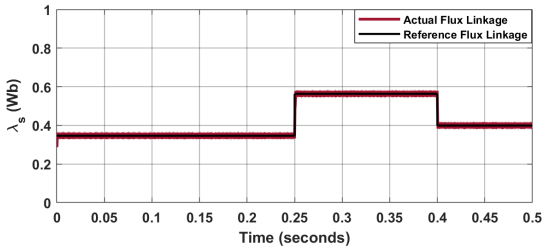

(c) Stator flux linkage.

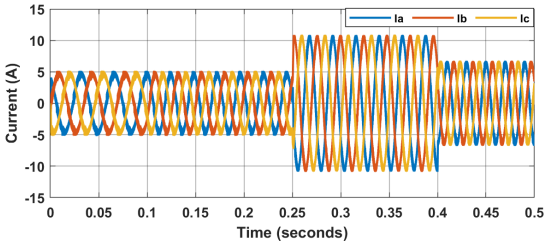

(d) Stator ABC currents.

Figure 2.18: Performance of PMSM [B] under DTC drives.

As can be noticed, the DTC controller is capable in achieving the desired torque of PMSM [B] at different speeds with good transient and steady state performance. The FOC and DTC torque response is compared in Fig. 2.19.

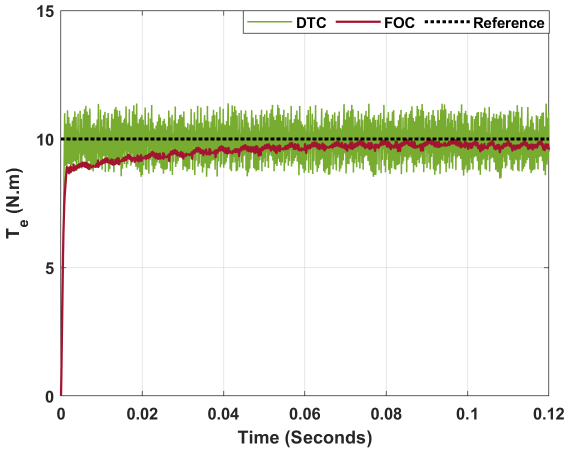

Figure 2.19: Torque response of PMSM [B] controlled by FOC and DTC.

The effect of using hysteresis bands in DTC driven PMSM, in comparison with FOC, can be better observed in the stator flux linkage locus in $\alpha\beta$ frame as shown in Fig. 2.20.

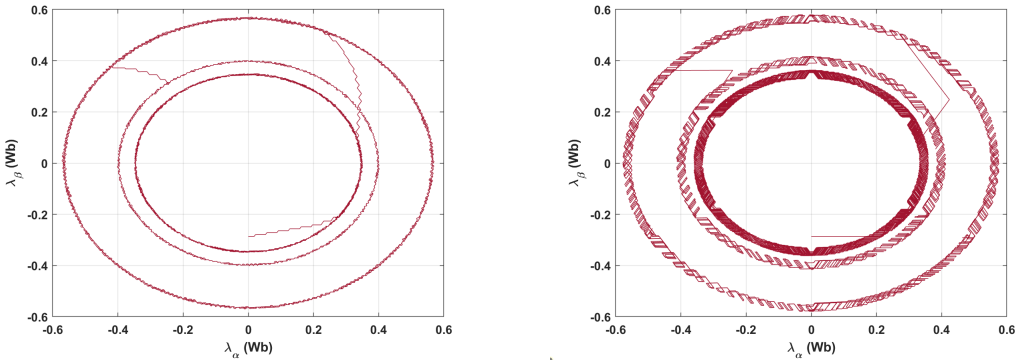

(a) FOC. (b) DTC.

Figure 2.20: Stator $\alpha\beta$ flux linkage locus of PMSM [B] controlled by FOC and DTC.

As expected, the switching frequency in DTC drives varies while it is fixed in FOC drives. The frequency spectrum of stator phase A current in PMSM [B] controlled by FOC and DTC is shown in Fig. 2.21 at the first time interval (T_1 to T_2).

The frequency spectrum of stator phase A current in FOC and DTC is shown in Fig. 2.22 at the second time interval (T_2 to T_3).

In comparison with DTC, it is noticed from the current spectrum that the switching fre-

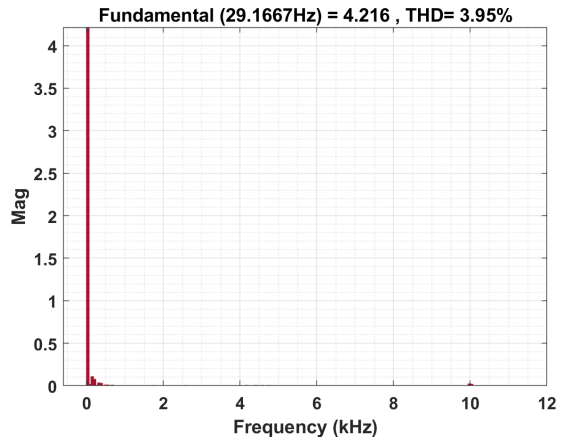

(a) FOC.

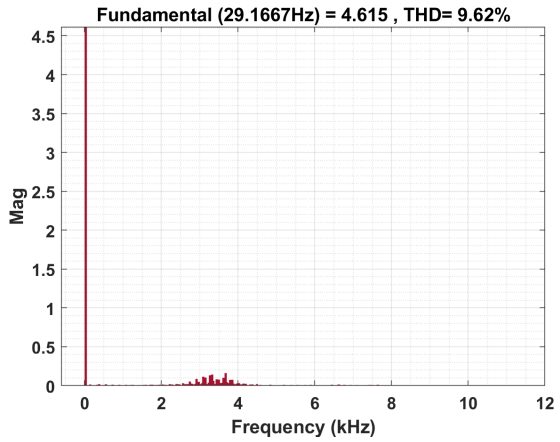

(b) DTC.

Figure 2.21: Frequency spectrum of stator phase A current of PMSM [B] controlled by FOC and DTC during (T_1 to T_2).

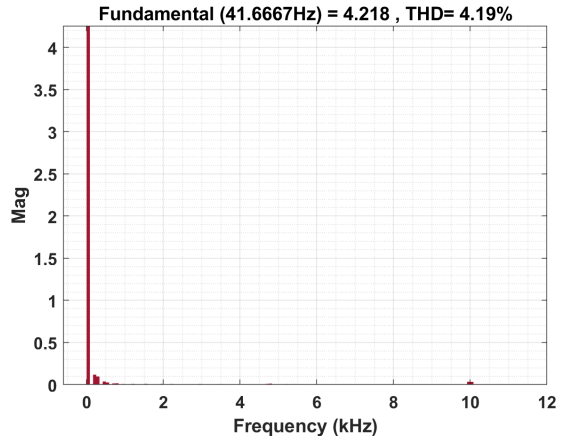

(a) FOC.

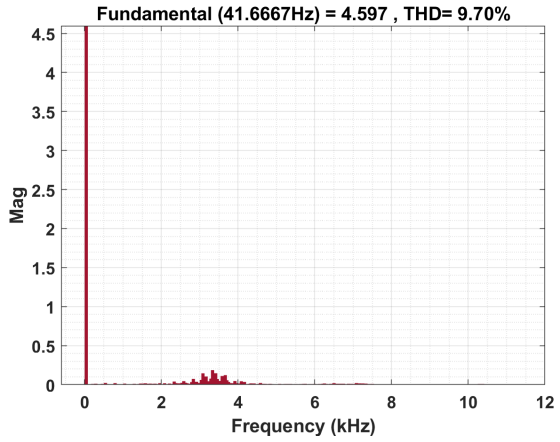

(b) DTC.

Figure 2.22: Frequency spectrum of stator phase A current of PMSM [B] controlled by FOC and DTC during (T_2 to T_3).

quency in FOC has negligible effect on the low frequency components around the fundamental one due to its lower magnitude and higher harmonic order away from the low frequency band.

2.3 PMSM Fault Types

As electrification advances, the safety and reliability of electrified products is a primary concern of manufacturers, as well as users. PMSMs suffer from different types of failures due to various conditions that affect their reliable operation. These failures can be divided into stator and rotor faults based on the affected machine part. Stator faults are the most commonplace in electric machines and they result in an unbalanced electrical system that could cause catastrophic damage to the machine itself and the entire drive system if they are not addressed at their premature stages. On the other hand, rotor faults are typical in large machines and they result in an unbalanced magnetic system that could lead eventually to machine damage if left unaddressed. Analyzing the behavior of a drive system under these faults is crucial in order to design fault diagnosis and mitigation schemes to improve the reliability and robustness of the drive system.

2.3.1 Stator Faults

Stator faults are common and generally caused by one or a combination of thermal, electrical, mechanical, and environmental stress on the machine windings [42]. The factors that lead to stator faults are unavoidable but preventive maintenance can be achieved when the failure causes are known. Two main stator faults could occur: TTSC and HRC.

2.3.1.1 Turn-to-Turn Short Circuit

The most common fault in PMSMs is an abnormal short connection between phase turns or turns from different phases. It is a result of insulation degradation due to aging or overloading [43]. It propagates faster than the other faults, and results in further insulation degradation and motor outage in the end [44]. The fault severity depends mainly on the

short path resistance (R_f) and the number of shorted turns (N_f). As N_f increases and R_f decreases, the short circuit current rises as shown in Fig. 2.23 and causes excess heat in the machine. Therefore, if this anomaly is not identified at its inception, it will develop into more severe levels that may cause damage to the stator winding.

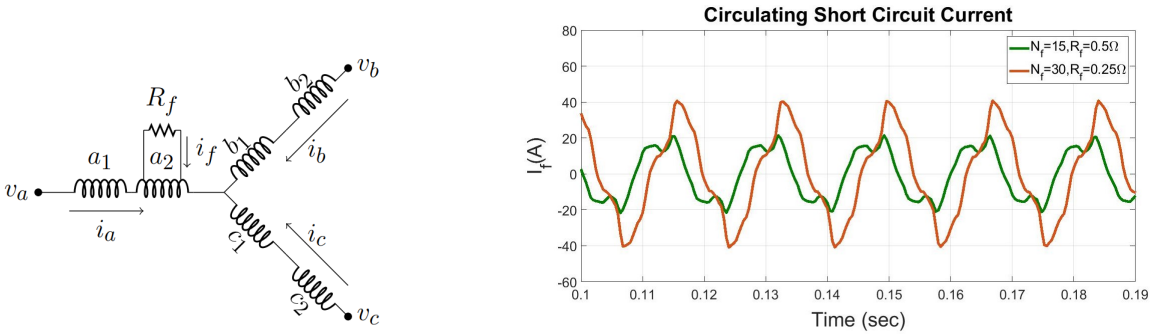

(a) Series winding with shorted turns electric machine [45].

(b) Short circuit current at different shorted turns and fault resistances.

Figure 2.23: Turn-to-turn short circuit: (a) series winding with shorted turns and (b) short circuit current at different shorted turns and fault resistances.

2.3.1.2 High Resistance Contact

This progressive electrical fault occurs at the stator terminals originating from weak joints at the inverter-motor connection. It is mainly caused by vibration or damaged contact connections due to corrosion. If the fault is not detected accurately at its inception, it leads to an open-phase fault at high severity levels. It will result in unbalanced stator currents that increase the torque ripple and machine losses [22, 46]. The current imbalance can be seen in Fig. 2.24. This fault should be detected and separated from ITSC in particular to ensure that the proper mitigation would be applied.

2.3.2 Rotor Faults

Rotor faults in PMSMs can result in unbalanced magnetic pull toward the machine stator and increase the machine vibration [47, 48]. This would reduce the lifetime of machine parts.

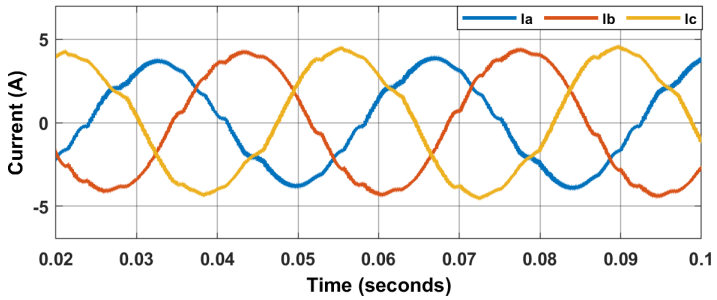

Figure 2.24: Unbalanced stator currents of PMSM under HRC fault.

Two main rotor faults can occur: static eccentricity and partial demagnetization. These faults can lead to occurrence of additional faults and potentially an undesired shutdown if not diagnosed and mitigated early. Therefore, rotor fault detection is crucial to avoid any damage to the machine structure and improve the drive performance.

2.3.2.1 Static Eccentricity

Eccentricity is an example of mechanical rotor failures that may inherently exist due to manufacturing tolerances. It increases the noise, vibration, and harshness (NVH) and can lead to rotor rubbing with stator lamination [20]. It could be a result of a misaligned rotor or manufacturing tolerance. It is termed static fault when the rotating axis of the rotor is shifted from the geometric center of the stator by a fixed value in one direction. Therefore, the air gap surrounding the rotor becomes unevenly distributed, so does the magnetic flux distribution. An unbalanced radial magnetic pull is established subsequently toward the stator core, and it grows as the fault becomes more severe [2]. This will cause rubbing between rotor and stator surfaces and that could lead to damages in core, wedges, and winding insulation. The fault severity is expressed in (2.31).

$$ECC = \frac{\epsilon}{g} \times 100\% \tag{2.31}$$

where (g) is the air gap length and (ϵ) is the shift length. Fig. 2.25 shows a comparison between healthy and eccentric rotors. The air gap length change due to static eccentricity

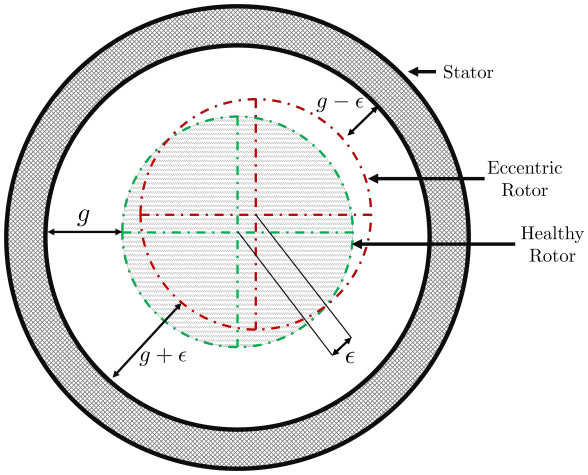

Figure 2.25: Comparison between healthy and eccentric machines.

fault causes a change in the reluctance. The machine reluctance is expressed in (2.32).

$$\mathcal{R} = \frac{g}{\mu_o A_g} \tag{2.32}$$

Higher flux concentration is expected at the area with a lower air gap ($g - \epsilon$) since it has lower reluctance, whereas the area with higher air gap length ($g + \epsilon$) has higher reluctance and, therefore, lower flux concentration. Due to the machine non-linearity, the magnetic flux increase at the smallest airgap area will be higher than the magnetic flux decrease in the largest airgap area. As a result, the total magnetic flux increase causes the phase inductance to increase and yields early saturation in the machine. The magnetic phase inductance (L) is expressed in (2.33).

$$L = \frac{N^2 \times \phi}{F} \tag{2.33}$$

Where (N) is the turns number, (ϕ) is the magnetic flux, and (F) is the magneto-motive force. Fig. 2.26 shows the eccentricity effect on phase B inductance where the phase windings

are located in the direction of eccentricity.

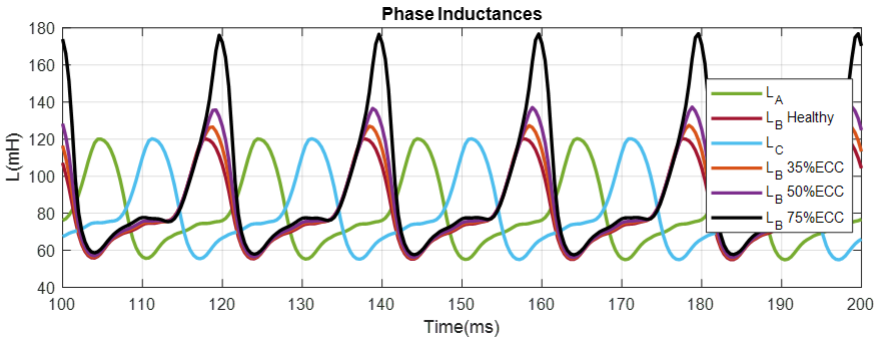

Figure 2.26: Eccentricity effect on magnetic inductance.

2.3.2.2 Partial Demagnetization

Permanent magnets are the most critical parts in PMSMs for electromagnetic torque generation. However, their performance degrades due to aging, high temperature, or intense opposing magnetic field from the stator current, particularly in the field weakening control region. Therefore, demagnetization could take place within driven PMSMs if the electromagnetic constraints are exceeded by improper operation in the field weakening region or due to the occurrence of a severe TTSC fault. As a result, the rotor magnets get demagnetized causing asymmetric flux distribution in the air gap. It is termed partial demagnetization when these demagnetizing conditions occur locally in specific magnets or poles. The partially demagnetized magnets will have lower residual flux densities than those in the healthy state as shown in Fig. 2.27. Reduction in the average torque and increase in the torque ripple are the main consequences of the demagnetization fault. The resultant fluctuation in the produced torque can possibly lead to eccentricity or short circuit faults at high severity levels [49]. Moreover, it degrades the performance of the drive system significantly and could cause loss of controllability in severe faulty cases [50].

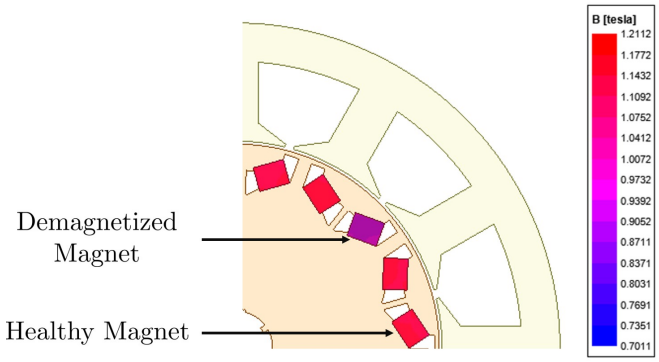

Figure 2.27: Residual flux density comparison between healthy and demagnetized magnets.

Chapter 3

Assessment of Fault Effects and DTC Response

Measured currents, estimated voltages, estimated flux linkages, and estimated torque are the required signals for the DTC drive to operate. Machine currents or voltages will include additional harmonics as a result of the response of the comparators in DTC drive to the fault occurrence. Therefore, thorough analysis of the reaction of the flux and torque hysteresis comparators in DTC upon a fault occurrence is essential. However, it is known that the nonlinear nature of the hysteresis comparators in DTC poses challenges to address this problem analytically [51–53]. Here, the behavior of the current under faulty conditions is described analytically to investigate the DTC reaction.

The initial consequence of the fault occurrence is generation of a negative sequence component in addition to the positive sequence of the machine stator currents. The resulting machine current space vector is given in (3.1).

$$\overrightarrow{i_s} = \left|I_P^f\right| e^{j(\omega_s t+\phi_{iP})} + \left|I_N^f\right| e^{-j(\omega_s t+\phi_{iN})} \tag{3.1}$$

The variables I_P^f and I_N^f represent the magnitudes of the positive and negative sequence components of the machine currents, while ϕ_{iP} and ϕ_{iN} represent their phase angles, re-

spectively. The stator flux linkages is estimated using the relationship described in (3.2).

$$\lambda_s = \int (v_s - r_s i_s)\, dt + \lambda_{s_0} \tag{3.2}$$

The resulting stator flux linkage space vector is described in (3.3).

$$\overrightarrow{\lambda_s^f} = \left|\lambda_P^f\right| e^{j(\omega_s t + \alpha_P)} + \left|\lambda_N^f\right| e^{-j(\omega_s t + \alpha_N)} + \lambda_0 \tag{3.3}$$

Here λ_P^f and λ_N^f are the positive and negative sequence component of the stator flux linkages while α_P and α_N are their phase angles, respectively. As described in (2.27), the electromagnetic torque is directly proportional to the cross product of the current and stator flux linkages. The resulting electromagnetic torque is the sum of three parts, as given in (3.4).

$$t_e = t_{mechanical} + t_{static} + t_{dynamic} \tag{3.4}$$

The machine output torque, $t_{mechanical}$, is produced by the interaction of the positive sequence components of the machine current and flux linkage, described in (3.5)

$$t_{mechanical} = \frac{3P_n}{4}\left(\left|I_P^f\right|\left|\lambda_P^f\right|\sin\left(\phi_{iP} - \alpha_P\right)\right) \tag{3.5}$$

The DC component of the torque t_{static}, described in (3.6), is a function of the negative sequences introduced by the fault occurrence.

$$t_{static} = \frac{3P_n}{4}\left(\left|I_N^f\right|\left|\lambda_N^f\right|\sin\left(\alpha_N - \phi_{iN}\right)\right) \tag{3.6}$$

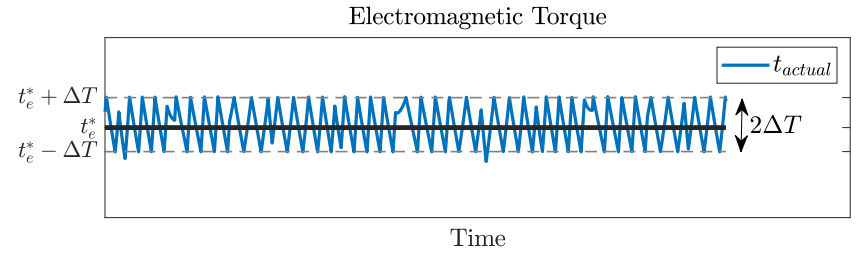

(a) Actual torque variation within torque hysteresis bands.

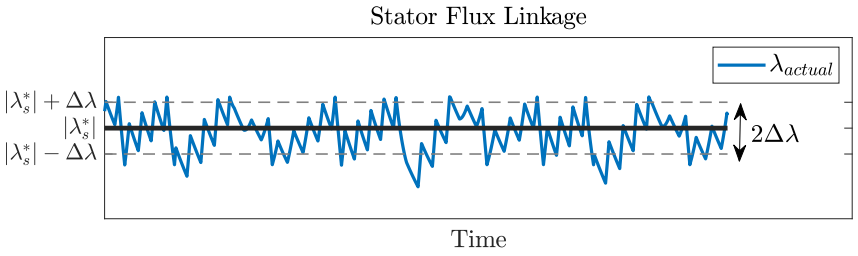

(b) Actual flux variation within flux hysteresis bands.

Figure 3.1: Time behaviour of torque and flux hysteresis comparators.

Finally, $t_{dynamic}$ is a torque component oscillating at double fundamental frequency ($2f_s$), as shown in (3.7), which is introduced in the machine output torque due to the fault occurrence.

$$t_{dynamic} = \frac{3P_n}{4}\left(\left|I_P^f\right|\left|\lambda_N^f\right|\sin\left(2\omega t + \phi_{iP} + \alpha_N\right) + \left|I_N^f\right|\left|\lambda_P^f\right|\sin\left(2\omega t + \phi_{iN} + \alpha_P\right)\right) \quad (3.7)$$

3.1 Response of Flux and Torque Comparators

The DTC technique employs hysteresis comparators to regulate the magnitude of stator flux linkage and electromagnetic torque. The bandwidth in the DTC scenario is determined by the torque and flux hysteresis bands (ΔT and $\Delta\lambda$), respectively. Fig. 3.1 presents the torque and flux variation within the hysteresis bands. The bands can either have fixed values that remain constant regardless of operating conditions [32], or they can be percentages of a preset value based on operating conditions [54]. Alternatively, they can be variables that

enable nearly constant switching frequency [55].

The utilization of wider hysteresis bands leads to a reduction in bandwidth and switching frequency due to the infrequent violation of the hysteresis bands during the control cycle. Conversely, a high controller bandwidth necessitates narrow bands, leading to increased switching frequency due to the likelihood of torque and flux errors exceeding the hysteresis bands during a significant portion of the control cycle. In general, DTC permits deviations in the estimation of flux and torque, provided that they fall within the predetermined tolerance margin established by the hysteresis band. Nonetheless, the estimated torque and flux linkage should follow the reference ones regardless of the machine condition, whether it is healthy or faulty.

3.1.1 Flux Comparator Response

Since a negative sequence component appears in the flux linkages due to its presence on the current, the flux comparator should cancel it by imposing another negative sequence component ($\overrightarrow{\lambda_c}$) in the flux linkage, as described in (3.8)

$$\overrightarrow{\lambda_c} = \left|\lambda_N^f\right| e^{-j(\omega_s t+\alpha_N)} \tag{3.8}$$

As a result, the machine flux linkage would be:

$$\overrightarrow{\lambda_s^h} = \overrightarrow{\lambda_s^f} - \overrightarrow{\lambda_c} = \left|\lambda_P^h\right| e^{j\left(\omega_s t+\phi_{\lambda_s}\right)} + \lambda_0 \tag{3.9}$$

To inject $\overrightarrow{\lambda_c}$, the DTC drive injects the negative sequence component on the reference voltages. The positive, negative, and zero sequence components of the commanded voltages

(V_P, V_N, V_0) are computed using (3.10).

$$\begin{bmatrix} V_P \\ V_N \\ V_0 \end{bmatrix} = \frac{1}{3} \begin{bmatrix} 1 & a & a^2 \\ 1 & a^2 & a \\ 1 & 1 & 1 \end{bmatrix} \begin{bmatrix} V_a \\ V_b \\ V_c \end{bmatrix} \tag{3.10}$$

Here $a = 1\angle 120°$. The resulting sequence components of the commanded voltages in DTC driven PMSM in case of healthy and faulty conditions are depicted in Figs. 3.2 to 3.6. Under normal operating conditions, the negative sequence component is absent because the commanded voltages are balanced. However, in the event of a fault, the commanded voltages become unbalanced, which causes the negative sequence voltage component to appear. This component helps to mitigate the effect of the fault on the stator flux linkage magnitude. As shown in Fig. 3.6, the negative sequence voltage is nearly zero under eccentricity fault as found in the healthy case, Fig. 3.2. It is expected that the DTC operation will still perform well despite the presence of an eccentricity fault.

The flux hysteresis band limits the maximum acceptable change in the stator flux linkage, which in turn limits the negative flux linkage sequence component that can be generated by applying a negative voltage sequence, as expressed in (3.11).

$$\frac{\left|\lambda_N^f\right|}{\left|\lambda_P^f\right|} \approx \frac{2\Delta\lambda}{|\lambda_s|} \tag{3.11}$$

The upper limit of the negative voltage sequence that the DTC flux comparator can apply in response to the flux linkage error is directly related to the flux hysteresis band, as described

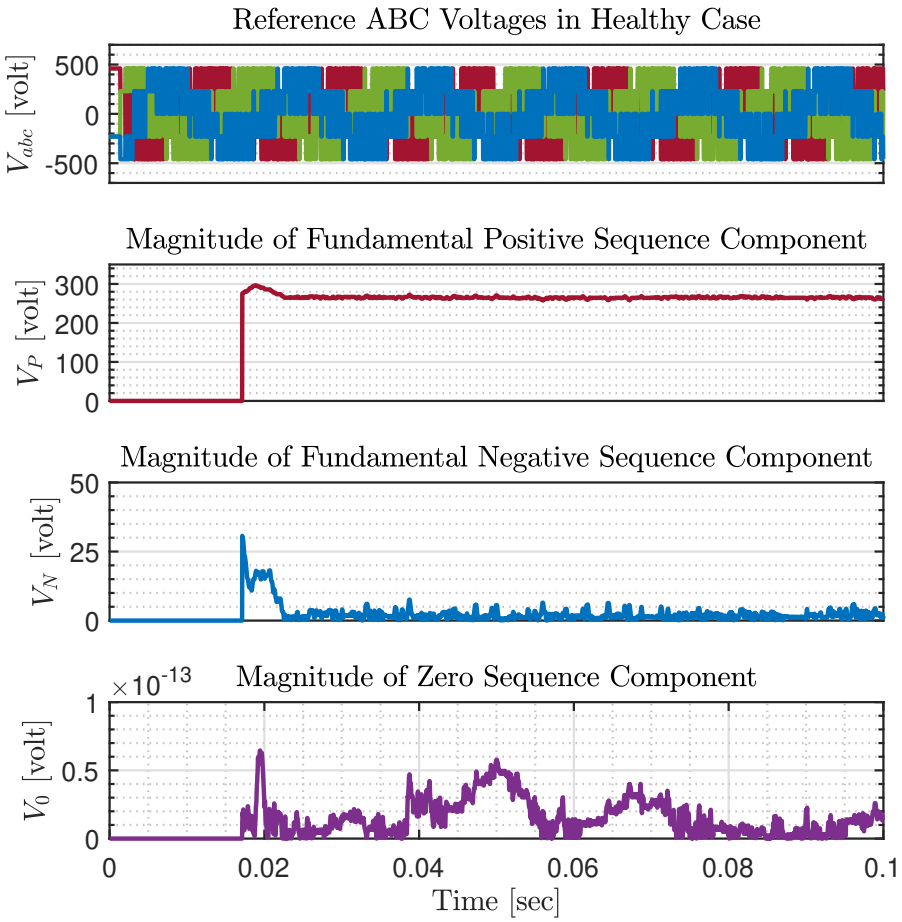

Figure 3.2: Sequence components analysis of the commanded voltages in DTC driven PMSM under healthy condition.

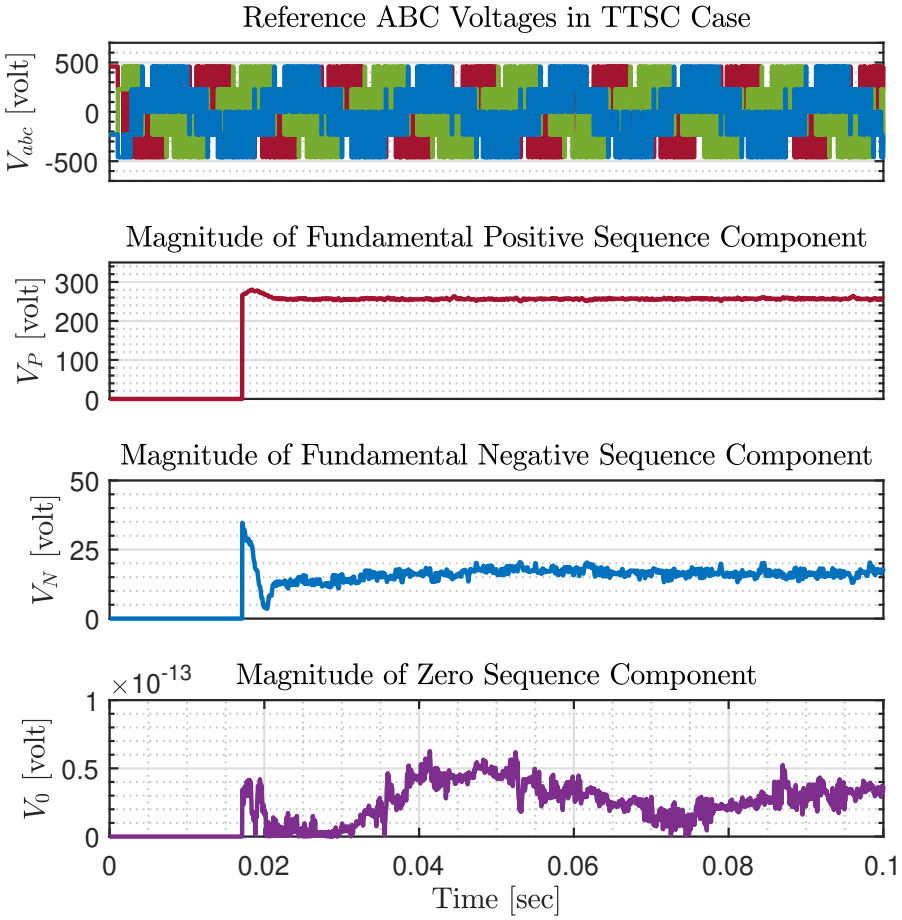

Figure 3.3: Sequence components analysis of the commanded voltages in DTC driven PMSM under TTSC fault.

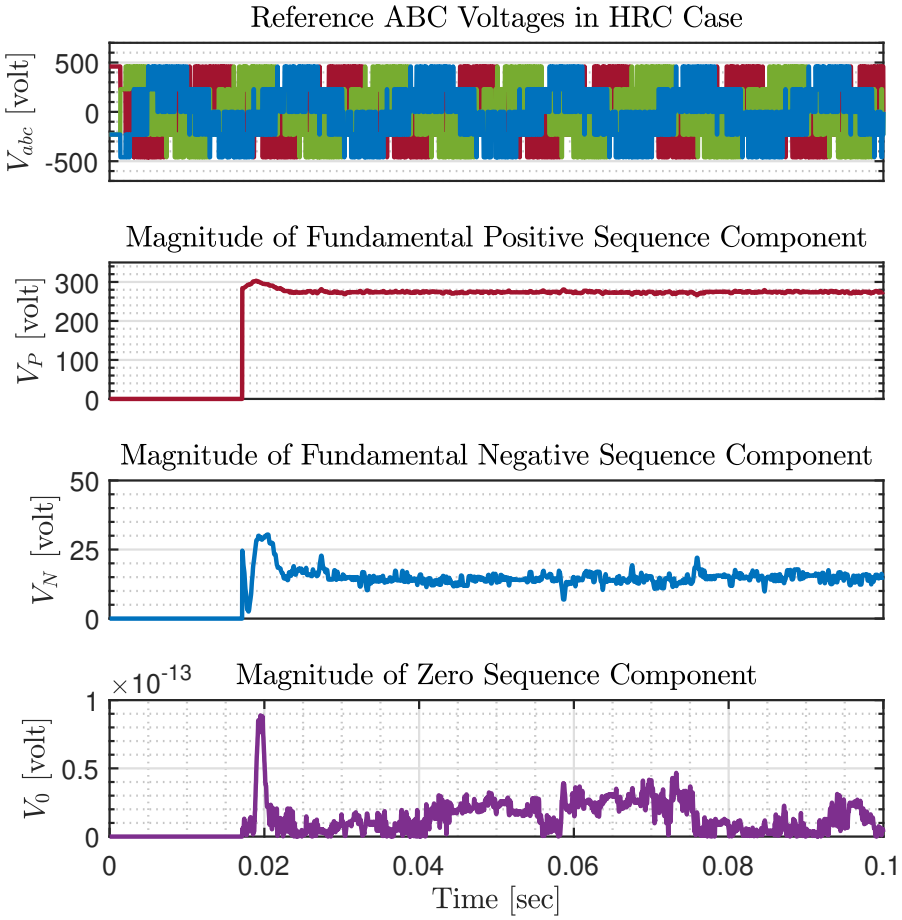

Figure 3.4: Sequence components analysis of the commanded voltages in DTC driven PMSM under HRC fault.

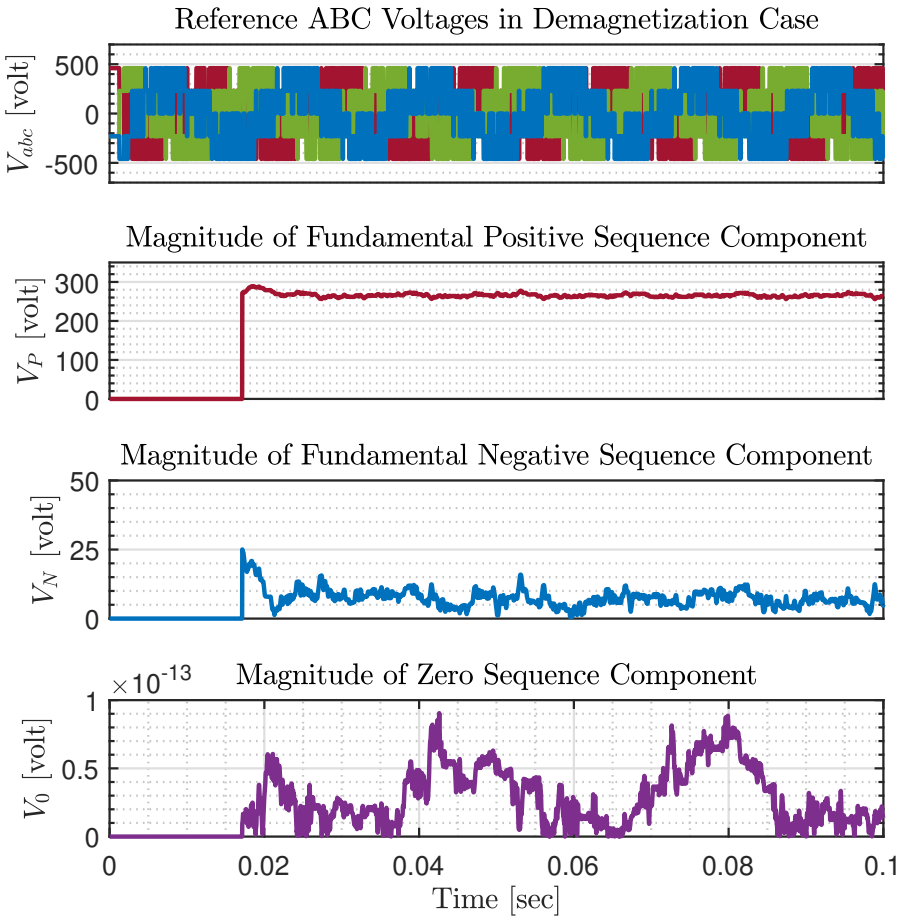

Figure 3.5: Sequence components analysis of the commanded voltages in DTC driven PMSM under demagnetization fault.

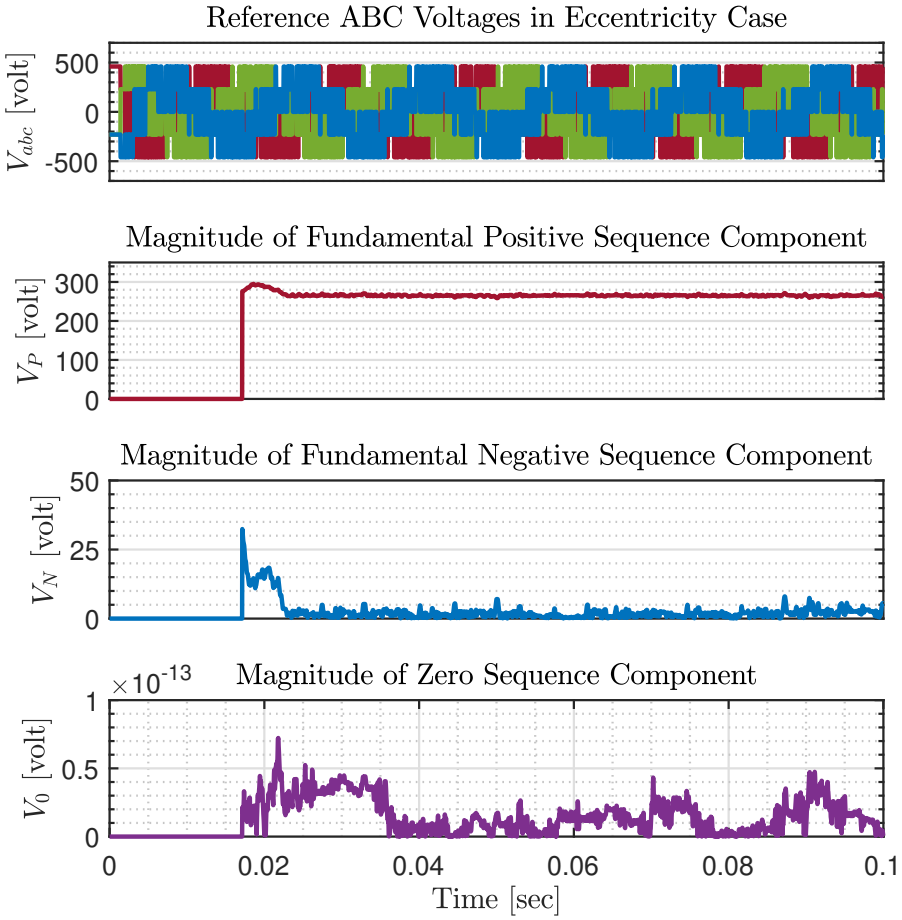

Figure 3.6: Sequence components analysis of the commanded voltages in DTC driven PMSM under eccentricity fault.

by (3.12).

$$\frac{|V_N|}{|V_P|} \approx \frac{2\Delta\lambda}{|\lambda_s|} \tag{3.12}$$

As a result of (3.8), the static torque error in (3.6) and the first term of (3.7) are cancelled. However, the second term of the torque dynamic error in (3.7) remains. This error is tolerated by DTC as long as this error falls within the hysteresis band of the torque comparator. However, if the error exceeds the maximum allowable torque error, the torque comparator must find an alternative method to compensate for it.

Recalling the torque equation given in (2.30), the torque angle (δ) is the other variable that can be adjusted to maintain the desired torque. The torque is comprised of two components: the magnetic torque (t_m) and the reluctance torque (t_{re}), as shown in (3.13).

$$\begin{aligned} t_e &= t_m + t_{re} \\ t_m &= A \cdot \sin(\delta) = Im\left[Ae^{j\delta}\right] \\ t_{re} &= B \cdot \sin(2\delta) = Im\left[Be^{j2\delta}\right] \\ A &= \frac{3P_n\lambda_s\lambda_{PM}}{4L_d} \\ B &= \frac{3P_n\lambda_s^2(L_d - L_q)}{8L_dL_q} \end{aligned} \tag{3.13}$$

The torque angle (δ) represents the difference between the stator flux linkage angle (θ_s) and the rotor flux linkage angle (θ_r). DTC has the capability to adjust the stator flux linkage vector during the transient conditions to either accelerate it to increase the torque angle and generate additional torque, or decelerate it to reduce the torque angle and produce less torque. In steady state conditions, the stator flux linkage vector is rotating at the same speed as the rotor flux linkage vector where the torque is constant. The two variables

that DTC can change are λ_s and δ. However, λ_s is almost fixed as it is controlled by the flux comparator. Therefore, the only option for DTC to respond to the torque error is by manipulating the torque angle.

3.1.2 Torque Comparator Response

The regulation of output torque in DTC drive is achieved through the use of a torque hysteresis comparator. As a result, it is expected that the output torque will conform to the torque reference regardless of the condition of the machine.

According to [56], the PMSM torque ripple exhibits harmonic orders that are multiples of the sixth harmonic, $f_{t_{ripple}} = 6 \cdot k \cdot f_s$, where f_s is the machine electric frequency and $k = 1, 2, 3, \ldots$. The frequency spectrum of the torque produced by IPMSM driven by FOC and DTC are provided in Fig. 3.7. It is evident that the FOC driven PMSM exhibits

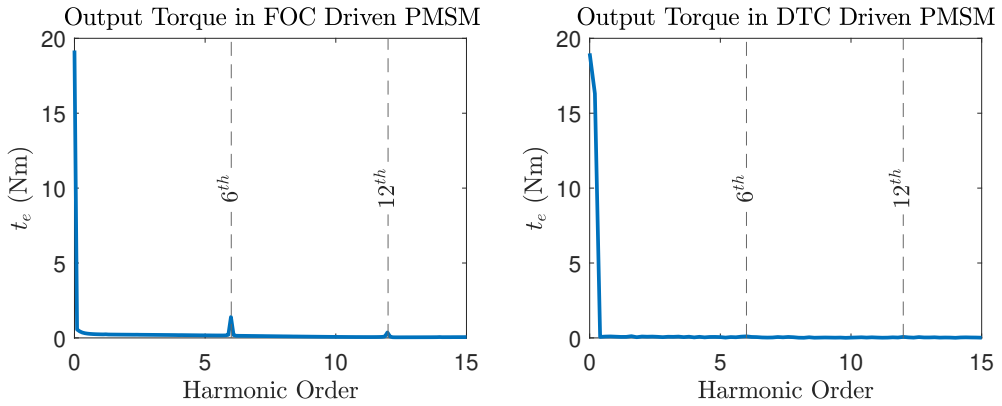

Figure 3.7: Frequency spectrum of the produced torque by IPMSM under FOC and DTC drives.

significant magnitudes of the 6^{th} and 12^{th} harmonics in its output torque, whereas such high magnitudes are not observable in the case of DTC. If the torque ripple caused by the 6^{th} and 12^{th} harmonics falls outside the torque hysteresis bands ($2\Delta T$), DTC will attempt to compensate for it in order to maintain the torque error within the band. Since the DTC

drive provides the ability to adjust the torque angle (δ), any induced harmonics are expected to manifest in the torque angle instead of the torque signal. This can be observed in the frequency spectrum of the torque angle depicted in Fig. 3.8.

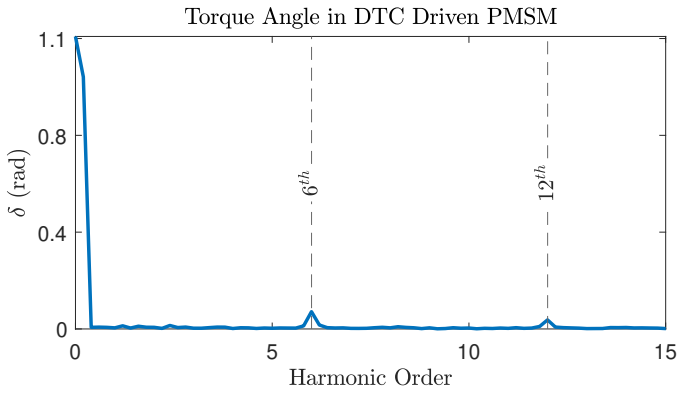

Figure 3.8: Frequency spectrum of the torque angle in DTC driven PMSM.

Introducing the 6^{th} and 12^{th} harmonics into the torque angle for both the magnetic and reluctance torque equations results in (3.14) and (3.15).

$$\begin{aligned} t_{m_1} &= A \cdot \sin(\delta + m) = Im\left[Ae^{j(\delta+m)}\right] \\ m &= x_6 \cos(6\delta + \gamma_6) + x_{12} \cos(12\delta + \gamma_{12}) \end{aligned} \tag{3.14}$$

$$\begin{aligned} t_{re_1} &= B \cdot \sin(2\delta + d) = Im\left[Be^{j(2\delta+d)}\right] \\ d &= 2x_6 \cos(6\delta + \gamma_6) + 2x_{12} \cos(12\delta + \gamma_{12}) \end{aligned} \tag{3.15}$$

The terms x_6, x_{12}, γ_6, and γ_{12} correspond to the amplitudes and phases of the 6^{th} and 12^{th} harmonics present in the frequency spectrum of the torque angle. The trigonometric identity described in (3.16) is used to expand the electromagnetic and reluctance torque equations as shown in (3.17) and (3.18).

$$\sin(x + y) = \sin(x)\cos(y) + \sin(y)\cos(x) \tag{3.16}$$

$$t_{m_1} = t_m \cos(m) + A \cdot \cos(\delta) \sin(m) \tag{3.17}$$

$$t_{re_1} = t_{re} \cos(d) + B \cdot \cos(2\delta) \sin(d) \tag{3.18}$$

By considering the presence of the 6^{th} and 12^{th} harmonics in the torque angle frequency spectrum, it can be observed that the magnitudes of t_m and t_{re} are subject to multiplication by $\cos(m)$ and $\cos(d)$, respectively. Nonetheless, their effect on t_m and t_{re} is negligible, as their magnitude is almost unity as illustrated in Fig. 3.9.

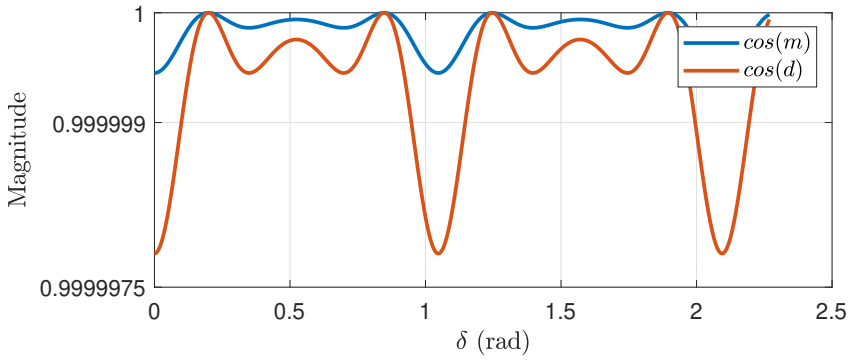

Figure 3.9: The magnitude of $\cos(m)$ and $\cos(d)$.

The inclusion of the 6^{th} and 12^{th} harmonics lead to additional terms in t_m and t_{re}. These terms are $A \cdot \cos(\delta) \sin(m)$ and $B \cdot \cos(2\delta) \sin(d)$. However, it is found that these terms mostly offset each other and hence their overall effect on the torque is negligible, as depicted in Fig. 3.10.

In summary, the DTC drive has the capability to incorporate the 6^{th} and 12^{th} harmonics in the torque angle instead of the torque signal itself. Although these additional harmonics are present, they have a negligible impact on the torque signal. As a result, the DTC drive can maintain the torque error within the torque hysteresis bands. This nonlinear behavior of the torque hysteresis comparator justifies the compensation of the second term of dynamic torque error in (3.7) due to the fault presence through the manipulation of the torque angle.

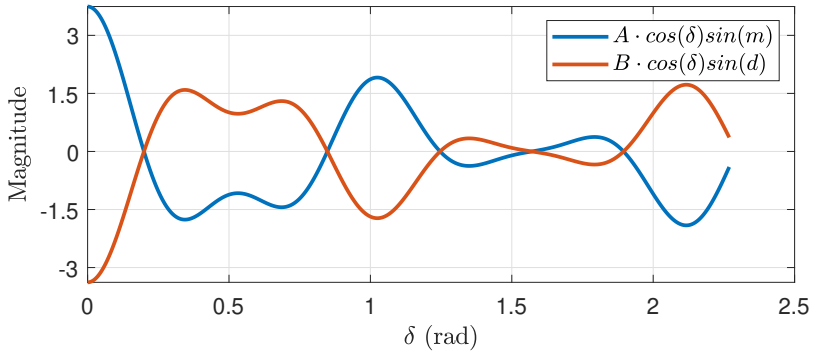

Figure 3.10: The magnitude of the offset error in (3.17) and (3.18).

3.2 Flux and Torque Estimation

Accurate estimation of the torque and magnetic flux linkage is crucial for maintaining stable operation of DTC driven PMSM. Such estimation is based on operating the machine in healthy conditions. However, occurrence of faults induces dynamics that are not captured by the estimation models used in DTC drive. Ignoring the unmodeled fault dynamics causes estimation errors and leads to unstable operation during severe faults [53]. Hence, it is imperative to evaluate the impact of the machine health condition on the accuracy of flux estimation. It was shown in Chapter 3.1 that the negative sequence introduced by an eccentricity fault is compensated by the flux and torque comparators. For this reason, the following sections present the flux linkage model for TTSC, HRC, and demagnetization faults only.

3.2.1 Case of TTSC

The PMSM model under TTSC fault is given in Fig. 3.11 and (3.19). Here r_{s_h}, L_{s_h}, and e_{s_h} are the resistance, inductance, and back-EMF of the healthy turns. r_{s_f}, L_{s_f}, and e_{s_f} are the resistance, inductance, and back-EMF of the shorted turns. L_{hf} is the mutual inductance between healthy and faulty turns of the faulted phase. i_f is the fault circulating current in

the short circuit path between the healthy and faulted turns.

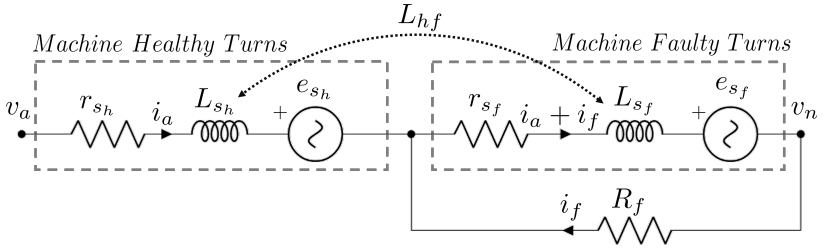

Figure 3.11: Phase A electrical model of a PMSM with TTSC fault.

$$\begin{bmatrix} v_a \\ v_b \\ v_c \\ 0 \end{bmatrix} = \begin{bmatrix} r_s & 0 & 0 & r_{s_f} \\ 0 & r_s & 0 & 0 \\ 0 & 0 & r_s & 0 \\ r_{s_f} & 0 & 0 & r_{s_f} + R_f \end{bmatrix} \begin{bmatrix} i_a \\ i_b \\ i_c \\ i_f \end{bmatrix} + \begin{bmatrix} L_s & 0 & 0 & L_{hf} + L_{s_f} \\ 0 & L_s & 0 & 0 \\ 0 & 0 & L_s & 0 \\ L_{hf} + L_{s_f} & 0 & 0 & L_{s_f} \end{bmatrix} \begin{bmatrix} \frac{di_a}{dt} \\ \frac{di_b}{dt} \\ \frac{di_c}{dt} \\ \frac{di_f}{dt} \end{bmatrix} + \begin{bmatrix} e_a \\ e_b \\ e_c \\ e_{s_f} \end{bmatrix} \tag{3.19}$$

Since DTC operates in the stationary ($\alpha\beta$) frame, it is then suitable to transform the faulty PMSM model into ($\alpha\beta$) frame using the transformation matrix given in (3.20).

$$T = \frac{2}{3} \begin{bmatrix} 1 & -\frac{1}{2} & -\frac{1}{2} & 0 \\ 0 & \frac{\sqrt{3}}{2} & -\frac{\sqrt{3}}{2} & 0 \\ \frac{1}{2} & \frac{1}{2} & \frac{1}{2} & 0 \\ 0 & 0 & 0 & \frac{3}{2} \end{bmatrix} \tag{3.20}$$

The resulting faulty PMSM model in $\alpha\beta$ frame is given in (3.21).

$$\begin{bmatrix} v_\alpha \\ v_\beta \\ v_o \\ v_f \end{bmatrix} = \begin{bmatrix} r_s & 0 & 0 & \frac{2}{3}r_{s_f} \\ 0 & r_s & 0 & 0 \\ 0 & 0 & r_s & \frac{1}{3}r_{s_f} \\ r_{s_f} & 0 & 0 & r_{s_f} + R_f \end{bmatrix} \begin{bmatrix} i_\alpha \\ i_\beta \\ i_o \\ i_f \end{bmatrix} + \begin{bmatrix} L_s & 0 & 0 & \frac{2}{3}(L_{hf} + L_{s_f}) \\ 0 & L_s & 0 & 0 \\ 0 & 0 & L_s & \frac{1}{3}(L_{hf} + L_{s_f}) \\ L_{hf} + L_{s_f} & 0 & L_{hf} + L_{s_f} & L_{s_f} \end{bmatrix} \begin{bmatrix} \frac{di_\alpha}{dt} \\ \frac{di_\beta}{dt} \\ \frac{di_o}{dt} \\ \frac{di_f}{dt} \end{bmatrix} + \begin{bmatrix} e_\alpha \\ e_\beta \\ 0 \\ e_{s_f} \end{bmatrix} \tag{3.21}$$

The α-axis voltage, from the first row in (3.21), is given in (3.22).

$$\begin{aligned} v_\alpha &= r_s i_\alpha + L_s \frac{di_\alpha}{dt} + e_\alpha + \frac{2}{3} r_{s_f} i_f + \frac{2}{3}\left(L_{hf} + L_{s_f}\right)\frac{di_f}{dt} \\ &= r_s i_\alpha + \frac{d\lambda_\alpha}{dt} + \frac{2}{3} r_{s_f} i_f + \frac{2}{3}\left(L_{hf} + L_{s_f}\right)\frac{di_f}{dt} \end{aligned} \tag{3.22}$$

The α axis voltage is used for flux estimation under TTSC fault, as described in (3.23), contains additional terms due to the TTSC fault.

$$\lambda_\alpha = \int \left(v_\alpha - r_s i_\alpha - \frac{2}{3} r_{s_f} i_f\right) dt - \frac{2}{3}\left(L_{hf} + L_{s_f}\right) i_f + \lambda_{\alpha_0} \tag{3.23}$$

The resulting stator flux estimation error increases with the fault severity, as shown in Figs. 3.12 and 3.13. The deviation in angle, θ_s, may result in the inappropriate choice of voltage vectors to sustain the stator flux linkages within the flux hysteresis bands. The stability of DTC heavily relies on accurate flux estimation, if the estimation error becomes

significant it could ultimately result in unstable control [53].

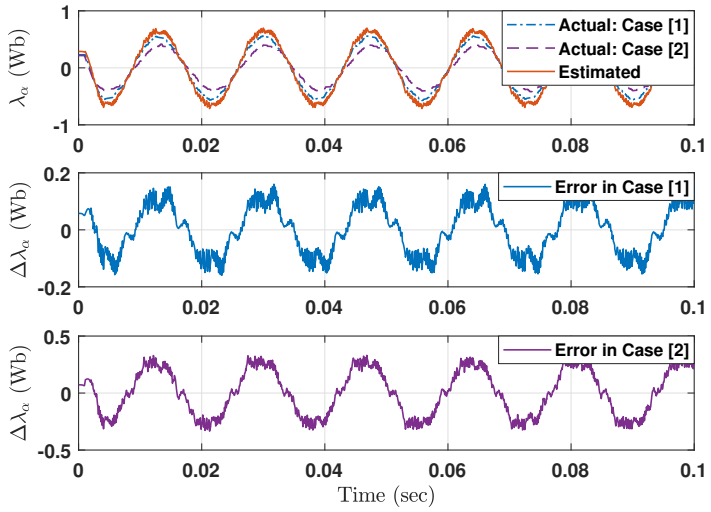

Figure 3.12: Difference in magnitude between actual and estimated α-axis stator flux linkage under ITSC fault, where case [1] is ($i_f = 25\%I_{rated}$) and case [2] is ($i_f = 32\%I_{rated}$) at single operating point.

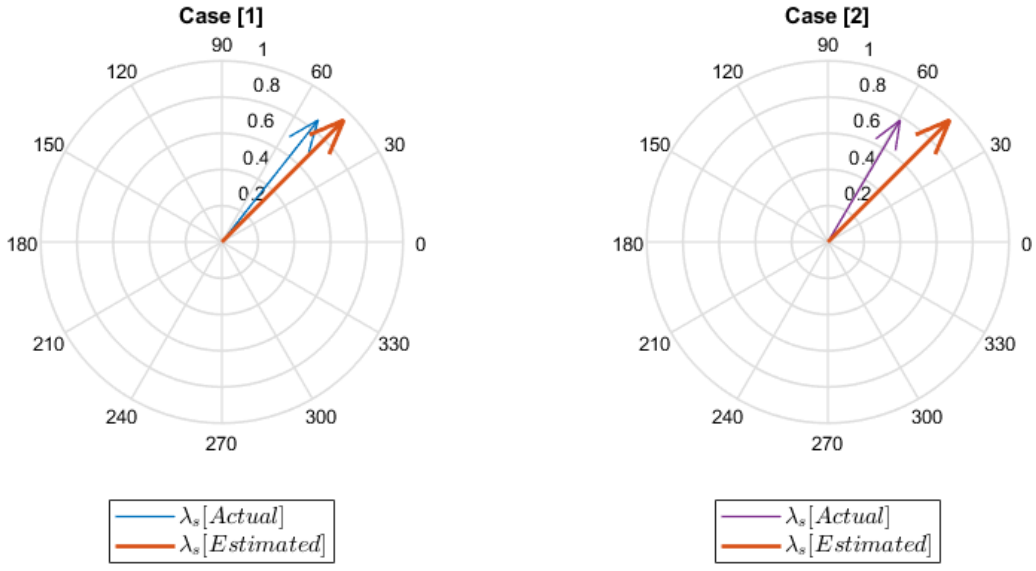

(a) $i_f = 25\%I_{rated}$.

(b) $i_f = 32\%I_{rated}$.

Figure 3.13: Error in magnitude and angle of the stator flux linkage under ITSC fault at single operating point.

3.2.2 Case of HRC

The PMSM model under HRC fault, given in (3.24), assuming the fault occurs in phase B connection, can be derived from in *abc* frame from the circuit shown in Fig. 3.14

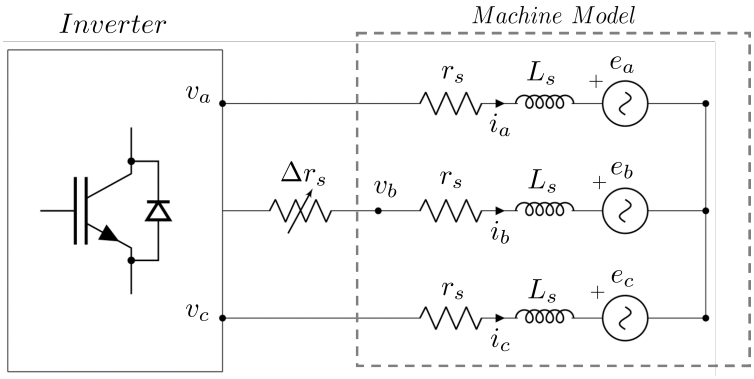

Figure 3.14: PMSM electrical model with HRC fault at Phase B terminal.

$$\begin{bmatrix} v_a \\ v_b \\ v_c \end{bmatrix} = \begin{bmatrix} r_s & 0 & 0 \\ 0 & r_s + \Delta r_s & 0 \\ 0 & 0 & r_s \end{bmatrix} \begin{bmatrix} i_a \\ i_b \\ i_c \end{bmatrix} + \begin{bmatrix} L_s & 0 & 0 \\ 0 & L_s & 0 \\ 0 & 0 & L_s \end{bmatrix} \begin{bmatrix} \frac{di_a}{dt} \\ \frac{di_b}{dt} \\ \frac{di_c}{dt} \end{bmatrix} + \begin{bmatrix} e_a \\ e_b \\ e_c \end{bmatrix} \tag{3.24}$$

The faulty PMSM model is then transformed into $\alpha\beta$ frame using the following transformation matrix given in (3.25)

$$T = \frac{2}{3} \begin{bmatrix} 1 & -\frac{1}{2} & -\frac{1}{2} \\ 0 & \frac{\sqrt{3}}{2} & -\frac{\sqrt{3}}{2} \\ \frac{1}{2} & \frac{1}{2} & \frac{1}{2} \end{bmatrix} \tag{3.25}$$

The resulting faulty PMSM model in $\alpha\beta$ frame is given in (3.26).

$$\begin{bmatrix} v_\alpha \\ v_\beta \\ v_o \end{bmatrix} = \begin{bmatrix} r_s + \frac{\Delta r_s}{2} & \frac{-\Delta r_s}{2\sqrt{3}} & -\frac{\Delta r_s}{3} \\ \frac{-\Delta r_s}{2\sqrt{3}} & r_s + \frac{\Delta r_s}{2} & -\frac{\Delta r_s}{3} \\ -\frac{\Delta r_s}{2} & \frac{\Delta r_s}{2\sqrt{3}} & r_s + \frac{\Delta r_s}{3} \end{bmatrix} \begin{bmatrix} i_\alpha \\ i_\beta \\ i_o \end{bmatrix} + \begin{bmatrix} L_s & 0 & 0 \\ 0 & L_s & 0 \\ 0 & 0 & L_s \end{bmatrix} \begin{bmatrix} \frac{di_\alpha}{dt} \\ \frac{di_\beta}{dt} \\ \frac{di_o}{dt} \end{bmatrix} + \begin{bmatrix} e_\alpha \\ e_\beta \\ 0 \end{bmatrix} \tag{3.26}$$

The α axis voltage, given in (3.27), can be used for flux estimation under HRC fault, as described in (3.28).

$$\begin{aligned} v_\alpha &= (r_s + \frac{\Delta r_s}{2})i_\alpha - (\frac{\Delta r_s}{2\sqrt{3}})i_\beta - (\frac{\Delta r_s}{3})i_o + L_s\frac{di_\alpha}{dt} + e_\alpha \\ &= r_s i_\alpha + \frac{d\lambda_\alpha}{dt} - (\frac{\Delta r_s}{2\sqrt{3}})i_\beta - (\frac{\Delta r_s}{3})i_o + (\frac{\Delta r_s}{2})i_\alpha \end{aligned} \tag{3.27}$$

$$\lambda_\alpha = \int (v_\alpha - r_s i_\alpha - (\frac{\Delta r_s}{2})i_\alpha - (\frac{\Delta r_s}{2\sqrt{3}})i_\beta - (\frac{\Delta r_s}{3})i_o)dt + \lambda_{\alpha 0} \tag{3.28}$$

Similarly, the flux estimation under HRC fault in β axis is given in (3.29).

$$\lambda_\beta = \int (v_\beta - r_s i_\beta - (\frac{\Delta r_s}{2})i_\beta - (\frac{\Delta r_s}{2\sqrt{3}})i_\alpha - (\frac{\Delta r_s}{3})i_o)dt + \lambda_{\beta 0} \tag{3.29}$$

It is clear from (3.28) and (3.29) that the flux estimation under HRC fault includes additional terms.

The differences ($\Delta\lambda_\alpha$) in magnitude between actual and estimated stator flux linkage in (α) axis under HRC fault are shown in Figs. 3.15 and 3.16. It is worth noting that the $\alpha\beta$ flux

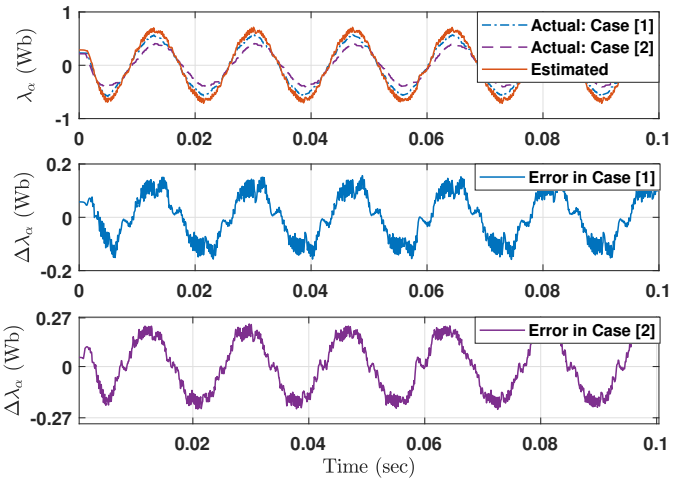

Figure 3.15: Difference in magnitude between actual and estimated stator flux linkage in (α) axis under HRC fault, where case [1] is ($100\%r_s$ increase) and case [2] is ($150\%r_s$ increase) at single operating point.

linkages will be equally affected, leading to no change in the angle of the stator flux linkage, as shown in Fig. 3.16. Authors in [57,58] observe that DTC drive may experience instability

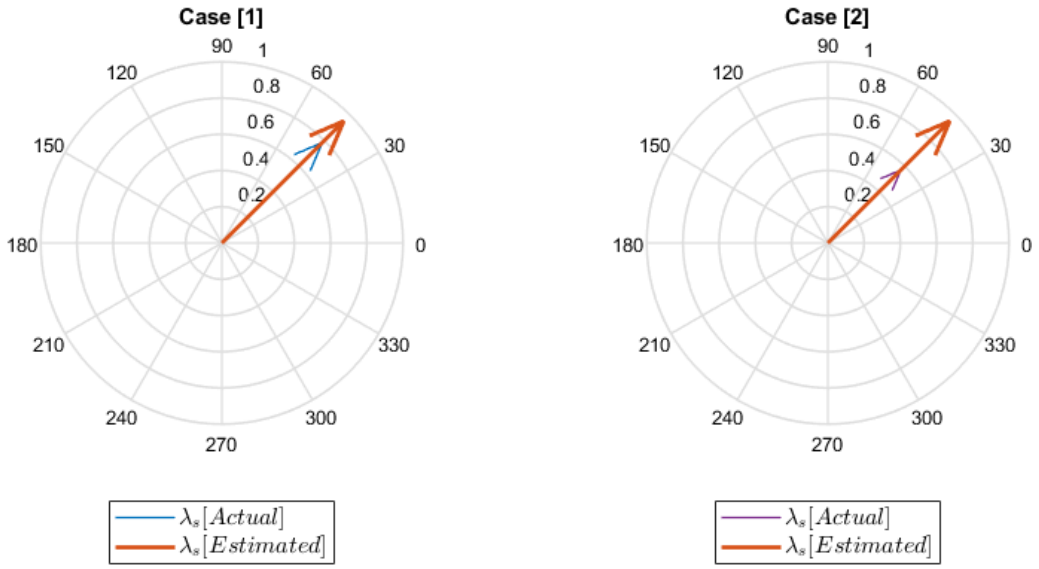

(a) $100\%r_s$ increase.)

(b) $150\%r_s$ increase.

Figure 3.16: Error in magnitude and angle of the stator flux linkage under HRC fault at single operating point.

under severe HRC conditions. Therefore, additional attention should be considered if the

HRC fault exists in case of DTC drives.

3.2.3 Case of Partial Demagnetization

The effect of demagnetization in the flux linkage estimators is represented by the magnet flux linkage reduction (Γ_0) as shown in (3.30).

$$\lambda_{\alpha\beta} = \int \left(v_{\alpha\beta} - r_s i_{\alpha\beta}\right) dt + \left(\lambda_{\alpha_0\beta_0} - \Gamma_0\right) \tag{3.30}$$

As shown in Figs. 3.17 and 3.18, there is a shift in both the magnitude and angle of the stator flux linkage resulting from the demagnetization fault.

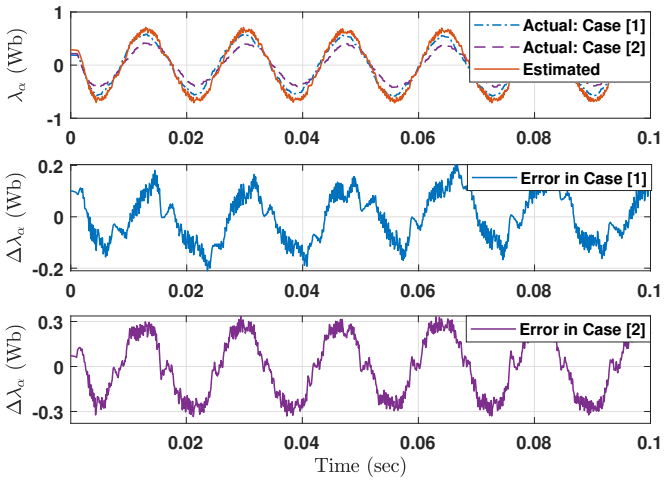

Figure 3.17: Difference in magnitude between actual and estimated stator flux linkage in (α) axis under demagnetization fault, where case [1] is ($6\%\lambda_{PM}$ reduction) and case [2] is ($14\%\lambda_{PM}$ reduction) at single operating point.

As the severity of the fault increases and the deviation between the estimated and actual flux linkage becomes more significant and may eventually lead to unstable control. This is due to the fact that the commanded stator flux linkage in DTC driven PMSMs should satisfy

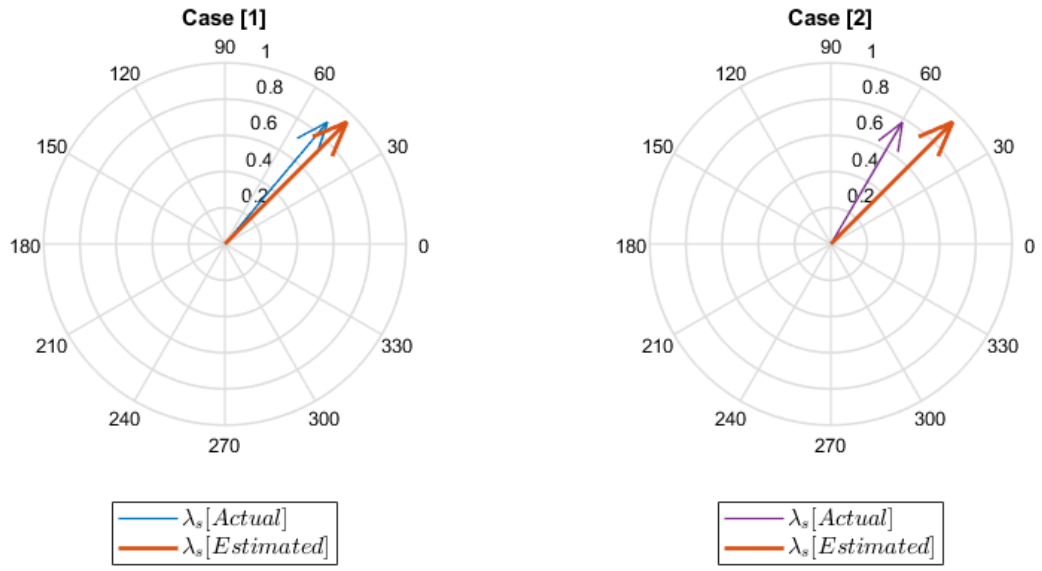

(a) $6\%\lambda_{PM}$ reduction.

(b) $14\%\lambda_{PM}$ reduction.

Figure 3.18: Error in magnitude and angle of the stator flux linkage under demagnetization fault at single operating point.

the threshold given in (3.31) to ensure stability [28].

$$\lambda_s < \left| \frac{L_q}{L_q - L_d} \right| \lambda_{PM} \tag{3.31}$$

As the threshold parameters vary, the region of stable drive operation will change. Authors in [59] show that as the severity of the demagnetization fault increases, the magnet flux linkage λ_{PM} decays faster than the inductance difference $(L_q - L_d)$. As a result, the stable drive area of DTC would decrease drastically under demagnetization fault due to the reduction in the upper limit in (3.31).

3.3 Impact of Variations in Stator Flux Linkage Angle

The robustness and tolerance of DTC can also be attributed to its discrete control action, which involves selecting a finite set of possible actions rather than continuous modulation.

The finite set of actions, namely the voltage vectors, is chosen based on heuristics and system dynamics, whereby an exact position of the stator flux linkage vector is not necessary. Fig. 3.19 presents the sector partitions and voltage vectors available for selection in DTC. It consists of six voltage vectors ($V_1 - V_6$) within six sectors ($S_1 - S_6$) that are displaced by 60°.

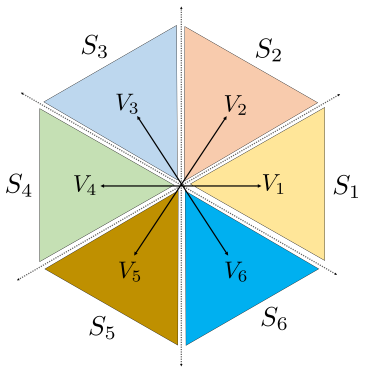

Figure 3.19: Sector partitions and the available set of voltage vectors in DTC drive.

Provided that the actual and estimated stator flux linkage vectors are in the same sector, identical voltage vectors will be applied. However, if they are situated at the boundaries between sectors, different voltage vectors are applied, which will lead to a deviation in both desired torque and flux. For illustration purposes, the error in estimating the flux caused by the fault has assumed to result in the estimated stator flux linkage vector ($|\lambda|_{est}$) being in the second sector, while it is assumed that the actual vector ($|\lambda|_{act}$) is in the third sector as depicted in Fig. 3.20. It is clear that the estimated value of $|\lambda_s|$ is higher than the reference value, which requires the selection of a voltage vector that can reduce the estimated value of $|\lambda_s|$. By assuming that the electromagnetic torque should be increased at this instant, the voltage vector (V_4) should be applied to the estimated stator flux linkage based on Table 2.1 since it lies the in second sector. Fig. 3.21 presents the trace of ($|\lambda|_{est}$) where (V_4) results in moving the vector from second sector to the third one. Subsequently, a varying pattern

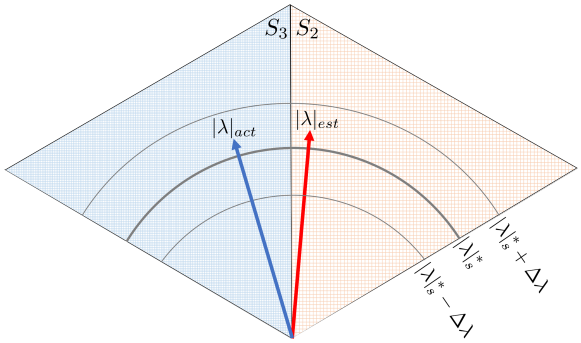

Figure 3.20: Error between actual and estimated stator flux linkages in case of fault occurrence.

is introduced now between V_4 and V_5 to the estimated stator flux linkage vector, which is located in the third section, in order to align it with the reference vector.

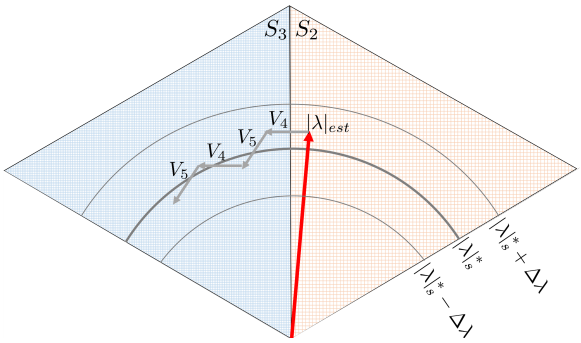

Figure 3.21: Estimated stator flux linkage trace.

Nonetheless, when dealing with the actual stator flux linkage vector, the voltage vector (V_5) must be utilized because the flux vector is situated in the third sector. This decision is supported by the information provided in Table 2.1, where a decrease in flux linkage is required while simultaneously increasing torque. Fig. 3.22 depicts the trace of the actual stator flux linkage vector in case of the voltage vector (V_5) is applied first.

As the feedback loop of DTC relies on the estimated stator flux linkage signal instead of the actual one, the actual stator flux linkage vector will follow the same voltage vector pattern illustrated in Fig. 3.21. However, this can cause inaccuracies in the control process, leading to differences between the actual stator flux linkage magnitude and the desired reference

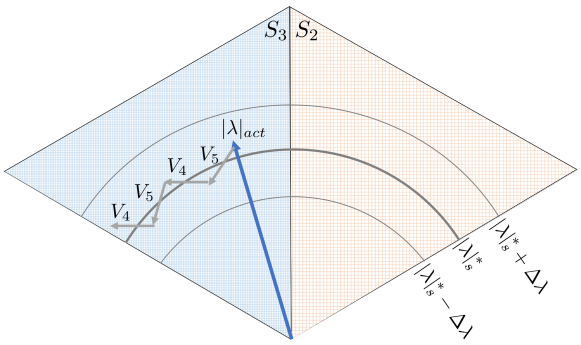

Figure 3.22: Optimal trace of the actual stator flux linkage.

value as shown in Fig. 3.23, even if the estimated value is shown to be properly regulated. The actual stator flux linkage will be adjusted to a new reference position that takes into account the offset caused by the erroneous control action. Nonetheless, if the error is not substantial, it may be within the hysteresis bands.

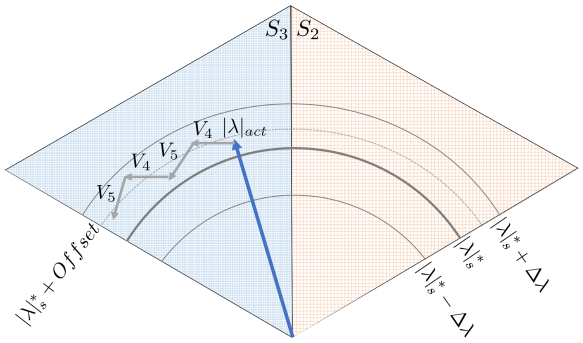

Figure 3.23: Actual trace of the actual stator flux linkage.

Chapter 4

Numerical and Experimental Setup

4.1 Healthy Machine Modeling and Control

To develop a fault diagnosis approach, it is necessary to model the PMSM in the healthy case and use the obtained measurement as a reference in case a fault occurs. Any deviation from the processed healthy data could be considered as fault symptoms. In order to implement these faults in the PMSM (2D-FE) model, geometric and electrical modifications should be made. The main electric parameters of the studied PMSM, PMSM [B], are mentioned in Table 2.2 and the geometrical parameters are listed in Table 4.1. The 2D model of the

Table 4.1: PMSM [B] Parameters.

Parameter	Symbol	Value
Number of slots	Q	12
Turns per slot	N_s	150
Air gap length	g	1 mm
Residual flux density	B_r	1.2 T
Mutual inductance	M_s	$\approx$ 0 H
Rated Phase Current	I_{rms}	18 A
Rated Line Voltage	V_{rms}	480 V

simulated PMSM in ANSYS MAXWELL software is depicted in Fig. 4.1. It can be observed that the machine winding of each phase are wound around a single tooth. This winding configuration is referred as concentrated winding machine where the winding are physically isolated and, therefore, the mutual inductance is negligible.

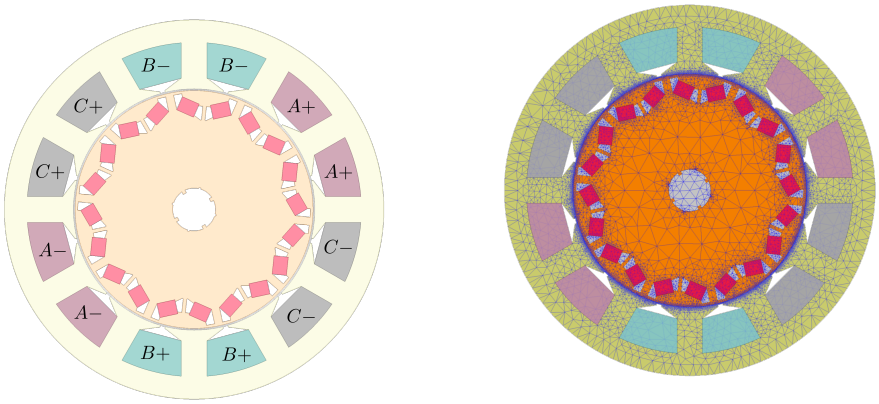

(a) Finite element machine model. (b) Mesh of the machine model.

Figure 4.1: The FEM model of studied PMSM machine.

Following the method in [37], the MTPA profile at different current levels, shown in Fig. 4.2, is evaluated to identify the optimal current angle. It can be observed that the stator current vector should be excited at $\beta = 30°$ for FOC to get the maximum torque for the given current. For DTC, the stator flux linkage (λ_s) was changed in steps of 0.25 Wb

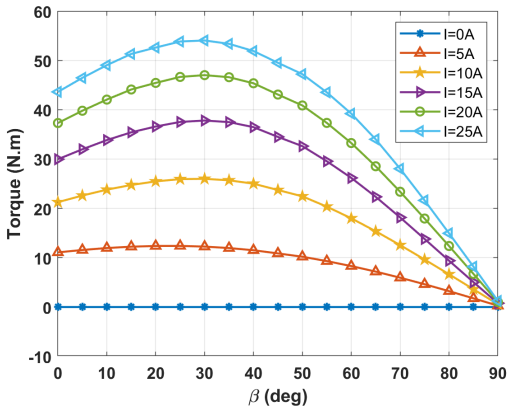

Figure 4.2: Maximum torque per amps profile for FOC driven PMSM [B].

from the permanent magnet flux linkage to the rated one at different operating torque levels. The corresponding stator flux linkage is stored for each torque level in a look-up table where the minimum stator current is achieved. Fig. 4.3 shows the machine MTPA profile for the operating torque range.

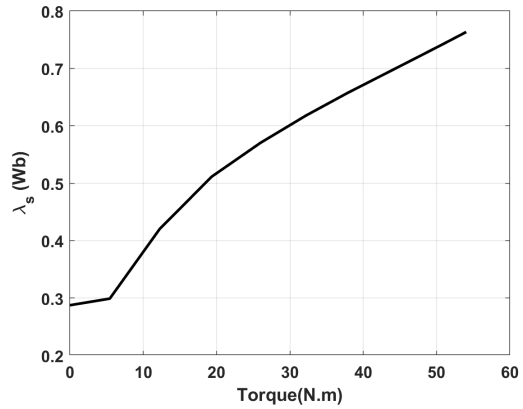

Figure 4.3: Maximum torque per amps profile for DTC driven PMSM [B].

4.2 Fault Implementation

4.2.1 Turn-to-turn Short Circuit

The implementation of TTSC fault requires modification to the electric circuit in SIMPLORER to insert the short circuit path with fault resistance (R_f) between the turns of a faulted phase. Besides that, modification to the geometrical model in MAXWELL has to be made by dividing the coil area into two distinct areas. One area represents the faulty turns and the other represents the remaining healthy turns. Fig. 4.4 shows the PMSM model and the phase A circuit with TTSC fault assuming the phase A is the faulted one. Here r_{s_h} and r_{s_f} are the resistance of the healthy and shorted turns.

Four fault severity levels are considered by varying the short circuit resistance R_f value, and the shorted turns number N_f as shown in Table 4.2.

Table 4.2: Severity levels of TTSC fault in PMSM [B].

Case	N_f	R_f
SC1	15	0.5 Ω
SC2	30	0.25 Ω
SC3	15	0.5 Ω
SC4	30	0.25 Ω

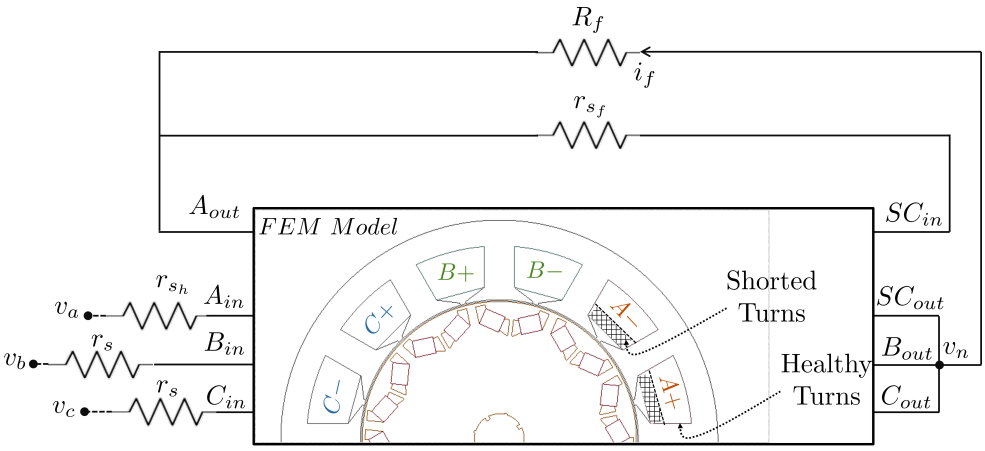

Figure 4.4: Ansys MAXWELL and SIMPLORER model with TTSC fault circuit on phase A winding.

4.2.2 High Resistance Contact

The implementation of HRC fault requires only a modification to the SIMPLORER circuit where a resistance (Δr_s) is connected in series with the faulted phase resistance as shown in Fig. 4.5. The most extreme case of HRC fault is when a relatively large fault resistance

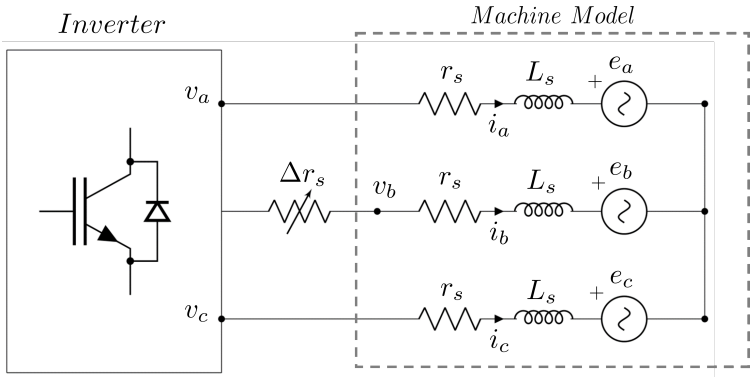

Figure 4.5: PMSM electrical model with HRC fault.

is connected with the phase resistance. This situation is considered an open phase fault. For HRC fault study, assuming the fault occurs at phase B, three levels of fault severity are studied as shown in Table 4.3.

Table 4.3: Severity levels of HRC fault in PMSM [B].

Case	$\frac{\Delta r_s}{r_s}\%$
HRC1	50%
HRC2	100%
HRC3	150%

4.2.3 Static Eccentricity

The machine is considered healthy if the stator and rotor geometrical centers are concentric with the rotational axis. If the rotor center and rotational axis are shifted from the stator center by a constant value, the machine is considered eccentric. Fig. 4.6 shows the rotor and the rotation axis shift in the fault direction while keeping the stator coordinate center the same. The fault is implemented in the positive Y-axis direction by varying the shift

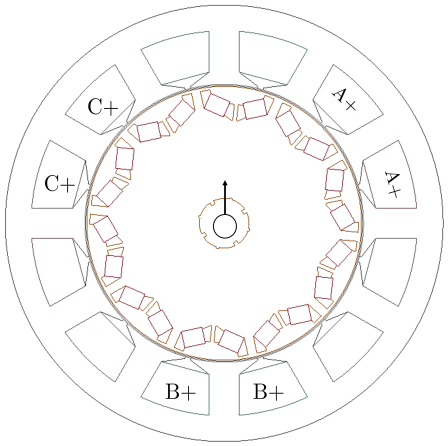

Figure 4.6: Shift direction of the static eccentricity fault.

value (ϵ), and three fault severity levels were considered as shown in Table 4.4. Since the eccentricity fault is inherently available due to tolerances in the manufacturing process, the machine is considered healthy if the severity level of static eccentricity is below than 10%.

Table 4.4: Severity levels of static eccentricity fault in PMSM [B].

Case	$\frac{\epsilon}{g}\%$
ECC1	40%
ECC2	60%
ECC3	80%

4.2.4 Partial Demagnetization

The demagnetization fault is applied in FEM by reducing the remnant flux density of the affected magnets. This could be uniform demagnetization in all magnets or partially in some magnets. The material in the upper corners (close to the air gap) of three selected magnets is replaced by the same material with reduced remnant flux density to $1T$. This is the most common scenario for demagnetization faults in PMSM. Fig. 4.7 shows the affected magnets. The fault severity is varied by changing the number of demagnetized magnets in the machine

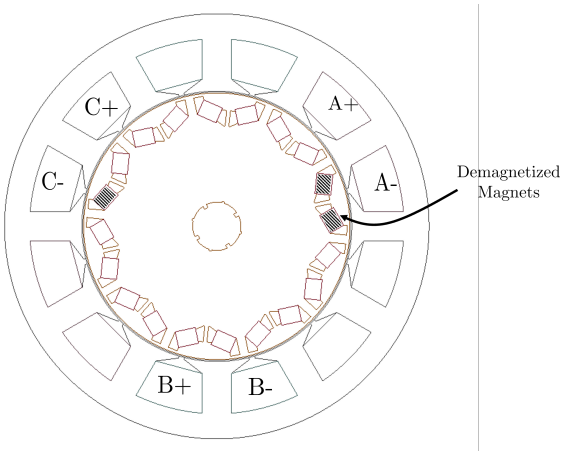

Figure 4.7: Demagnetized magnets in PMSM [B].

model as listed in Table 4.5.

Table 4.5: Severity levels of demagnetization fault in PMSM [B].

Case	Severity
Demag1	One Magnet
Demag2	Two Adjacent Magnets
Demag3	Three Nonadjacent Magnets

4.3 Experimental Setup

The test setup for this study consist of the PMSM [B] connected to the electrical dynamometer via a drive shaft flange. The PMSM is controlled in torque regulation mode and loaded with a dynamometer to run at particular states of load and speed for normal and faulty conditions. Pictures of the experimental test bench are shown in Fig. 4.8.

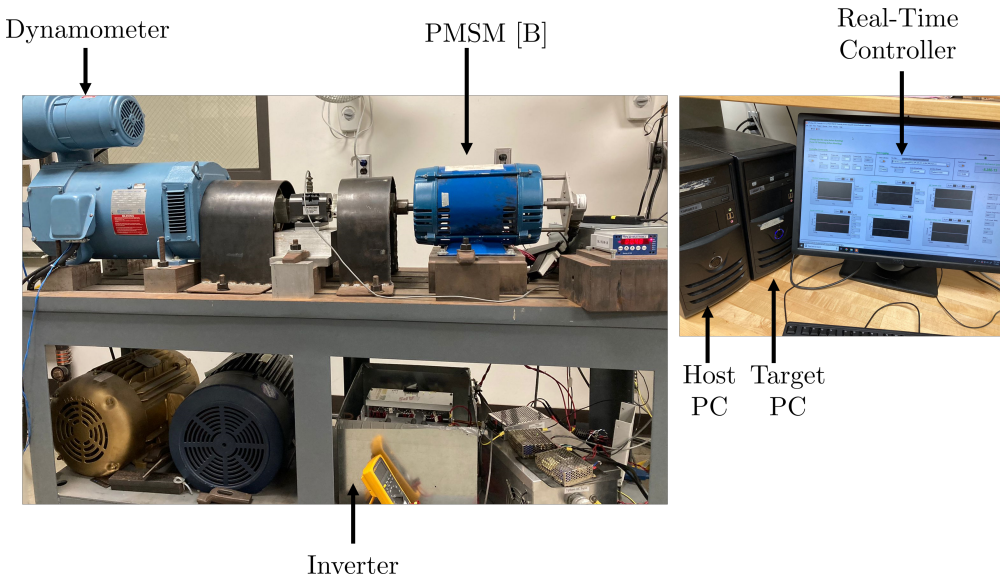

Figure 4.8: Experimental Test Bench.

Real Time LabVIEW is utilized to develop controllers for the studied PMSM in a host PC. The developed controllers are then deployed to a target PC, which includes an integrated 40 MHz Field Programmable Gate Array (FPGA). The host PC is used to set the controller commands and visualize the control performance. The target PC is dedicated only to do the control computations and sending/receiving the control signals to/from an inverter through

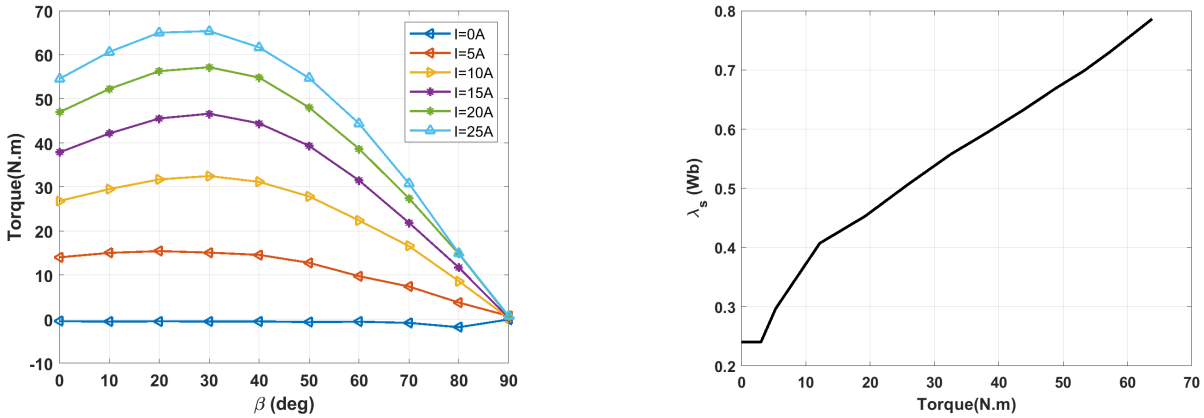

(a) For FOC drives.

(b) For DTC drives.

Figure 4.9: Experimental results of MTPA profile for driven PMSM [B].

FPGA-7852R series by National Instrument. This FPGA provides high resolution data sampling with 16-bits.

The FOC is implemented at 10 kHz where one sample is taken every one switching period. For DTC implementation, operating at a high sampling frequency is required to achieve adequate performance. Therefore, the DTC algorithm is divided into two parts. The first part is implemented at the FPGA level, since it requires fast control to keep the torque and flux within the hysteresis bands. The other part is implemented in the CPU of the target PC and it includes the references generation based on the stored MTPA profile as well as their estimation. The MTPA profile for FOC and DTC driven PMSM [B] is depicted in Fig. 4.9. As mentioned, the excitation angle (β) is found to be 30° to get the minimum current for a given torque in FOC case. The drive settings are listed in Table 4.6.

Table 4.6: Settings of the DTC Drive.

Controller Settings	**Symbol**	**Value**
Flux hysteresis band	$\Delta\lambda$	$0.025 \cdot \lvert\lambda_s^*\rvert$
Torque hysteresis band	ΔT	$0.045 \cdot t_e^*$
Sampling frequency	f_s	25 μs
Initial conditions	$(\lambda_{\alpha_0}, \lambda_{\beta_0})$	$(0.287, 0)$Wb

For TTSC fault experimental implementation, the winding of Phase A is split into separate coils with a different number of turns. The leads of each coil are carried out of the housing into the terminal box and can be shorted through a resistor. Additionally, the fault current circulating in the short path can be measured. In this work, the fault severities studied are: 15 turns with 0.5Ω, 15 turns with 0.25Ω, 30 turns with 0.5Ω, and 30 turns with 0.25Ω. The winding configuration of phase A for TTSC implementation is shown in Fig. 4.10.

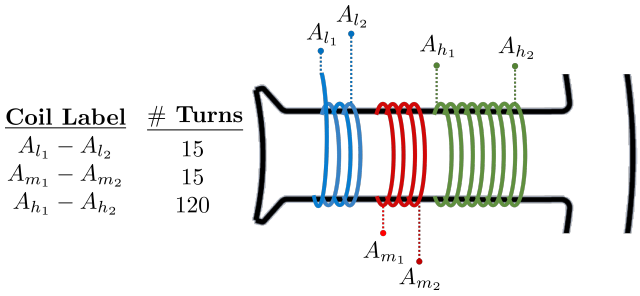

Figure 4.10: Winding Configuration of Phase A for TTSC Implementation.

Chapter 5

Comparative Fault Diagnosis Study in Inverter Driven PMSM

Inverter drives pose challenges in fault diagnosis. Therefore, fault diagnosis is critically important in inverter drives to assess the machine health and avoid any costly damage. In this chapter, fault diagnosis in FOC and DTC driven PMSM will be compared.

5.1 Motor Voltage Signature Analysis (MVSA)

Authors in [60] demonstrate the successful implementation of fault diagnosis based on the stator current spectrum in various industrial applications. This approach is considered non-invasive as it does not require any additional hardware. The current signal is available in the drive system using a current transducer. The commanded voltage signal could also be used for noninvasive diagnosis instead of using voltage sensor to measure the actual ones. For inverter driven machines, selecting the stator current or voltage signal is dependent on the bandwidth of the controller [1]. Faults would have similar or distinct changes to the frequency spectrum of the machine current or voltage signals. These changes could be utilized as features for fault classification and severity estimation.

Several signal processing techniques are available to obtain the frequency spectrum of the machine current or voltage signals [61]. The signal spectrum is obtained at a steady state

using Fast Fourier Transform (FFT), or at nonstationary conditions using time-frequency analysis methods like Short Time Fourier transform (STFT). FFT has been applied successfully to the machine voltage in [4] to detect and separate between faults. The first fifteen harmonics in the voltage spectrum are used as features for the classification algorithms. This section is to examine the accuracy of the machine voltage signature analysis (MVSA) with FFT in fault diagnosis for both control drives. Supervised classification algorithms are utilized to detect the fault type and severity.

5.1.1 Analysis in FOC driven PMSM

The frequency spectrum of the commanded phase A voltage is obtained using FFT for different machine health conditions. The fundamental, 5^{th}, and 7^{th} harmonics are used here to show the fault effect on the voltage spectrum at different severity levels.

The stator voltage spectrum is shown in Fig. 5.1 for healthy and faulty machine under different severity levels of TTSC fault.

It could be observed that the magnitude of the fundamental, 5^{th}, and 7^{th} harmonics in the voltage spectrum is reduced as the TTSC fault becomes more severe. The magnitude changes in the spectrum are significant enough to distinguish between the healthy case and TTSC fault. Besides that, one can notice the increase in the 2^{nd} harmonic when TTSC is present. The first ten harmonics will be used as features for diagnosis as described in the following section.

The stator voltage spectrum is shown in Fig. 5.2 for healthy and faulty machine under different severity levels of HRC fault.

It could be observed that the magnitude of the fundamental harmonic in the voltage spectrum is increasing significantly with the severity HRC fault. On the other hand, the magnitude of

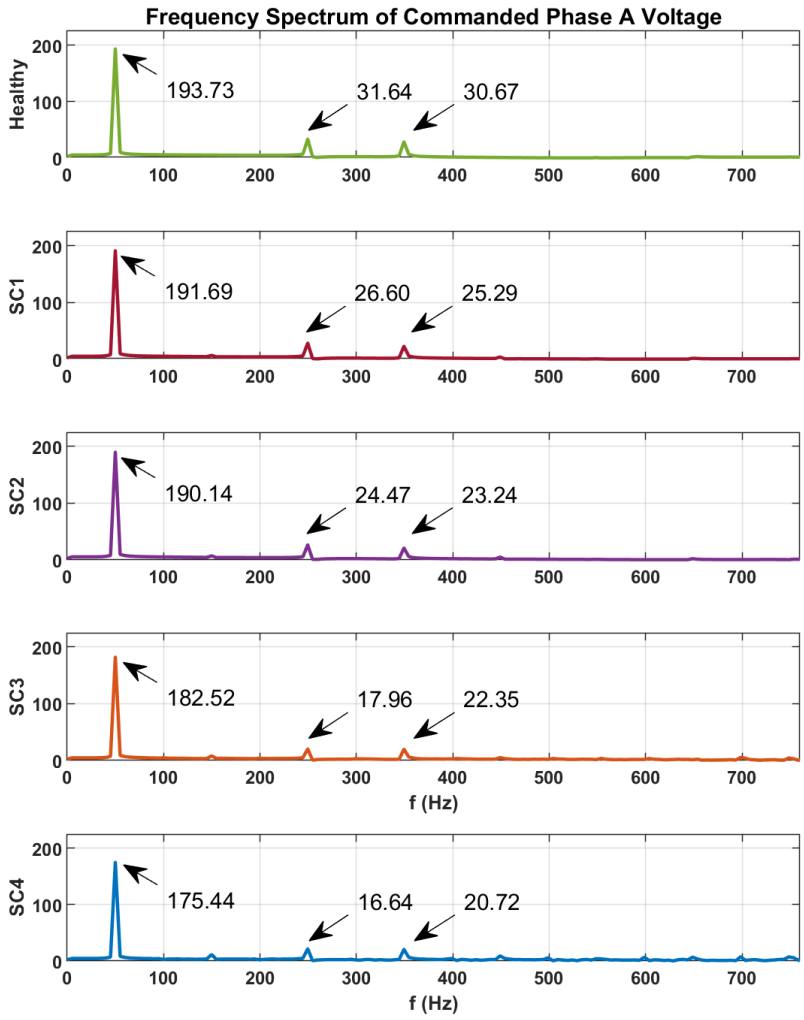

Figure 5.1: Stator voltage spectrum for healthy and faulty machine under TTSC fault in FOC drive at 600 rpm and 10A.

the 5^{th}, and 7^{th} harmonics is reduced. However, these magnitude changes may be insignificant for distinguishing between the healthy case and HRC fault. It is worth noting that the considered severity levels of HRC are relatively low and may justify the insignificant changes in the magnitude of the 5^{th}, and 7^{th} harmonics.

The stator voltage spectrum is shown in Fig. 5.3 for healthy and faulty machine under different severity levels of eccentricity fault.

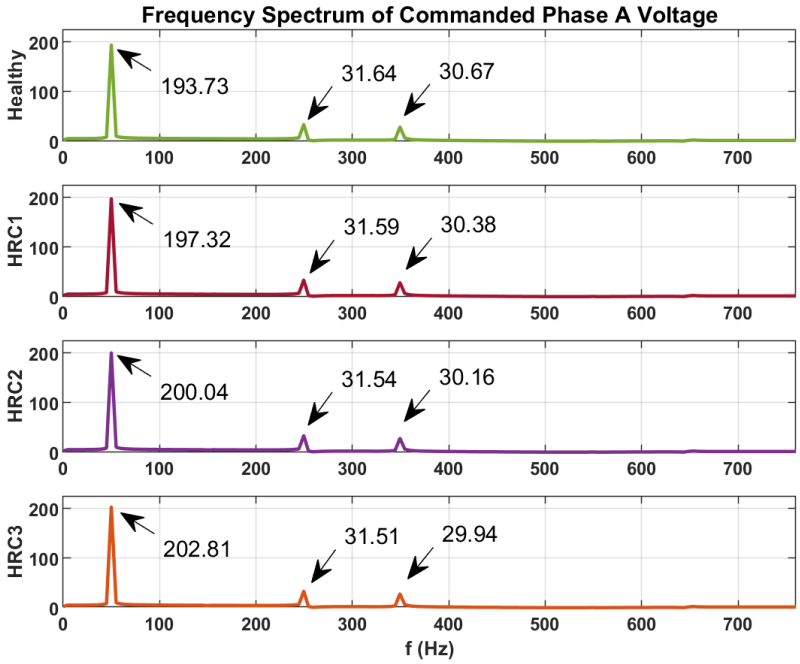

Figure 5.2: Stator voltage spectrum for healthy and faulty machine under HRC fault in FOC drive at 600 rpm and 10A.

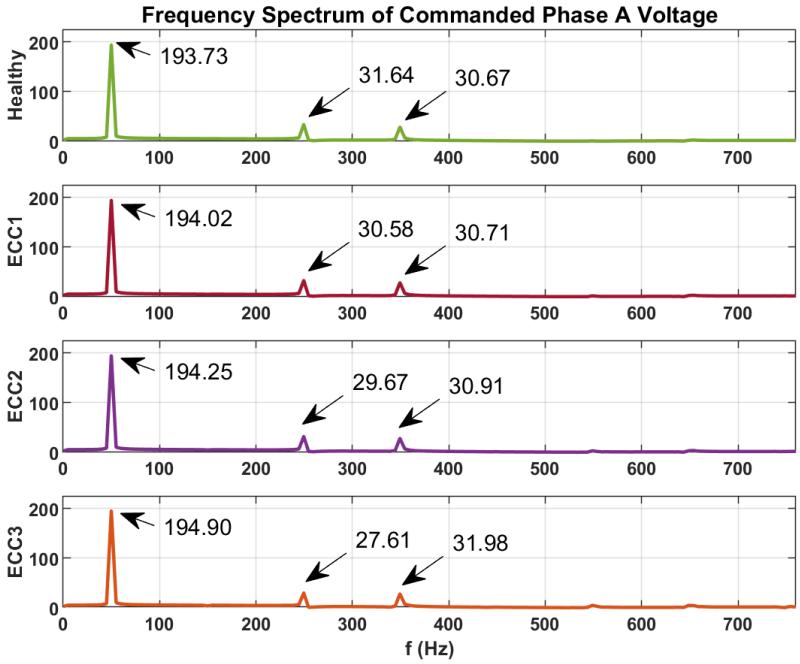

Figure 5.3: Stator voltage spectrum for healthy and faulty machine under eccentricity fault in FOC drive at 600 rpm and 10A.

It can be observed that the magnitude of the fundamental and 7^{th} harmonics in the voltage spectrum is increasing with the severity of the eccentricity fault, while the magnitude of the 5^{th} harmonic is reduced significantly. These magnitude changes are significant enough to distinguish between the healthy case and eccentricity fault. Besides that, these magnitude changes due to eccentricity fault are different from those for TTSC and HRC faults. This will benefit fault classification, discussed later.

The stator voltage spectrum is shown in Fig. 5.4 for healthy and faulty machine under different severity levels of demagnetization fault. As shown, the magnitude of the fundamental

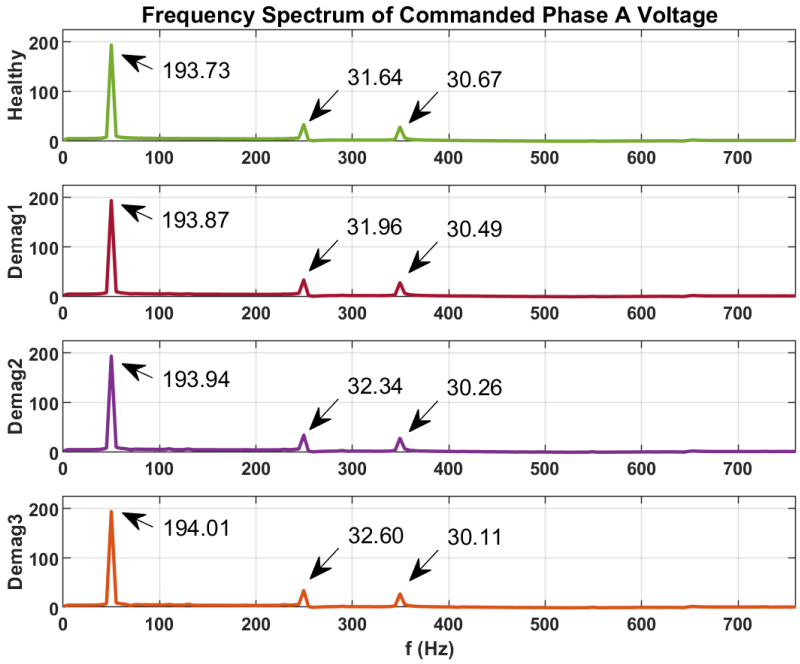

Figure 5.4: Stator voltage spectrum for healthy and faulty machine under demagnetization fault in FOC drive at 600 rpm and 10A.

and 5^{th} harmonics in the voltage spectrum is increasing with severity of the demagnetization fault, while the magnitude of the 7^{th} harmonic is reduced. These magnitude changes can be used to distinguish between the healthy case and demagnetization fault. It is worth to mention that the considered severity levels of demagnetization fault is full demagnetization

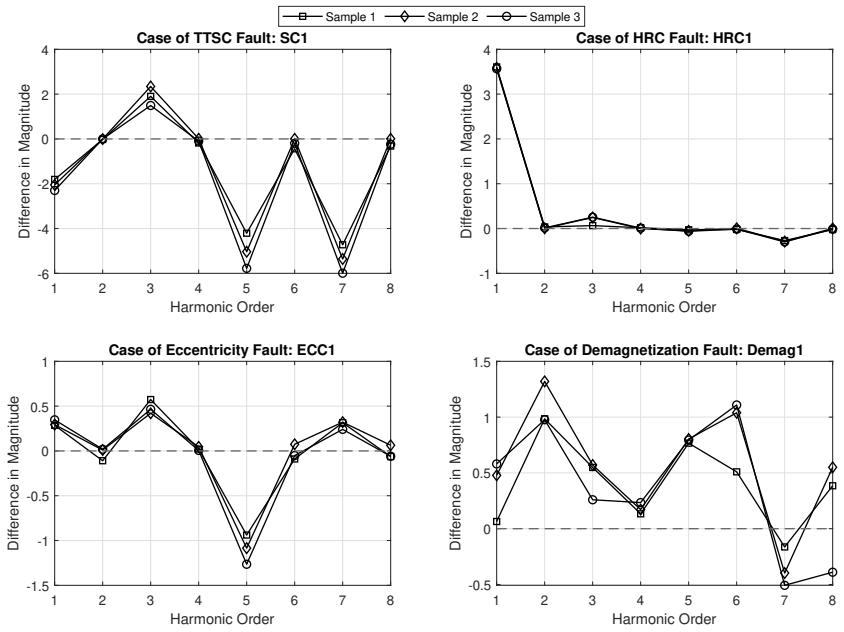

Figure 5.5: Feature Trends of the MVSA for the Lowest Considered Severity Level of Each Fault Across Different Samples in case of FOC driven PMSM.

of one to three magnets. Besides that, the trend in magnitude change of the fundamental harmonic due to demagnetization fault is similar to the trend due to HRC and eccentricity faults, while it is the opposite in case of the 5^{th} harmonic. This would help the classifier in discriminating between these three faults.

Fig. 5.5 provides evidence of the consistent variation in feature trends observed for the lowest considered severity level of each fault across different samples: 550, 600, and 650 rpm.

5.1.2 Analysis in DTC driven PMSM

The frequency spectrum of the commanded phase A voltage is obtained using FFT for different machine health conditions under DTC drive. The fundamental, 5^{th}, and 7^{th} harmonics are also used here to show the fault effect on the voltage spectrum at different severity levels.

The stator voltage spectrum is shown in Fig. 5.6 for healthy and faulty machine under

different severity levels of TTSC fault when the machine is driven by DTC. It is observed

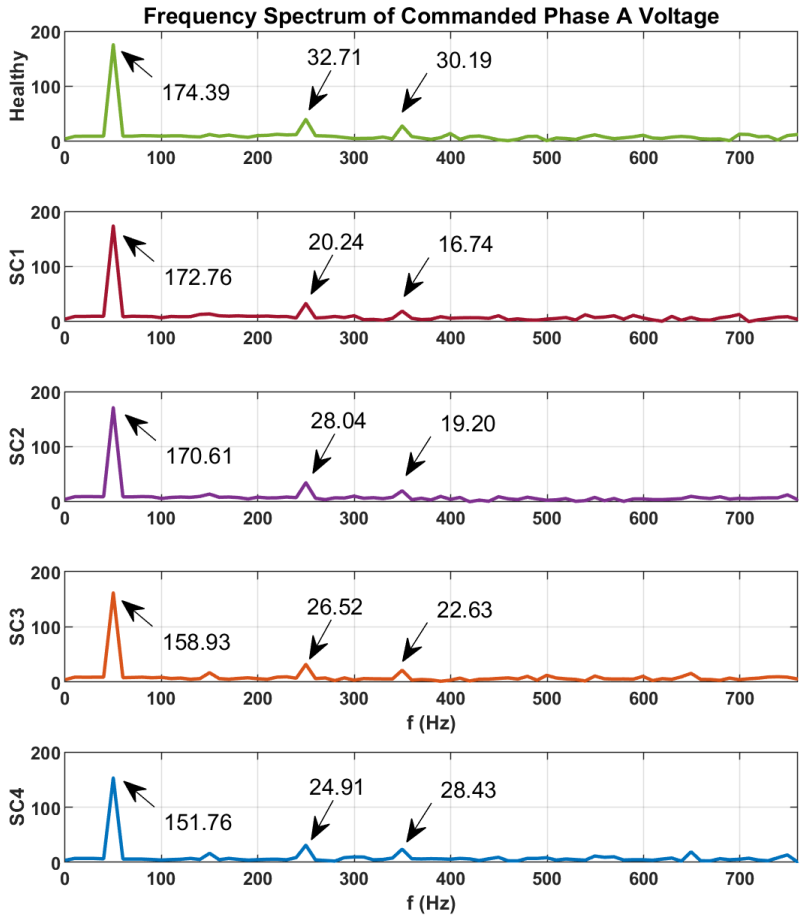

Figure 5.6: Stator voltage spectrum for healthy and faulty machine under TTSC fault in DTC drive at 600 rpm and 20Nm.

that the magnitude of the fundamental, 5^{th}, and 7^{th} harmonics in the voltage spectrum is reduced when TTSC fault is present. This observation is similar to the fault effect in the FOC drive. However, it can be noticed that the magnitude of the 7^{th} harmonic is increased from SC1 to SC2 and from SC3 to SC4, where the number of shorted turns is the same but different fault resistance is used. This is the same case for the 5^{th} harmonic from SC1 to SC2 but not from SC3 to SC4. Additionally, the magnitude of the 7^{th} harmonic is increased from

SC1 to SC3 and from SC2 to SC4, where the number of shorted turns is different but with the same fault resistance. This is the same case for the 5^{th} harmonic from SC1 to SC3 but it is not from SC2 to SC4. If these harmonics are used as features for diagnosis approach, the classifier will be overwhelmed since the changes in the used harmonics due to different TTSC severity levels are not consistent with increase in the fault severity.

The stator voltage spectrum is shown in Fig. 5.7 for healthy and faulty machine under different severity levels of HRC fault when the machine is driven by DTC. It is observed that

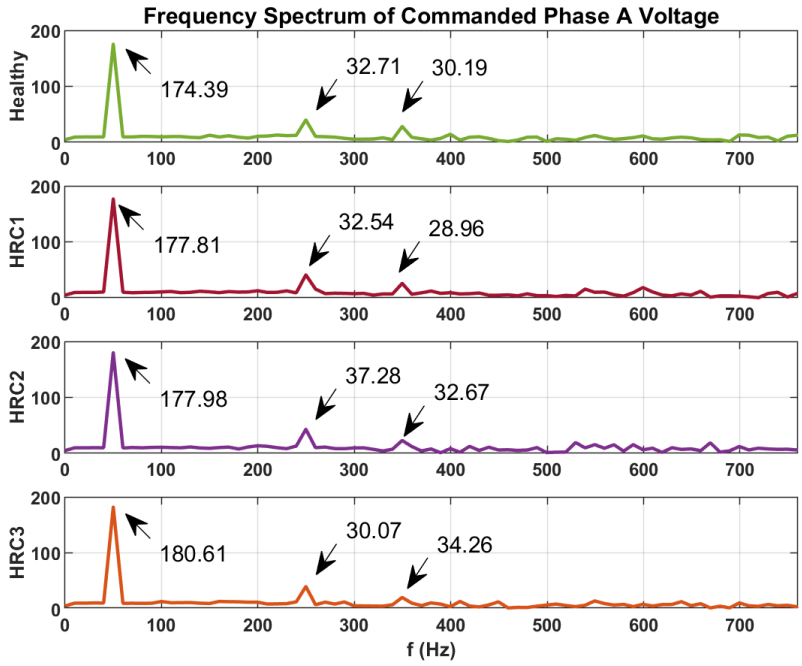

Figure 5.7: Stator voltage spectrum for healthy and faulty machine under HRC fault in DTC drive at 600 rpm and 20Nm.

the magnitude of the fundamental harmonic in the voltage spectrum is increasing significantly with severity of the HRC fault. On the other hand, the magnitude of the 5^{th} has inconsistent change; it does not change significantly at HRC1 but it increases at HRC2 and then decreases at HRC3. Similarly, the magnitude of the 7^{th} decreases at HRC1 but then starts increasing at HRC2 and HRC3. Once again, these inconsistent changes in the voltage spectrum due to

different HRC severity levels will result in high false classification results.

The stator voltage spectrum is shown in Fig. 5.8 for healthy and faulty machine under different severity levels of eccentricity fault when the machine is driven by DTC. It is observed

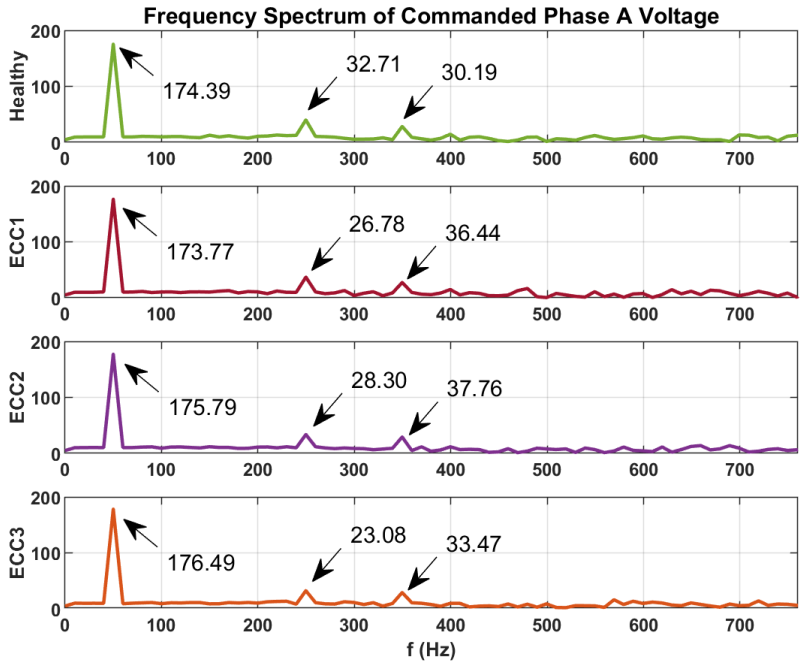

Figure 5.8: Stator voltage spectrum for healthy and faulty machine under eccentricity fault in DTC drive at 600 rpm and 20Nm.

that the magnitude of the fundamental harmonic in the voltage spectrum has inconsistent changes due to different severity levels of eccentricity fault. It is reducing at ECC1 and then increasing at ECC2 and ECC3. Similarly, the magnitude of the 5^{th} harmonic reduces at all eccentricity severity levels. However, it decreases from healthy case to ECC1, increases from ECC1 to ECC2, and then decreases from ECC2 to ECC3. An inconsistent pattern is also noticed with the 7^{th} harmonic. These irregular changes in the spectrum will result in difficulty performing fault detection and separation in DTC drives.

The stator voltage spectrum is shown in Fig. 5.9 for healthy and faulty machine under different severity levels of demagnetization fault when the machine is driven by DTC. It

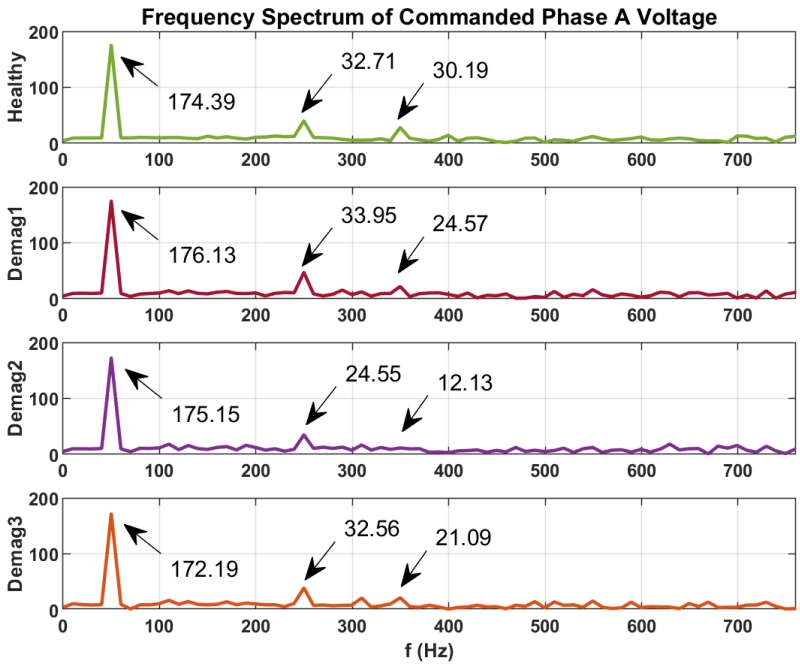

Figure 5.9: Stator voltage spectrum for healthy and faulty machine under demagnetization fault in DTC drive at 600 rpm and 20Nm.

is noticed that the magnitude of the fundamental harmonic in the voltage spectrum has inconsistent changes due to different severity levels of demagnetization fault. It is increasing at Demag1 and Demag2 but then reducing at Demag3. Similarly, the magnitude of the 5^{th} and 7^{th} harmonics have inconsistent changes with increasing the demagnetization fault severity.

Fig. 5.10 provides evidence of the inconsistent variation in feature trends observed for the lowest considered severity level of each fault across different samples: 550, 600, and 650 rpm. In comparison with applying the MVSA approach in FOC drives, the changes in the voltage spectrum in DTC drives will not benefit the classifier in identifying fault, discriminating between them, and estimating their severity.

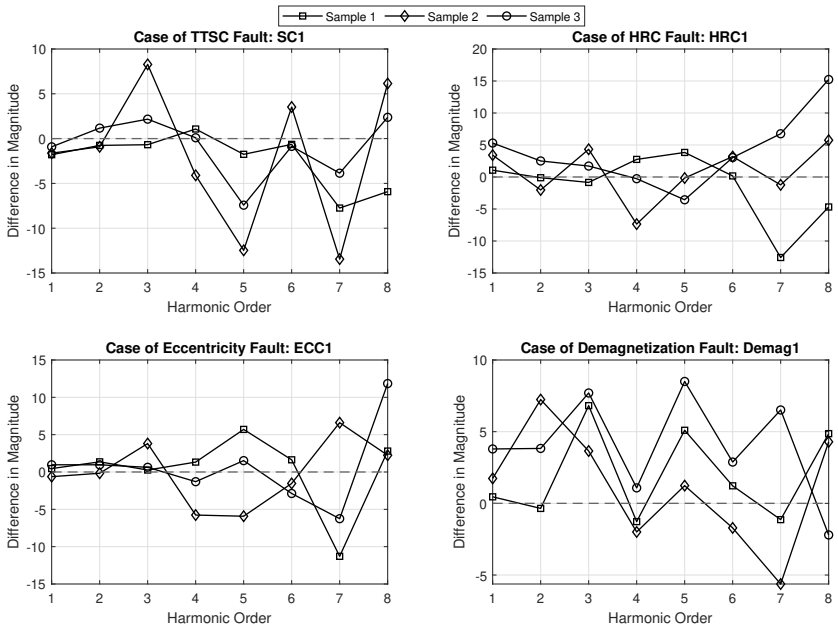

Figure 5.10: Feature Trends of the MVSA for the Lowest Considered Severity Level of Each Fault Across Different Samples in case of DTC driven PMSM.

5.2 Supervised Classification

Supervised machine learning is a training process for the predictive model through known input data [62]. This data-driven model is then used to predict a class for an unknown sample. In this work, three classification approaches are used: (i) Linear Discriminant Analysis (LDA), (ii) k-Nearest Neighbor (k-NN), and (iii) Support Vector Machine (SVM).

LDA assumes a normal distribution for the training samples with a fixed covariance matrix that does not depend on classes. Given a two-indicator case, the decision boundary segregating classes are linear using LDA. However, if the normality assumption of data distribution does not hold, the discriminant routine is extremely biased [63]. Here, the sample space is split into (K) classes, where each class contains a number of samples corresponding to the same class. Each class is associated with weighting factors that are used to determine the discriminant function for that class. The discriminant function (C_k) for k^{th} class is

calculated as following:

$$C_k(X) = \alpha_{1k}x_1 + \alpha_{2k}x_2 + ... + \alpha_{Nk}x_N \tag{5.1}$$

where $X = [x_1, x_2, ..., x_N]$ is the N dimensional observation vector and $[\alpha_{1k}, \alpha_{2k}, ..., \alpha_{Nk}]$ is the weighting factors matrix for the k^{th} group. Each sample will be assigned to a particular class if its linear discriminant function is greater than other linear discernment functions. For example, a sample X_i belongs to a class j if,

$$C_j(X_i) \geq C_k(X_i), \quad \forall j \neq k \tag{5.2}$$

To avoid dependency on normal distribution parameters, k-NN and SVM are applied, but their classification accuracy depends proportionally on the number of training samples [64]. The k-NN approach assigns a class for the unknown sample based on the majority voting among the nearest neighbors. Its accuracy relies on the number of selected neighbors and the distance metric used to find the neighbors. For this work, the nearest four neighbors and Euclidean distance show the maximum classification accuracy using k-NN. The Euclidean distance is given by:

$$D_{XY} = \sqrt{\sum_{i=1}^{n}(x_{mi} - y_{pi})^2} \tag{5.3}$$

where $X = [x_{m1}, ..., x_{mn}]$ is the tested samples vector, $Y = [y_{p1}, ..., y_{pn}]$ is the training samples vector, $m = 1, ..., j$ is the number of tested samples and $p = 1, ..., l$ is the number of testing samples.

SVM is another supervised machine learning technique known for its robustness against noise and data bias [65]. The objective of the SVM classifier is to obtain the optimum

hyperplane that maximizes the discrimination of two different sets of data using support vectors only. The furthest samples near the discrimination margin are called support vectors. An unknown sample is classified by evaluating the orthogonal distance from this sample to the optimum hyperplane generated by SVM. The training phase of SVM consists of a minimization problem of the weighting vector $\zeta(X)$ such that each sample will meet the following objective:

$$\zeta(X) = w^T X + \xi_o \geq 0 \tag{5.4}$$

where w is weighting vector and ξ_o is a threshold value for classifier modeling. SVM utilizes kernel functions when the data is not linearly separable in its dimensional space. Therefore, SVM fits the data into other dimensional spaces with higher scales where the data becomes linearly divisible. SVM classifier could also be extended for multi-class classification problems by considering one class against another in the classification problem or considering one class against all other classes. In this study, the former approach is applied to study different fault classes.

To evaluate the accuracy of the aforementioned classifiers, a leave-one-out approach is used by excluding one sample from the training samples set and use it as unknown sample to be classified. The process is iterated for all samples in every class. Afterward, the classifier accuracy is evaluated using the following:

$$\Lambda = (\frac{N_{labeled}}{N_{total}}) \times 100\% \tag{5.5}$$

where Λ is the classifier accuracy, $N_{labeled}$ is the number of correctly labeled samples, and

N_{total} is the total number of samples in the training pool.

5.3 Diagnosis Approach

Fast Fourier transformation (FFT) technique was applied in MATLAB to get the frequency spectrum of commanded phase A voltage, and extract the magnitude of the first eight harmonics. The inclusion of additional harmonics enables fault detection, categorization and estimation for TTSC, HRC, static eccentricity and partial demagnetization without additional sensors. If the ultimate goal is reliable fault separation, multiple features should be adopted. The fault detection method is evaluated for inverter-fed PMSM drives under FOC and DTC controllers, taking the advantage of inherent availability of commanded voltage signal in these control schemes.

Here, a comparison between supervised classification approaches: LDA, k-NN, and SVM in terms of the ability to identify the faulty cases, distinguish between the considered faults, and estimate their severity is provided. Fig. 5.11 shows the flowchart of the fault detection, separation, and severity estimation algorithm. The harmonics are used as features for the classification stage. To generate samples in FEA for healthy and faults cases, the speed is varied from 250 rpm to 750 rpm in steps of 50 rpm at different operating points. The current loading is set to be 10 A at $\beta = 30^{\circ}$ for FOC, while the torque loading for DTC is set at 20 Nm at 0.52 Wb to get the MTPA operation for both controllers. In this numerical setup, 140 observations are generated (10 for each health state): healthy, three severity levels of eccentricity, three severity levels of HRC, four severity levels of TTSC, and three severity levels of demagnetization.

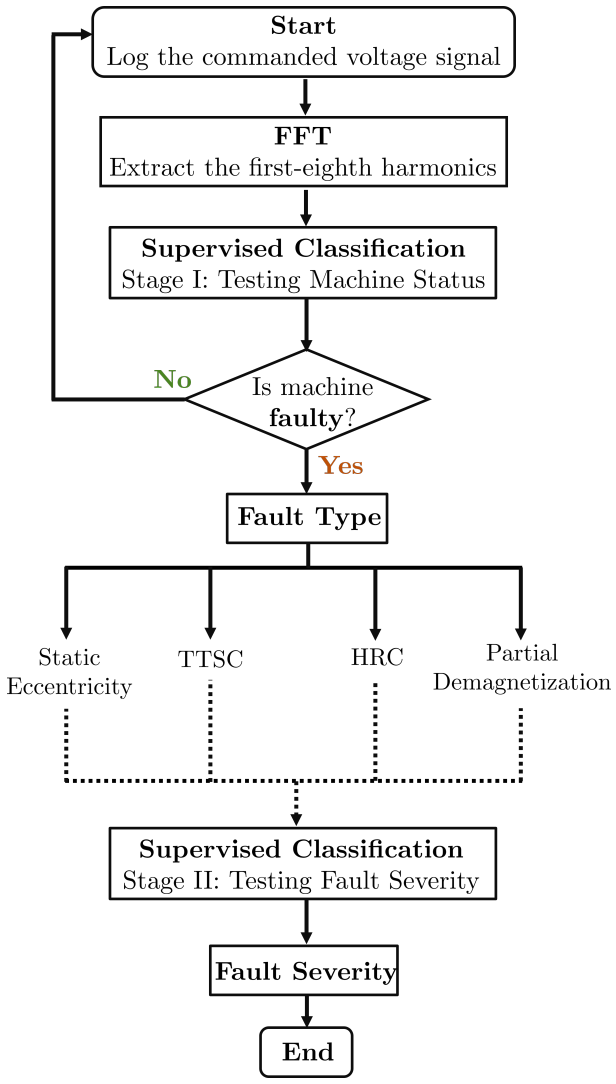

Figure 5.11: Flowchart of fault detection, separation, and severity estimation algorithm.

5.4 Comparative Results

The accuracy of the fault detection and classification is shown in Table 5.1. It is assumed that if the classifier is able to detect the faulty operation of the machine and indicate the fault type at its lower severity level, then it will be able to perform the diagnosis at higher severity levels. Therefore, only samples of the faulty cases at the lowest severity are considered in the training pool to perform fault detection and separation.

It is clear that the considered classifiers are capable of fault detection and separation using

Table 5.1: Detection accuracy using MVSA approach for FOC and DTC driven PMSM [B].

	FOC			**DTC**		
Case	LDA	k-NN	SVM	LDA	k-NN	SVM
Healthy	100%	100%	97.5%	10%	10%	67.5%
SC1	90%	100%	100%	80%	80%	80%
HRC1	100%	100%	90%	40%	80%	85%
Ecc1	100%	100%	100%	60%	90%	77.5%
Demag1	80%	70%	87.5%	70%	40%	80%
Overall	94%	94%	95%	52%	60%	78%

the MVSA approach in FOC driven PMSM while their overall performance is significantly degraded in case of DTC driven PMSM. Moreover, it can be observed that all classifiers achieve lower accuracy in capturing the healthy state for DTC drives in comparison with case of FOC drives. This leads to high false indication rate in DTC and unnecessary system shutdowns. Besides that, SVM classifier shows the highest detection and separation accuracy in both drives. Therefore, it is proved that relying on the MVSA approach for fault diagnosis in DTC drives would result in poor performance and significant amount of false alarms. Fig. 5.12 provides the confusion matrix of LDA classifier for fault diagnosis to show the false alarms and incorrect classification in FOC and DTC drives. The accuracy of the fault severity estimation using the LDA and SVM classifiers is shown in Table 5.2. Once the faulty operation is indicated and fault type is detected from the first stage of the supervised classification, then the second classification stage will be dedicated for severity estimation of the detected fault. Therefore, samples of the detected fault at each severity level are considered in the training pool to perform fault severity estimation. It can be observed from Table 5.2 the degradation in the performance of LDA and SVM classifiers for the fault severity estimation when DTC is applied in comparison with FOC. This is related to the earlier mentioned fact of inconsistent changes in the voltage spectrum due to different

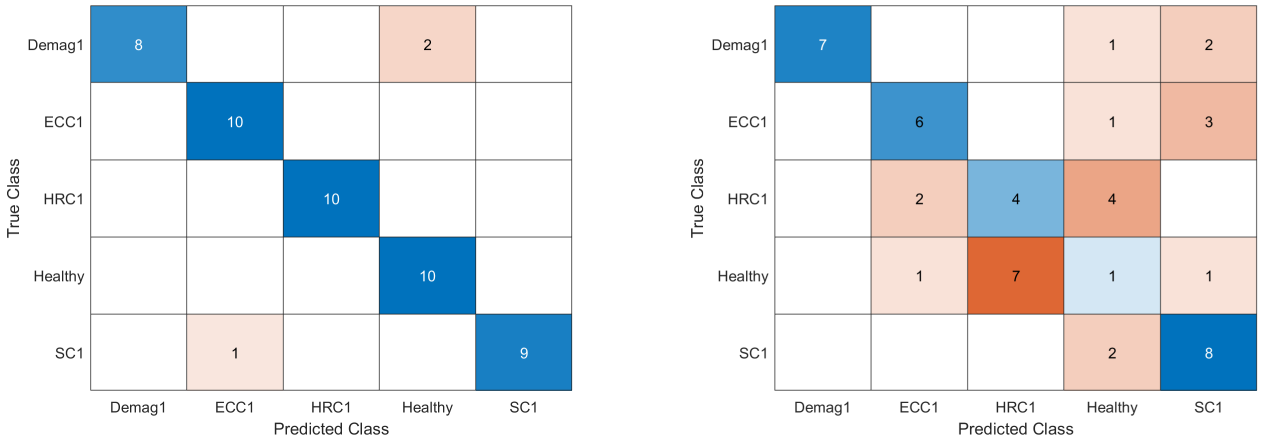

(a) For FOC drives.

(b) For DTC drives.

Figure 5.12: Confusion matrix of LDA classifier for fault diagnosis in FOC and DTC driven PMSM [B].

Table 5.2: The accuracy of fault severity estimation using MVSA approach for FOC and DTC driven PMSM [B].

	FOC		**DTC**	
Fault Type	LDA	SVM	LDA	SVM
TTSC	**85%**	**97.5%**	**42.5%**	**64.167%**
SC1	100%	100%	50%	63.333%
SC2	100%	100%	40%	66.667%
SC3	80%	93.333%	30%	66.667%
SC4	60%	96.667%	50%	60%
HRC	**96.667%**	**86.667%**	**30%**	**38.333%**
HRC1	100%	100%	30%	35%
HRC2	90%	80%	20%	30%
HRC3	100%	100%	40%	50%
Eccentricity	**100%**	**100%**	**46.667%**	**71.667%**
ECC1	100%	100%	60%	75%
ECC2	100%	100%	40%	65%
ECC3	100%	100%	40%	75%
Demagnetization	**86.667%**	**71.667%**	**46.667%**	**56.667%**
Demag1	100%	100%	80%	75%
Demag2	90%	50%	20%	55%
Demag3	70%	60%	40%	40%

severity levels of each fault in case of DTC drives. Therefore, for reliable fault diagnosis in DTC driven PMSMS further improvement is required.

To determine if the lack of integration between the separate stages for fault detection and severity estimation led to suboptimal performance, feasibility of a single stage classifier is evaluated. This classifier is designed to concurrently predict both fault types and severity levels. Table 5.3 presents the accuracy of LDA and SVM classifier in identifying the machine health state and severity levels.

Table 5.3: Fault detection and severity estimation using MVSA approach for FOC and DTC driven PMSM [B] in One Stage.

	FOC		**DTC**	
Machine Condition	LDA	SVM	LDA	SVM
Healthy	40.0%	94.6%	0.00%	57.7%
SC1	40.0%	96.9%	10.0%	63.8%
SC2	50.0%	99.2%	50.0%	80.0%
SC3	30.0%	98.5%	20.0%	87.7%
SC4	50.0%	99.2%	40.0%	73.1%
HRC1	0.00%	91.5%	10.0%	61.5%
HRC2	0.00%	93.1%	0.00%	61.5%
HRC3	10.0%	94.6%	30.0%	71.5%
ECC1	0.00%	95.4%	0.00%	60.0%
ECC2	20.0%	99.2%	40.0%	75.4%
ECC3	80.0%	96.9%	20.0%	76.2%
Demag1	20.0%	88.5%	30.0%	68.5%
Demag2	10.0%	80.8%	40.0%	73.8%
Demag3	0.00%	84.6%	40.0%	76.2%
Overall	25.0%	93.8%	23.6%	70.5%

The degradation of LDA performance can be observed when fault detection and severity estimation are combined in a single stage. In contrast, the SVM classifier demonstrates better performance in both the FOC and DTC drives for fault detection and severity estimation. Nevertheless, the accuracy of the SVM classifier experiences a noticeable decline in the case of DTC driven PMSM in comparison with its performance in the FOC drive. Since the performance of SVM classifier in DTC drive is not satisfactory, there is a potential to

improve its effectiveness by means of investigating alternative kernel functions.

Kernel functions in SVM model are utilized to transform the feature vector into higher dimensional space where the feature vector becomes linearly separable. Radial Basis Function (RBF) kernel and polynomial kernel are two examples of kernel functions used in SVM classifier. The RBF kernel is known as the Gaussian kernel as it uses the Gaussian distribution function as given by (5.6) [66].

$$Z_{RBF}(x_i, x_j) = e^{-\gamma||x_i - x_j||^2} \tag{5.6}$$

Here, $Z_{RBF}(x_i, x_j)$ measures the similarity between x_i and x_j. The parameter γ controls the influence of each data pair on the decision boundary. As γ becomes larger, limited impact range is expected. The initial selection of this parameter is given by (5.7) [67].

$$\gamma = \frac{1}{N \cdot \sigma} \tag{5.7}$$

Here, N is the number of features used for classification and σ is the variance of the data. The initial value for γ is set to 0.125, and additional values are chosen for a grid search to identify the optimal value that maximizes accuracy. Table 5.4 presents the classification accuracy of SVM classifier in DTC drive using the RBF kernel function. It is observed that the utilization of the SVM classifier with the RBF kernel function does not exhibit a substantial enhancement in the detection accuracy.

The other kernel function used for SVM modeling is the polynomial. The mathematical

Table 5.4: Fault detection and severity estimation using MVSA approach for DTC driven PMSM [B] in One Stage of SVM classifier with RBF Kernel.

	SVM with RBF Kernel			
Machine Status	$\gamma = 0.01$	$\gamma = 0.125$	$\gamma = 0.25$	$\gamma = 1$
Healthy	11.5%	31.5%	23.8%	12.3%
SC1	13.1%	36.9%	36.15%	10.0%
SC2	20.0%	75.4%	69.2%	37.7%
SC3	18.5%	67.7%	64.6%	32.3%
SC4	26.9%	74.6%	73.8%	36.9%
HRC1	16.9%	46.2%	48.5%	20.0%
HRC2	16.9%	40.0%	37.7%	12.3%
HRC3	16.9%	47.7%	42.3%	28.5%
ECC1	13.1%	32.3%	33.8%	10.8%
ECC2	15.4%	39.3%	34.6%	21.5%
ECC3	10.0%	40.0%	36.9%	6.90%
Demag1	15.4%	61.5%	58.5%	20.8%
Demag2	49.2%	66.1%	66.9%	55.4%
Demag3	46.9%	66.1%	70.0%	56.2%
Overall Accuracy	20.8%	51.8%	49.8%	25.8%

expression of the polynomial kernel is given in (5.8).

$$Z_{poly}(x_i, x_j) = (1 + x_i \cdot x_j)^q \tag{5.8}$$

Here, Z_{poly} measures the similarity between x_i and x_j using a polynomial function of q degree. Table 5.5 presents the classification accuracy of SVM classifier in DTC drive using the polynomial kernel function with different orders. In conclusion, the detection accuracy obtained by using the polynomial kernel function in the SVM classifier is comparable to that achieved by the linear kernel. However, further investigation is needed to explore different feature sets that have the potential to improve the overall performance of the SVM classifier in DTC driven PMSM.

Table 5.5: Fault detection and severity estimation using MVSA approach for DTC driven PMSM [B] in One Stage of SVM classifier with Polynomial Kernel.

	SVM with Polynomial Kernel			
Machine Status	$q = 2$	$q = 3$	$q = 4$	$q = 5$
Healthy	43.1%	32.3%	36.2%	30.0%
SC1	53.1%	56.2%	50.8%	61.5%
SC2	73.1%	65.4%	63.8%	60.0%
SC3	76.9%	84.6%	80.8%	81.5%
SC4	70.0%	73.1%	64.6%	56.9%
HRC1	58.5%	58.5%	51.5%	53.1%
HRC2	50.0%	51.5%	39.2%	46.2%
HRC3	59.2%	62.3%	58.5%	63.1%
ECC1	51.5%	43.8%	49.2%	40.0%
ECC2	56.9%	56.2%	61.5%	60.0%
ECC3	58.4%	60.0%	63.8%	62.3%
Demag1	72.3%	70.0%	69.2%	67.7%
Demag2	80.0%	63.8%	56.9%	47.7%
Demag3	71.5%	68.5%	50.8%	55.4%
Overall Accuracy	62.5%	60.4%	56.9%	56.1%

Chapter 6

Condition Monitoring of DTC Driven PMSM

Torque and flux ripple are considered the main effects of the faults on the drive performance. These metrics are expected to increase under faulty conditions. However, these metrics may have different changes in DTC under different faulty conditions since the switching frequency is variable in this drive. DTC changes the switching frequency in order to maintain the torque and flux waveforms within prespecified hysteresis bands. Therefore, studying the variations in both torque and flux ripple and switching frequency is needed to understand the principle behind these changes. The torque and flux ripple ($t_{ripple}, \lambda_{ripple}$) are computed using (6.1).

$$S_{ripple} = \sqrt{\frac{1}{N}\sum_{n=1}^{N}(S(n) - S^*)^2} \tag{6.1}$$

Where (S) is the considered torque or flux signal, and (N) is the total number of samples within the considered cycle for ripple evaluation.

The inverter switching frequency in DTC is mainly determined by the bandwidth of the torque and flux hysteresis comparators. As less ripple is desired in the torque and flux responses, higher switching frequency is required to maintain these signals within the hysteresis bands and thereby achieving a nearly sinusoidal current waveform, similar to FOC. The average switching frequency (f_s), described in (6.2), is used here to predict the average

switching frequency.

$$f_s = \frac{n_s}{\tau} \tag{6.2}$$

Where (n_s) is number of transitions between voltage sectors in one fundamental period (τ). Also, it could be predicted empirically as suggested in [68].

6.1 Faulty Drive Operation

As shown in Table 6.1, both the torque and flux ripple increase with fault severity. It can be observed that the torque ripple of the machine has been significantly increased under TTSC fault especially when the machine is highly loaded or running at higher speeds. This would result in undesirable increase of the NVH levels of the machine. The sampling frequency is an important consideration for controller design to ensure that the ripple remains within the hysteresis band under both healthy and faulty conditions.

Table 6.1: The effect of TTSC fault on the torque and flux ripple of PMSM [B].

	DTC Operating Point							
	20N.m/350rpm		**20N.m/700rpm**		**40N.m/350rpm**		**40N.m/700rpm**	
Case	t_{ripple}	λ_{ripple}	t_{ripple}	λ_{ripple}	t_{ripple}	λ_{ripple}	t_{ripple}	λ_{ripple}
Healthy	1.33	0.0174	1.42	0.0173	2.39	0.0171	2.74	0.0250
SC1	1.60	0.0179	1.97	0.0188	2.59	0.0162	3.29	0.0201
SC2	1.78	0.0205	2.46	0.0222	2.77	0.0180	3.64	0.0184
SC3	2.49	0.0322	3.51	0.0414	3.50	0.0258	5.70	0.0292
SC4	2.97	0.0383	3.94	0.0563	4.24	0.0308	6.85	0.0379

It is also noted that DTC reacts to the presence of the TTSC effect by increasing the switching frequency as shown in Fig. 6.1. This is a result of hitting the flux and torque bands under TTSC fault more frequently than the healthy case due to the increase in the torque and flux ripple [21].

As shown in Table 6.2, HRC fault has insignificant effect on the torque and flux ripple

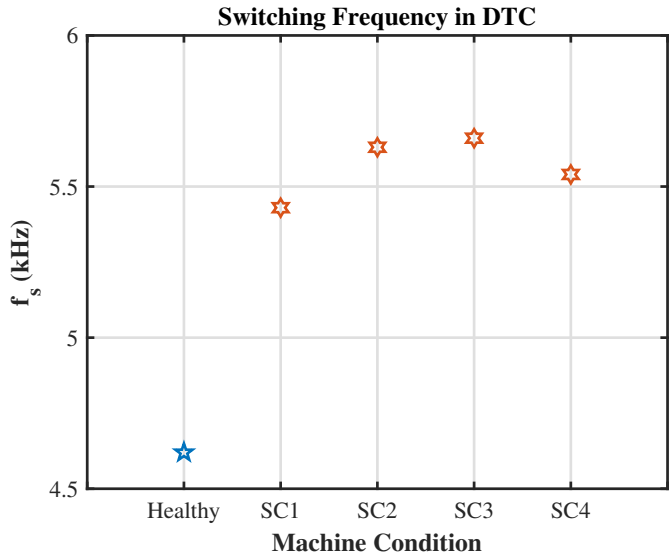

Figure 6.1: Switching frequency in DTC under healthy case and different TTSC fault severities.

Table 6.2: The effect of HRC fault on the torque and flux ripple of PMSM [B].

	DTC Operating Point							
	20N.m/350rpm		**20N.m/700rpm**		**40N.m/350rpm**		**40N.m/700rpm**	
Case	t_{ripple}	λ_{ripple}	t_{ripple}	λ_{ripple}	t_{ripple}	λ_{ripple}	t_{ripple}	λ_{ripple}
Healthy	1.33	0.0174	1.42	0.0173	2.39	0.0171	2.74	0.0250
HRC1	1.34	0.0177	1.42	0.0166	2.46	0.0189	2.74	0.0228
HRC2	1.34	0.0181	1.44	0.0166	2.49	0.0179	2.78	0.0252
HRC3	1.35	0.0185	1.43	0.0178	2.48	0.0182	2.81	0.0247

at different load and speed states. However, this is due to the low severity levels that are considered for this fault in this study. Nevertheless, it can be concluded that the torque and flux ripple are increasing as the fault becomes intense. Besides that, HRC fault shows the same effect as TTSC fault on the switching frequency of DTC as shown in Fig. 6.2, [22].

Demagnetization fault has the most significant effect on the torque and flux ripple at different speed and load conditions in comparison with the other considered faults, as shown in Table 6.3.

It is worth noting that DTC reacts to the demagnetization effect by reducing the switching

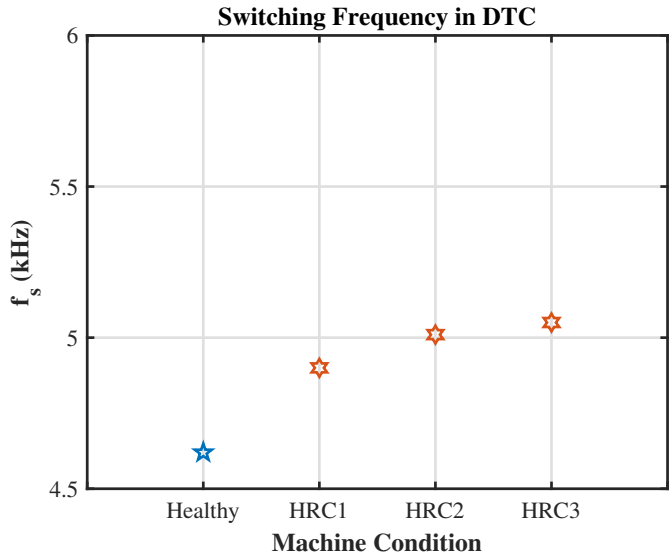

Figure 6.2: Switching frequency in DTC under healthy case and different HRC fault severities.

Table 6.3: The effect of demagnetization fault on the torque and flux ripple of PMSM [B].

	DTC Operating Point							
	20N.m/350rpm		**20N.m/700rpm**		**40N.m/350rpm**		**40N.m/700rpm**	
Case	t_{ripple}	λ_{ripple}	t_{ripple}	λ_{ripple}	t_{ripple}	λ_{ripple}	t_{ripple}	λ_{ripple}
Healthy	1.33	0.0174	1.42	0.0173	2.39	0.0171	2.74	0.0250
Demag1	2.04	0.0247	2.44	0.0273	3.98	0.0255	5.07	0.0333
Demag2	2.93	0.0278	3.69	0.0337	5.66	0.0281	7.37	0.0345
Demag3	3.75	0.0321	4.42	0.0341	7.11	0.0314	8.69	0.0373

frequency as shown in Fig. 6.3. This is a result of the drop in the average torque, which is below lower hysteresis band [69]. As a result, DTC reacts to the torque error due to the fault by commanding only voltage vectors that would increase the torque.

6.2 Faulty Machine Analysis in MT Frame

Faults could occur either on the machine side or the drive side where they have different effects on the drive performance. These effects can be included in the equivalent circuit

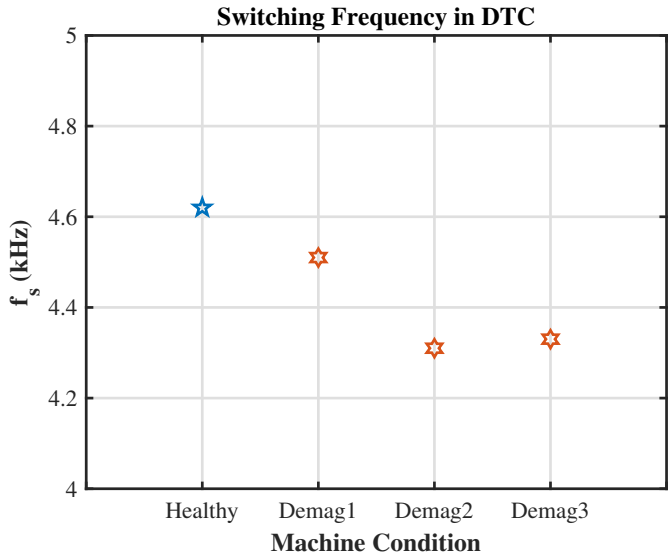

Figure 6.3: Switching frequency in DTC under healthy case and different demagnetization fault severities.

model of the PMSM, as described in (6.3).

$$\begin{aligned} \hat{v}_M &= v_M + v_{Mf} \\ \hat{v}_T &= v_T + v_{Tf} \end{aligned} \tag{6.3}$$

Here, v_{Mf} and v_{Tf} are the MT voltage deviations due to faults and $\hat{v}_M$ and $\hat{v}_T$ are the MT voltages considering the fault effects.

The effect of TTSC fault on PMSM model can be obtained by transforming the faulty (abc) model in (3.21) using (2.6) and then (2.13). The resultant faulty PMSM model in MT

frame under TTSC fault is described in (6.4).

$$
\begin{aligned}
v_M &= r_s i_M + \frac{2}{3} r_{s_f} \cos(\theta_r + \delta)\, i_f + \left(L_q - L_d\right) \frac{d\delta}{dt} \sin(2\delta)\, i_M \\
&+ \left(L_q - L_d\right) \frac{d\delta}{dt} \cos(2\delta)\, i_T - \frac{2}{3} \left(\omega + \frac{d\delta}{dt}\right) \left(\left(L_{s_f} + L_{hf}\right) \sin(\theta + \delta)\, i_f\right) \\
&+ \left(L_d \cos^2(\delta) + L_q \sin^2(\delta)\right) \frac{di_M}{dt} + \left(L_q - L_d\right) \cos(\delta) \sin(\delta) \frac{di_T}{dt} \\
&+ \frac{2}{3} \left(L_{s_f} + L_{hf}\right) \cos(\theta + \delta) \frac{di_f}{dt} - \frac{d\delta}{dt} \lambda_{PM} \sin(\delta) \\
&- \left(\omega + \frac{d\delta}{dt}\right) \left[\left(L_q - L_d\right) \cos(\delta) \sin(\delta)\, i_M + \left(L_d \sin^2(\delta) + L_q \cos^2(\delta)\right) i_T\right] \\
&+ \left(\omega + \frac{d\delta}{dt}\right) \left[\frac{2}{3} \left(L_{s_f} + L_{hf}\right) \sin(\theta + \delta)\, i_f + \lambda_{PM} \sin(\delta)\right] \\
v_T &= r_s i_T - \frac{2}{3} r_{s_f} \sin(\theta_r + \delta)\, i_f + \left(L_q - L_d\right) \frac{d\delta}{dt} \cos(2\delta)\, i_M \\
&- \left(L_q - L_d\right) \frac{d\delta}{dt} \sin(2\delta)\, i_T - \frac{2}{3} \left(\omega + \frac{d\delta}{dt}\right) \left(\left(L_{s_f} + L_{hf}\right) \cos(\theta + \delta)\, i_f\right) \\
&+ \left(L_d \sin^2(\delta) + L_q \cos^2(\delta)\right) \frac{di_T}{dt} + \left(L_q - L_d\right) \cos(\delta) \sin(\delta) \frac{di_M}{dt} \\
&- \frac{2}{3} \left(L_{s_f} + L_{hf}\right) \sin(\theta + \delta) \frac{di_f}{dt} - \frac{d\delta}{dt} \lambda_{PM} \cos(\delta) \\
&+ \left(\omega + \frac{d\delta}{dt}\right) \left[\left(L_q - L_d\right) \cos(\delta) \sin(\delta)\, i_T + \left(L_d \cos^2(\delta) + L_q \sin^2(\delta)\right) i_M\right] \\
&+ \left(\omega + \frac{d\delta}{dt}\right) \left[\frac{2}{3} \left(L_{s_f} + L_{hf}\right) \cos(\theta + \delta)\, i_f + \lambda_{PM} \cos(\delta)\right]
\end{aligned}
\tag{6.4}
$$

Upon comparing (2.7) to the resultant faulty PMSM model in MT frame under TTSC fault, the additional terms, given in (6.5), are due to TTSC fault.

$$
\begin{aligned}
v_{Mf} &= \frac{2}{3} \left(r_{s_f} i_f + \left(L_{hf} + L_{s_f}\right) \frac{di_f}{dt}\right) \cos(\theta_r + \delta) \\
v_{Tf} &= -\frac{2}{3} \left(r_{s_f} i_f + \left(L_{hf} + L_{s_f}\right) \frac{di_f}{dt}\right) \sin(\theta_r + \delta)
\end{aligned}
\tag{6.5}
$$

The circulating short circuit current, described in (6.6) could be assumed nearly sinusoidal

following the sinusoidal phase back-EMF of the studied machine.

$$i_f = \left|I_f\right| \sin\left(\theta_r + \delta + \phi\right) \tag{6.6}$$

Here (ϕ) represents the phase angle of the fault current. As a result, the MT voltage deviation due to TTSC at steady state, have a DC shift in the first term and oscillation in the second term, as described in (6.7)

$$\begin{aligned} v_{Mf} &= \frac{1}{3} r_{s_f} \left|I_f\right| \left(\sin\left(\phi\right) + \sin\left(2\theta_r + 2\delta + \phi\right)\right) \\ v_{Tf} &= -\frac{1}{3} r_{s_f} \left|I_f\right| \left(\cos\left(\phi\right) - \cos\left(2\theta_r + 2\delta + \phi\right)\right) \end{aligned} \tag{6.7}$$

Therefore, it is expected that the M-axis voltage increases while T-axis voltage decreases under TTSC following the DC term in (6.7).

The voltage shift due to HRC could be represented, at steady state, by (6.8) and (6.9).

$$\begin{aligned} v_{Mf} = {} & \Delta r \cdot \cos^2\left(\theta_r + \delta - \frac{2\pi}{3}\right) \cdot i_M \\ & - \Delta r \cdot \cos\left(\theta_r + \delta - \frac{2\pi}{3}\right) \cdot \sin\left(\theta_r + \delta - \frac{2\pi}{3}\right) \cdot i_T \end{aligned} \tag{6.8}$$

$$\begin{aligned} v_{Tf} = {} & \Delta r \cdot \sin^2\left(\theta_r + \delta - \frac{2\pi}{3}\right) \cdot i_T \\ & - \Delta r \cdot \cos\left(\theta_r + \delta - \frac{2\pi}{3}\right) \cdot \sin\left(\theta_r + \delta - \frac{2\pi}{3}\right) \cdot i_M \end{aligned} \tag{6.9}$$

It can be noticed that the voltage deviations in MT frame due to HRC has a DC shift in the first term and oscillating one in the second term, similarly to the ITSC fault. However, the DC term for both MT voltages would increase under HRC fault.

As expected from (6.10), the stator flux linkage magnitude would decrease under the demagnetization fault, as does the magnetizing current [70]. Here k_a and k_s are the approximation coefficients.

$$i_M = k_s \lambda_s - k_a \lambda_{PM} \tag{6.10}$$

As a result, the M-axis voltage is decreased directly, as described in (6.11). Here, $\Delta\lambda_{sf}$ and $\Delta\lambda_{PMf}$ are the changes in stator flux linkage and PM flux linkage magnitudes due to demagnetization. It is worth noting that $\Delta\lambda_{PMf} \ll \Delta\lambda_{sf}$.

$$\begin{aligned} v_{Mf} &= -r_s k_s \Delta\lambda_{sf} + r_s k_a \Delta\lambda_{PMf} \\ v_{Tf} &= 0 \end{aligned} \tag{6.11}$$

6.2.1 Numerical Results

As expected from the analysis, the studied faults show a unique trend in the MT frame. The voltages shift toward the southeast for TTSC, northeast for HRC and west for demagnetization, as shown in Fig. 6.4 under different operating conditions. It could be observed that the operating conditions impact the magnitude of the MT voltages. Nevertheless, the direction of the shift in the commanded MT voltages holds under different fault conditions regardless of the speed and load.

6.2.1.1 Detection and Classification

The SVM classifier is utilized for identifying the health state of the machine and the fault types in the event of a fault. The feature vector contains the commanded MT voltages for healthy and faulty conditions. Table 6.4 shows the accuracy of SVM in detecting and classifying faults in DTC driven PMSM at different operating points. The SVM classifier can

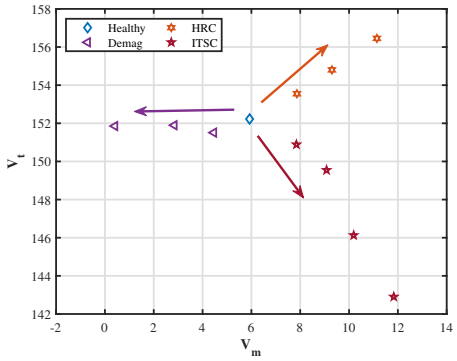

(a) $(t^*_{e2}, |\lambda^*_{s2}|)$ - 350 rpm.

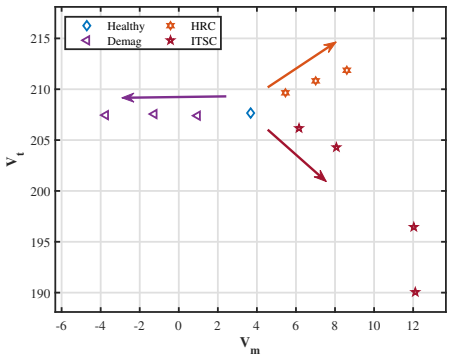

(b) $(t^*_{e2}, |\lambda^*_{s2}|)$ - 700 rpm.

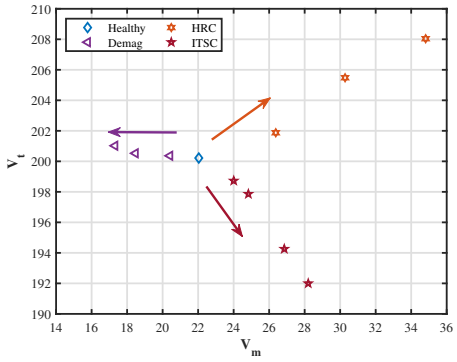

(c) $(t^*_{e3}, |\lambda^*_{s3}|)$ - 350 rpm.

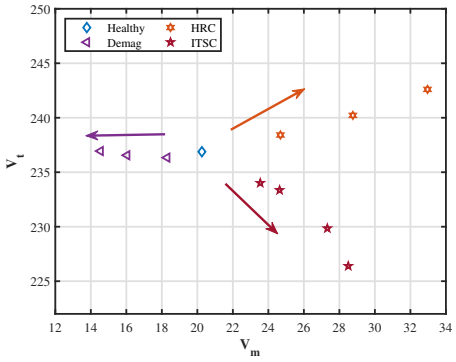

(d) $(t^*_{e3}, |\lambda^*_{s3}|)$ - 700 rpm.

Figure 6.4: Simulation results for the variation in $(V_m - V_t)$ for healthy and three different fault conditions at different speeds and load conditions (the arrow direction is with the increase in the fault severity).

Table 6.4: Simulation Results of Detection Accuracy in DTC driven PMSM using Commanded MT Voltages.

	SVM: Stage I		
Machine Status	$(t^*_{e1}, \|\lambda^*_{s1}\|)$	$(t^*_{e2}, \|\lambda^*_{s2}\|)$	$(t^*_{e3}, \|\lambda^*_{s3}\|)$
Healthy	93.3%	100%	100%
SC1	93.3%	80.0%	96.7%
HRC1	93.3%	80.0%	96.7%
Demag1	100%	100%	100%
Overall Accuracy	95.0%	90.0%	98.3%

accurately distinguish between normal machine operation and faulty operation, and identify the type of fault under different load conditions.

6.2.1.2 Effect of Noise on Detection Accuracy

The detection accuracy of SVM classifier utilizing commanded MT voltages in DTC driven PMSM is evaluated in the presence of AWGN to investigate the potential impact of measurement noise and manufacturing variations on the accuracy of fault detection. To modify the SNR ratio, the variance of the noise is adjusted. Table 6.5 shows the overall detection accuracy using SVM at different SNR levels at both load conditions. It can be observed

Table 6.5: Simulation Results of Detection Accuracy in DTC driven PMSM using Commanded MT Voltages at Different SNR Levels.

	SVM: Stage I		
SNR(dB)	$(t^*_{e1}, \lvert\lambda^*_{s1}\rvert)$	$(t^*_{e2}, \lvert\lambda^*_{s2}\rvert)$	$(t^*_{e3}, \lvert\lambda^*_{s3}\rvert)$
No Noise	95.0%	90.0%	98.3%
40	93.3%	90.0%	97.5%
30	87.5%	82.5%	85.8%
20	80.0%	75.0%	81.7%

that the introduced noise has an impact, but the performance of the SVM classifier remains adequate.

6.2.1.3 Effectiveness of Alternative Classifiers for Fault Detection

The viability of utilizing alternative classifiers for fault diagnosis, in conjunction with the commanded MT voltages method, is examined in DTC driven PMSMs. Specifically, the LDA and k-NN classifiers are employed using the same training data as the SVM classifier. The fault diagnosis accuracy of the LDA and 3-NN classifiers in DTC driven PMSMs is presented in Tables 6.6 and 6.7, respectively. It can be concluded that the SVM and 3-NN classifiers are more effective than the LDA classifier in detecting faults in DTC driven PMSMs using the commanded MT voltages method.

Table 6.6: Simulation Results of Detection Accuracy using LDA Classifier with the Commanded MT Voltages in DTC driven PMSM.

	LDA Classifier		
Machine Status	$(t^*_{e1}, \lvert\lambda^*_{s1}\rvert)$	$(t^*_{e2}, \lvert\lambda^*_{s2}\rvert)$	$(t^*_{e3}, \lvert\lambda^*_{s3}\rvert)$
Healthy	70.0%	100%	100%
SC1	60.0%	30.0%	40.0%
HRC1	90.0%	30.0%	100%
Demag1	90.0%	90.0%	90.0%
Overall Accuracy	77.5%	52.5%	82.5%

Table 6.7: Simulation Results of Detection Accuracy using k-NN Classifiers with the Commanded MT Voltages in DTC driven PMSM.

	k-NN Classifier		
Machine Status	$(t^*_{e1}, \lvert\lambda^*_{s1}\rvert)$	$(t^*_{e2}, \lvert\lambda^*_{s2}\rvert)$	$(t^*_{e3}, \lvert\lambda^*_{s3}\rvert)$
Healthy	100%	100%	100%
SC1	80.0%	90.0%	100%
HRC1	80.0%	80.0%	90.0%
Demag1	100%	100%	100%
Overall Accuracy	90.0%	92.5%	97.5%

6.2.1.4 Identifying the Fault Severity

Once the fault class is determined in the first stage of the SVM classifier, the second stage of the classifier is used to assess the severity level of the identified fault. The accuracy of the SVM, in conjunction with the commanded MT voltages method, is presented in Table 6.8 for estimating the fault severity. It is evident that the SVM model demonstrates proficiency in predicting the severity of all faults. Nevertheless, it encounters challenges in discerning between different severity levels in case of TTSC fault.

6.2.2 Experimental Results

The variations in MT voltages in DTC under healthy and TTSC fault cases are shown in Fig. 6.5. As expected, in the MT frame the TTSC fault shows a unique trend toward the

Table 6.8: Simulation Results of Severity Estimation Accuracy in DTC driven PMSM using the Commanded MT Voltages.

Machine Status	SVM: Stage II		
	$(t^*_{e1}, \lvert\lambda^*_{s1}\rvert)$	$(t^*_{e2}, \lvert\lambda^*_{s2}\rvert)$	$(t^*_{e3}, \lvert\lambda^*_{s3}\rvert)$
TTSC	72.5%	93.3%	95.0%
SC1	60.0%	86.7%	96.7%
SC2	83.3%	93.3%	93.3%
SC3	70.0%	96.7%	93.3%
SC4	76.7%	96.7%	96.7%
HRC	95.0%	100%	100%
HRC1	100%	100%	100%
HRC2	90.0%	100%	100%
HRC3	95.0%	100%	100%
Demagnetization	100%	100%	100%
Demag1	100%	100%	100%
Demag2	100%	100%	100%
Demag3	100%	100%	100%

southeast. This shift could be utilized in a fault detection scheme and used further for severity estimation.

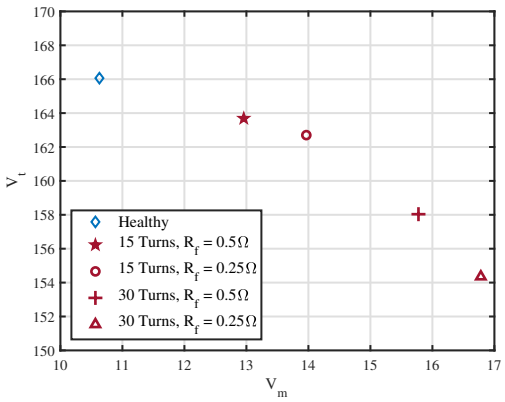

(a) Commanded MT Voltages Shift under TTSC fault at $(t^*_{e2}, \lvert\lambda^*_{s2}\rvert)$ - 300 rpm.

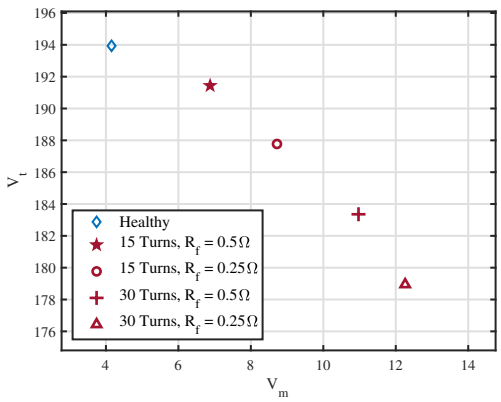

(b) Commanded MT Voltages Shift under TTSC fault at $(t^*_{e2}, \lvert\lambda^*_{s2}\rvert)$ - 600 rpm.

Figure 6.5: Experimental results for the variation in $(V_m - V_t)$ for healthy and TTSC fault.

The variations in switching frequency in DTC under healthy and TTSC fault cases are

Table 6.9: Experimental Results of Detection Accuracy in DTC driven PMSM at different loads using the Commanded MT Voltages.

Machine Status	SVM: Stage I	
	$(t^*_{e1}, \lvert\psi^*_{s1}\rvert)$	$(t^*_{e2}, \lvert\psi^*_{s2}\rvert)$
Healthy	90.0%	100%
SC1	100%	100%
Overall Accuracy	95.0%	100%

depicted in Fig. 6.6. It could be observed that DTC reacts to the TTSC effect by increasing the switching frequency as found in the simulation results.

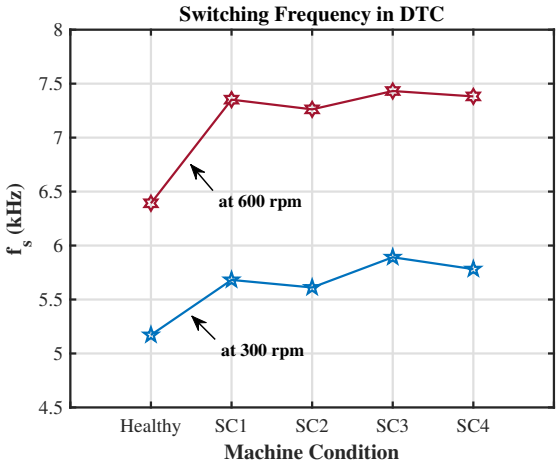

Figure 6.6: Switching frequency in DTC under healthy case and different TTSC fault severities.

6.2.2.1 Detection and Severity Estimation

The performance of the SVM classifier, combined with the commanded MT voltage approach, is evaluated in detecting TTSC faults and assessing their severity in various operating conditions. Tables 6.9 and 6.10 present the accuracy of fault detection in the initial stage and fault severity evaluation in the subsequent stage, respectively. The results demonstrate that the SVM classifier with the commanded MT voltage approach is effective in detecting and assessing the severity of TTSC faults.

Table 6.10: Experimental Results of Severity Estimation Accuracy in DTC driven PMSM using the Commanded MT Voltages.

Machine Status	SVM: Stage II	
	$(t^*_{e1}, \lvert\psi^*_{s1}\rvert)$	$(t^*_{e2}, \lvert\psi^*_{s2}\rvert)$
TTSC	80.8%	87.5%
SC1	70.0%	73.3%
SC2	86.7%	93.3%
SC3	83.3%	93.3%
SC4	83.3%	90.0%

6.3 Power Signature Analysis

The application of power signature analysis for the identification of faults in inverter driven induction machines is a well-recognized strategy, and its advantageous performance has recently been leveraged for inverter driven PMSMs. The power theory is used for anomaly detection as an alternative approach for using current or voltage signals separately [3, 9, 10]. This is due to the fact that the power signal is less sensitive to the controller bandwidth as it combines the spectral information from both signals at any bandwidth. The authors in [3] suggests use of the second harmonic in the instantaneous active power for short circuit fault detection in generating mode, whereas the instantaneous reactive power is used in motoring mode. In [10], reduction of the sixth harmonic amplitude of active power is one of the utilized methods to detect the presence of static eccentricity. However, if the ultimate aim is reliable fault detection and separation, multi-feature analysis has to be adopted to avoid misclassification. This section provides the utilization of the power theory for fault diagnosis in inverter driven PMSMs.

6.3.1 Diagnosis Approach

The developed diagnosis method uses the measured currents and commanded voltages to calculate active and reactive power signals. Features extracted from both signals have been shown to aid fault separation between HRC and TTSC. The new approach utilizes the SVM classifier in two cascaded stages, shown in Fig. 6.7. In the first stage, the classifier aims to detect the fault existence and fault class. Afterward, the second stage of the classifier is dedicated to the fault severity estimation. The proposed approach is performed in the following steps:

1. Compute the active and reactive power $(p(t), q(t))$ signals. The measured current signals and commanded voltages transformed into the $\alpha\beta$ frame, as indicated in (6.12).

$$\begin{aligned} p(t) &= \Re(s(t)) = \frac{3}{2}(v_\alpha(t)i_\alpha(t) + v_\beta(t)i_\beta(t)) \\ q(t) &= \Im(s(t)) = \frac{3}{2}(v_\beta(t)i_\alpha(t) - v_\alpha(t)i_\beta(t)) \end{aligned} \tag{6.12}$$

   where the complex power $s(t)$ is given by the product of the stator voltage and current space vectors $(\overrightarrow{v_s}, \overrightarrow{i_s})$ as following:

$$s(t) = \frac{3}{2}[\overrightarrow{v_s} \cdot \overrightarrow{i_s}^*] = \frac{3}{2}[(v_\alpha + jv_\beta) \cdot (i_\alpha + ji_\beta)^*] \tag{6.13}$$

   As mentioned earlier, the DTC drive requires these current signals to calculate the torque and flux linkages. The commanded voltages are generated by the voltage vector selection table.

2. Use FFT to find the DC, 2^{nd}, and 6^{th} spectral components in active and reactive power. The power spectrum, both active and reactive, contains valuable information

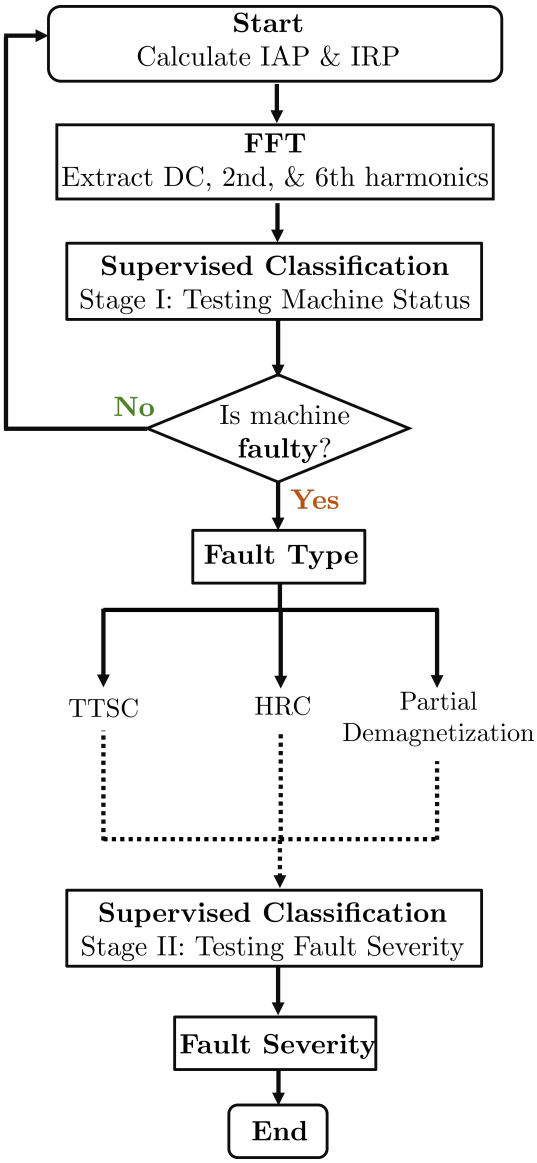

Figure 6.7: Fault diagnosis flow chart.

pertaining to fault events in stator current and voltage signals, independent of the reference frame or controller bandwidth [1]. The stator current and voltage space vectors consist of fundamental component and other significant harmonics that could be used for detection as following [4]:

$$\overrightarrow{v_s} = v_1 e^{j(\omega t+\theta_v)} + v_3 e^{3j(\omega t+\theta_v)} + v_5 e^{-5j(\omega t+\theta_v)} + v_7 e^{7j(\omega t+\theta_v)} + ... \tag{6.14}$$

$$\overrightarrow{i_s} = i_1 e^{j(\omega t+\theta_i)} + i_3 e^{3j(\omega t+\theta_i)} + i_5 e^{-5j(\omega t+\theta_i)} + i_7 e^{7j(\omega t+\theta_i)} + ... \tag{6.15}$$

By applying (6.13) on (6.14) and (6.15), the resultant spectrum of the stator complex power space vector would be in:

$$\begin{aligned}\overrightarrow{s} = {} & v_1 i_1 e^{j(\theta_v-\theta_i)} + v_3 i_1 e^{j(2\omega t+3\theta_v-\theta_i)} \\ & + v_1 i_5 e^{j(6\omega t+\theta_v+5\theta_i)} + v_7 i_1 e^{j(6\omega t+7\theta_v-\theta_i)} + ...\end{aligned} \tag{6.16}$$

The significant spectral components with positive sequence only are shown in (6.16).

In [71], it was demonstrated that the DC and second harmonic components in the power signals can be used to identify electrical imbalances resulting from TTSC or HRC in induction machines. Additionally, reference [1] indicated that the first to fifteenth harmonics in IRP can be employed to differentiate faults related to magnetic and electrical asymmetry in the machine. However, here it is shown that the sixth harmonic, among other harmonics, exhibit significant separation between healthy and faulty cases, as evidenced by the active power spectrum in Fig. 6.8.

As a result, a reduced number of harmonics are used as classification features, thus eliminating the redundancy observed in [1]. The investigation indicated that using these three features not only yields accurate fault detection but also separation between HRC and TTSC faults. Fig. 6.9 shows the magnitude variation of these features under the considered faults at different severity levels.

3. Apply SVM classifier to determine the machine condition, healthy or faulty. In case of a faulty indication, the classifier will specify the fault type. The training data for the classifier contains samples from different load and speed conditions for healthy and the

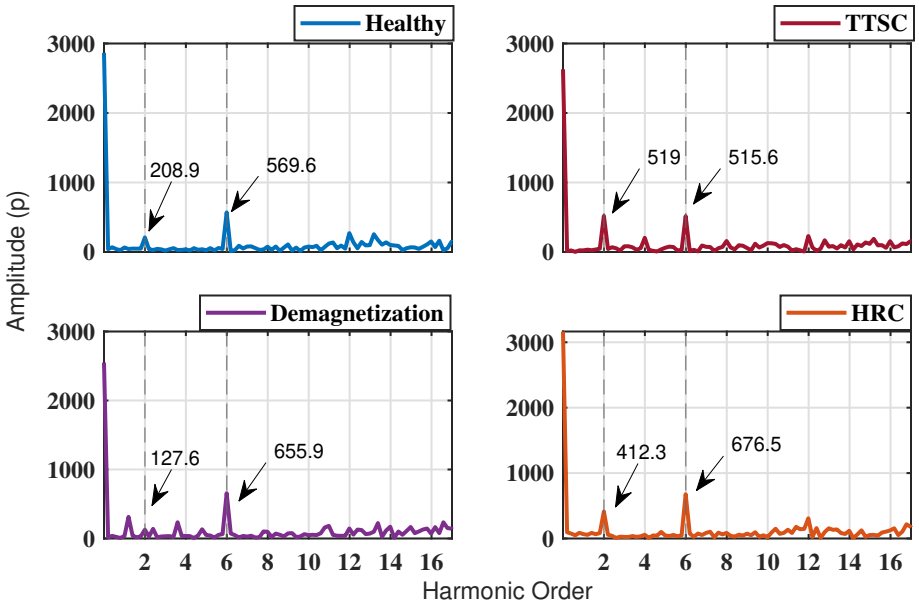

Figure 6.8: Active power spectrum for healthy and faulty conditions.

lowest severity cases of all faults. The faulty indication should be one of the following: TTSC, demagnetization, or HRC.

4. Apply SVM to determine the fault severity level that is predefined in the training pool. The second stage of SVM classification is based on the samples from the indicated fault only.

6.3.2 Numerical Results

Three operating conditions, as shown in Fig. 6.10, are chosen from the MTPA $(t_e^*, |\lambda_s^*|)$ profile to run the machine in the torque regulation mode using DTC drive. These operating points are listed in Table 6.11. To create the training samples for SVM classifier learning, the machine runs at ten different speeds ranging from 250 rpm to 700 rpm in steps of 50 rpm. This results in a total of 10 samples for the healthy case, 40 samples for the TTSC fault (divided into four severity levels), 30 samples for the demagnetization fault (divided

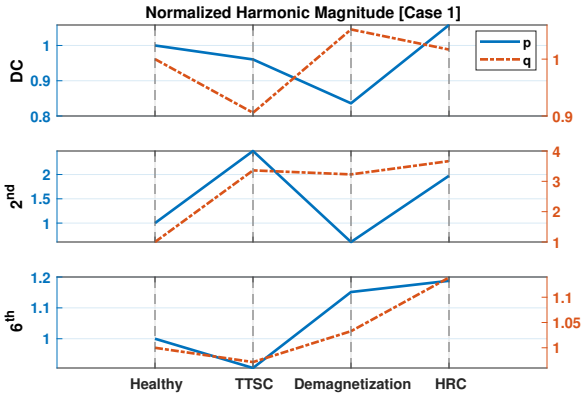

(a) Case of low severe faults: TTSC at ($i_f = 25\%I_{rated}$), Demagnetization at ($6\%\lambda_{PM}$ reduction), and HRC at ($100\%r_s$ increase).

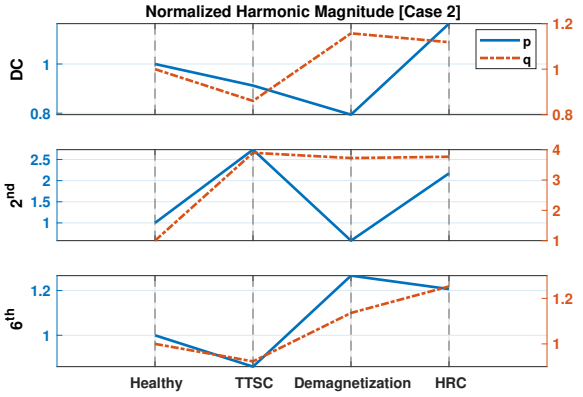

(b) Case of more severe faults: TTSC at ($i_f = 32\%I_{rated}$), Demagnetization at ($14\%\lambda_{PM}$ reduction), and HRC at ($150\%r_s$ increase).

Figure 6.9: Harmonic magnitude variations in active and reactive power between healthy and faulty conditions.

Table 6.11: Operating points of the DTC Drive.

Operating points	**Value**
$(t^*_{e1}, \lvert\lambda^*_{s1}\rvert)$	(10Nm,0.37Wb)
$(t^*_{e2}, \lvert\lambda^*_{s2}\rvert)$	(20Nm,0.52Wb)
$(t^*_{e3}, \lvert\lambda^*_{s3}\rvert)$	(40Nm,0.67Wb)

into three severity levels), and 30 samples for the HRC fault (divided into three severity levels).

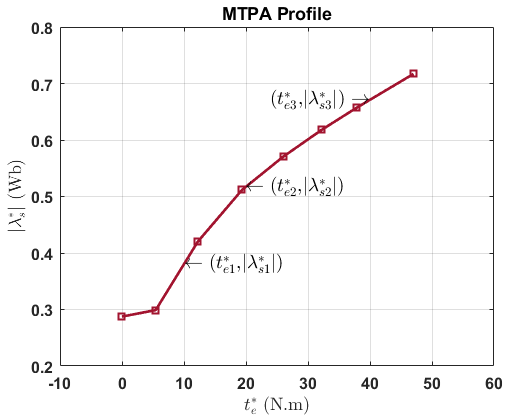

Figure 6.10: Stator flux linkage versus the electromagnetic torque.

6.3.2.1 Detection and Classification

The first phase of the diagnostic approach is to indicate the condition of the machine. If the machine is found to be faulty, the SVM classifier is used to identify the fault type. Table 6.12 presents the accuracy of detecting and classifying faults at different operating points. It can be observed that the SVM classifier is capable of identifying whether the machine is operating normally or experiencing a fault under different loading conditions. The fault with fully demagnetized magnets is highly detectable in DTC driven PMSMs due to its significant impact on the performance of the DTC. On the other hand, the accuracy for detecting healthy, TTSC, and HRC conditions is adequate. At lower speeds, the SVM classifier is unable to distinguish between the healthy case and the least severe cases of TTSC

Table 6.12: Simulation Results of Detection Accuracy in DTC driven PMSM at different loads using PQ Theory.

	SVM: Stage I		
Machine Status	$(t^*_{e1},\|\lambda^*_{s1}\|)$	$(t^*_{e2},\|\lambda^*_{s2}\|)$	$(t^*_{e3},\|\lambda^*_{s3}\|)$
Healthy	96.7%	93.3%	83.3%
SC1	100%	90.0%	90.0%
HRC1	93.3%	93.3%	76.7%
Demag1	100%	100%	93.3%
Overall Accuracy	97.5%	94.2%	85.8%

and HRC faults due to their comparable effects on the performance of the drive. It is worth noting that the accuracy of classification decreases under high loads, potentially as a result of magnetic saturation of the machine. In general, the SVM classifier can successfully separate between faults even when trained on a limited number of samples.

6.3.2.2 Effect of Noise on Detection Accuracy

To evaluate the potential impact of measurement noise and manufacturing variations within inverter driven PMSMs, the detection accuracy of SVM classifier utilizing power signature analysis in DTC driven PMSM is evaluated in the presence of additive white Gaussian noise (AWGN). The variance of the noise is adjusted to alter the SNR ratio. Table 6.13 shows the overall detection accuracy using SVM at different SNR levels at both load conditions. It can be noticed from Table 6.13 that the SVM classifier is immune to the included noise. This is due to the fact the SVM classifier depends on the support vectors that gives the maximum separation between classes. However, it is worth mentioning that the noise adds difficulty for SVM classifier in separating between healthy and HRC fault at low severity levels. As shown in Table 6.14, high noise levels mask the impact of low severe HRC fault. Inaccurate classification of low severity HRC is potentially due to the minimal impact this fault has on the stator flux linkage angle. As illustrated in Fig. 3.16, the magnitude of the stator flux linkage reduces, but the angle does not change.

Table 6.13: Simulation Results of Detection Accuracy in DTC driven PMSM at Different SNR Levels using PQ Theory.

	SVM: Stage I		
SNR(dB)	$(t^*_{e1}, \lvert\lambda^*_{s1}\rvert)$	$(t^*_{e2}, \lvert\lambda^*_{s2}\rvert)$	$(t^*_{e3}, \lvert\lambda^*_{s3}\rvert)$
No Noise	97.5%	94.2%	85.8%
40	97.5%	92.5%	84.2%
30	95.0%	91.7%	81.7%
20	86.7%	86.7%	75.8%

Table 6.14: HRC Detection Accuracy in DTC Driven PMSM at Different SNR Levels Using FEA Results using PQ Theory.

Operating Point	**SNR(dB)**	**HRC1 Detection Accuracy**
$(t^*_{e1}, \lvert\lambda^*_{s1}\rvert)$	No Noise	80.0%
	40	70.0%
	30	60.0%
	20	50.0%
$(t^*_{e2}, \lvert\lambda^*_{s2}\rvert)$	No Noise	80.0%
	40	70.0%
	30	60.0%
	20	50.0%
$(t^*_{e3}, \lvert\lambda^*_{s3}\rvert)$	No Noise	80.0%
	40	80.0%
	30	80.0%
	20	70.0%

6.3.2.3 Effectiveness of Alternative Classifiers for Fault Detection

To assess the effectiveness of using alternative classifiers for fault diagnosis in DTC driven PMSM, the LDA and k-NN classifiers are used here with the power signature analysis approach. The training pool is the same one used for the SVM classifier. Tables 6.15 and 6.16 provides the accuracy of fault detection and classification in DTC driven PMSM using the LDA and 3-NN classifiers, respectively. The findings indicate that the SVM classifier exhibits superior performance compared to the LDA and 3-NN classifiers in diagnosing faults in a DTC driven PMSM.

Table 6.15: Simulation Results of Detection Accuracy using LDA Classifier in DTC driven PMSM using PQ Theory.

	LDA Classifier		
Machine Status	$(t^*_{e1}, \lvert\lambda^*_{s1}\rvert)$	$(t^*_{e2}, \lvert\lambda^*_{s2}\rvert)$	$(t^*_{e3}, \lvert\lambda^*_{s3}\rvert)$
Healthy	70.0%	90.0%	100%
SC1	100%	90.0%	60.0%
HRC1	80.0%	80.0%	50.0%
Demag1	100%	100%	100%
Overall Accuracy	87.5%	90.0%	77.5%

Table 6.16: Simulation Results of Detection Accuracy using k-NN Classifiers in DTC driven PMSM using PQ Theory.

	k-NN Classifier		
Machine Status	$(t^*_{e1}, \lvert\lambda^*_{s1}\rvert)$	$(t^*_{e2}, \lvert\lambda^*_{s2}\rvert)$	$(t^*_{e3}, \lvert\lambda^*_{s3}\rvert)$
Healthy	70.0%	70.0%	40.0%
SC1	100%	80.0%	60.0%
HRC1	70.0%	30.0%	40.0%
Demag1	90.0%	90.0%	20.0%
Overall Accuracy	82.5%	67.5%	40.0%

Table 6.17: Simulation Results of Severity Estimation Accuracy in DTC driven PMSM using PQ Theory.

	SVM: Stage II		
Machine Status	$(t^*_{e1}, \lvert\lambda^*_{s1}\rvert)$	$(t^*_{e2}, \lvert\lambda^*_{s2}\rvert)$	$(t^*_{e3}, \lvert\lambda^*_{s3}\rvert)$
TTSC	94.1%	86.6%	80.0%
SC1	96.6%	96.6%	73.3%
SC2	96.6%	93.3%	80.0%
SC3	90.0%	83.3%	80.0%
SC4	93.3%	73.3%	86.6%
HRC	96.6%	95.0%	85.0%
HRC1	90.0%	100%	80.0%
HRC2	100%	85.0%	75.0%
HRC3	100%	100%	100%
Demagnetization	100%	96.6%	86.6%
Demag1	100%	100%	80.0%
Demag2	100%	90.0%	95.0%
Demag3	100%	100%	85.0%

6.3.2.4 Identifying the Fault Severity

This is a crucial component of fault diagnosis, as it enables the selection of an appropriate online mitigation technique or the scheduling of preventive maintenance. The accuracy of the SVM in estimating fault severity is presented in Table 6.17. It can be noticed that the SVM is able to predict the severity of all faults, but it struggles to distinguish between TTSC cases with varying fault resistance. This is likely because the short circuit current resulting

from TTSC is dependent on the speed, number of shorted turns, and fault resistance, as mentioned in [43]. Different classes of TTSC faults may potentially result in the same fault current. It is shown in Fig. 6.11 that the fault current resulting from 15 shorted turns with 0.5Ω fault resistance in a machine operating at 10Nm and 500 rpm has the same amplitude as that of a machine operating at 10Nm and 250 rpm with 30 shorted turns through a 0.25Ω fault resistance.

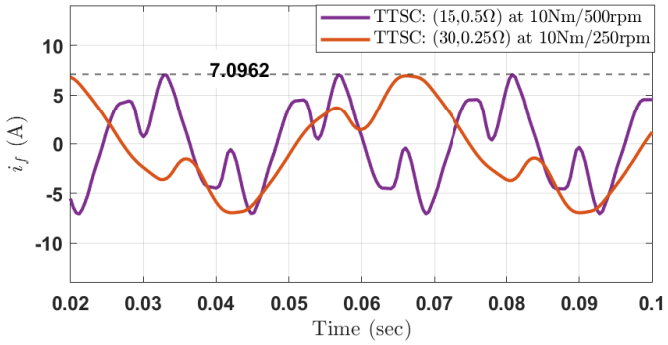

Figure 6.11: The short circuit current produced by an TTSC fault.

6.3.2.5 Impact of the FOC Drive on Diagnosis

In order to evaluate the sensitivity of the proposed methodology for detecting faults in PMSM driven by FOC, comparable MTPA loading levels to those utilized in DTC are employed during FOC operation. The currents of 5A and 10A at an excitation angle of 120° are corresponding to $(t^*_{e1}, |\lambda^*_{s1}|)$ and $(t^*_{e2}, |\lambda^*_{s2}|)$ in DTC, respectively. This is can be seen in Fig. 6.12.

Identical sample size, as in DTC case, is generated at each load condition in FOC for the healthy and faulty machine conditions. According to the results presented in Table 6.18, the use of power signature analysis in conjunction with an SVM classifier for diagnostic purposes continues to be a feasible option for PMSMs driven by FOC, even when subjected to 40dB of AWGN.

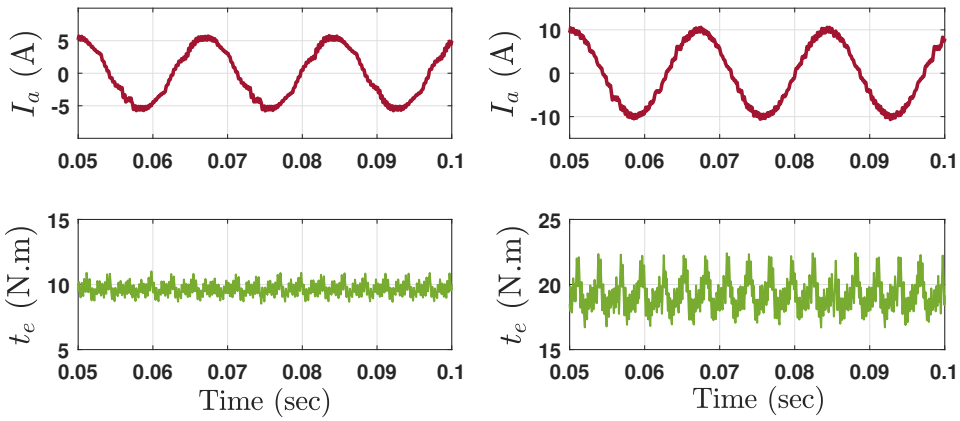

Figure 6.12: The resultant stator current at the corresponding actual machine torque in DTC driven PMSM: (Left) 5A at $(t_{e1}^*, |\lambda_{s1}^*|)$, (Right) 10A at $(t_{e2}^*, |\lambda_{s2}^*|)$.

Table 6.18: Simulation Results of Detection Accuracy in FOC driven PMSM at different loads using PQ Theory.

	SVM: Stage I			
	Without AWGN		With AWGN	
Machine Status	5A	10A	5A	10A
Healthy	96.7%	86.7%	96.6%	80.0%
SC1	93.3%	93.3%	93.3%	93.3%
HRC1	96.7%	80.0%	90.0%	73.3%
Demag1	100%	90.0%	93.3%	83.3%
Overall Accuracy	96.7%	87.5%	93.3%	82.5%

6.3.3 Experimental Results

In order to ensure the machine operates within a safe range, only the operating conditions of $(t_{e1}^*, |\lambda_{s1}^*|)$ and $(t_{e2}^*, |\lambda_{s2}^*|)$ are used here to run the machine in the torque regulation mode using DTC drive.

6.3.3.1 Detection and Severity Estimation

The accuracy of detecting the machine condition in the initial stage of the diagnostic methodology and evaluating the fault severity in the subsequent stage at various operating points is displayed in Tables 6.19 and 6.20. It can be noted that the SVM classifier, when combined

with power signature analysis, is capable of effectively detecting TTSC fault and assessing their severity.

Table 6.19: Experimental Results of Detection Accuracy in DTC driven PMSM at different loads using PQ Theory.

	SVM: Stage I	
Machine Status	$(t^*_{e1}, \lvert\psi^*_{s1}\rvert)$	$(t^*_{e2}, \lvert\psi^*_{s2}\rvert)$
Healthy	90.0%	80.0%
SC1	90.0%	90.0%
Overall Accuracy	90.0%	85.0%

Table 6.20: Experimental Results of Severity Estimation Accuracy in DTC driven PMSM using PQ Theory.

	SVM: Stage II	
Machine Status	$(t^*_{e1}, \lvert\psi^*_{s1}\rvert)$	$(t^*_{e2}, \lvert\psi^*_{s2}\rvert)$
TTSC	86.7%	89.2%
SC1	83.3%	86.7%
SC2	86.7%	93.3%
SC3	86.7%	86.7%
SC4	90.0%	90.0%

To address the influence of speed variations on the SVM classifier in practice, a new dataset is generated by running the machine at speeds slightly above and below the predetermined ones by ±5 rpm. The training phase utilizes the previously generated data, while the testing phase involves evaluating the performance of the SVM classifier using the newly collected dataset. The experimental outcomes of SVM classifier accuracy for detecting the TTSC fault and estimating its severity in DTC driven using PQ Theory under the influence of speed variations are presented in Tables 6.21 and 6.22, respectively.

6.3.3.2 Impact of the FOC Drive on Diagnosis

The effectiveness of the proposed methodology for fault detection is examined in PMSM driven by FOC at operating conditions comparable to those in the numerical investigation

Table 6.21: Experimental Results of Detection Accuracy in DTC driven using PQ Theory Considering the Speed Variations.

	SVM: Stage I	
Machine Status	$(t^*_{e1}, \lvert\psi^*_{s1}\rvert)$	$(t^*_{e2}, \lvert\psi^*_{s2}\rvert)$
Healthy	80.0%	80.0%
SC1	90.0%	80.0%
Overall Accuracy	85.0%	80.0%

Table 6.22: Experimental Results of Severity Estimation Accuracy in DTC driven PMSM using PQ Theory Considering the Speed Variations.

	SVM: Stage II	
Machine Status	$(t^*_{e1}, \lvert\psi^*_{s1}\rvert)$	$(t^*_{e2}, \lvert\psi^*_{s2}\rvert)$
TTSC	80.8%	88.8%
SC1	83.3%	83.3%
SC2	73.3%	85.0%
SC3	83.3%	93.3%
SC4	83.3%	93.3%

involving the TTSC fault. The same sample size is produced at each load condition in FOC for both the healthy and faulty machine under ITSC fault, similar to the DTC scenario. Tables 6.23 and 6.24 exhibit the accuracy in identifying the machine condition under TTSC fault during the first stage of the diagnostic method and estimating the fault severity during the second stage across different operational points. It is observed that the feasibility of utilizing power signature analysis in combination with an SVM classifier for diagnostic persists for PMSM operated by FOC.

Table 6.23: Experimental Results of Detection Accuracy in FOC driven PMSM at different loads using PQ Theory.

	SVM: Stage I	
Machine Status	5A	10A
Healthy	100%	100%
SC1	100%	90.0%
Overall Accuracy	100%	95.0%

Table 6.24: Experimental Results of Severity Estimation Accuracy in FOC driven PMSM using PQ Theory.

	SVM: Stage II	
Machine Status	5A	10A
TTSC	95.8%	90.0%
SC1	90.0%	83.3%
SC2	93.3%	86.7%
SC3	100%	93.3%
SC4	100%	93.3%

Chapter 7

Conclusion and Future Work

Condition monitoring of DTC driven PMSMs and executing the proper maintenance procedures assist in avoiding costly machine damage. However, the hysteresis comparators in DTC pose challenges in fault diagnosis for PMSMs. The compensating capability of DTC and switching frequency variations, determined by the hysteresis band, may result in unobservable fault impacts in DTC drives. Accordingly, the faulty operation of DTC driven PMSMs may lead to unstable control if the faults are not detected and mitigated properly in their early phases. Considering the DTC behavior mentioned above, the contributions of this work help in maintaining a safe and reliable DTC driven PMSM.

The necessity for a reliable fault diagnosis technique that suits DTC is demonstrated through a detailed analysis of the impact of the faults on the torque and flux comparators as well as the torque and flux estimation. It is shown that the hysteresis comparators are capable of masking the fault presence by adjusting the voltage vector and torque angle. The flux and torque estimation errors due to the presence of faults are not captured because the model does not consider the fault dynamics. Inclusion of the fault dynamics in the flux and torque estimation can improve performance.

A new technique is developed using the MT voltages to detect the presence of faults as well as estimate fault severity. The proposed machine models are used for fault detection and separation without the need for complex signal processing techniques. The other advantage

of this approach is that it maintains the simple structure feature of direct torque control as it requires only the available signals in the drive without additional sensors. The unique trend in the voltages aids detection and fault separation; however, classification algorithms enable severity estimation. It is shown that both k-NN and SVM are the most suited algorithms for acceptable accuracy even in the presence of noise.

Lastly, a noninvasive algorithm is developed to identify the faulty condition of inverter driven PMSM under FOC or DTC using the active and reactive power signature analysis. Spectral components of the power signals are used as fault indicators. This algorithm is capable of fault separation and severity estimation at different operating conditions without extra hardware components.

In addition, when employing one of the suggested methods to create the feature set for the SVM classifier, it has been demonstrated that the SVM classifier is a remarkably efficient technique for identifying and categorizing faults in PMSMs operated under FOC or DTC, even when there is limited training data and significant levels of noise. This performance improvement is noted for power signature analysis and commanded MT voltages yields; however, this is not the case for MVSA.

Future work will consider the following potential directions:

- **Explore Wavelet based diagnosis to detect eccentricity faults:** It was shown that eccentricity faults have a minimal impact on DTC driven PMSM as DTC compensates and tolerates the eccentricity effects by varying the switching frequency. Use of wavelet based diagnosis may isolate the switching frequency effect to detect the fault using the low frequency components.
- **Develop a fault mitigation scheme:** The control stability of the drive system may

deteriorate when faults occur and become severe as stability limits are dependent on machine parameters. The robustness improvement can be achieved by integrating a fault mitigation scheme once the fault is detected. Another solution may be to monitor the machine parameters using observers in order to keep the control system within the stability limits.

BIBLIOGRAPHY

[1] I. M. Allafi and S. N. Foster, "Fault Detection and Identification for Inverter-Driven Permanent Magnet Synchronous Machines," in *2021 IEEE 13th International Symposium on Diagnostics for Electrical Machines, Power Electronics and Drives (SDEMPED)*, vol. 1, 2021, pp. 358–364.

[2] S. Choi, M. S. Haque, M. T. B. Tarek, V. Mulpuri, Y. Duan, S. Das, V. Garg, D. M. Ionel, M. A. Masrur, B. Mirafzal, and H. A. Toliyat, "Fault Diagnosis Techniques for Permanent Magnet AC Machine and Drives—A Review of Current State of the Art," *IEEE Transactions on Transportation Electrification*, vol. 4, no. 2, pp. 444–463, 2018.

[3] B. Wang, J. Wang, A. Griffo, and B. Sen, "Stator Turn Fault Detection by Second Harmonic in Instantaneous Power for a Triple-Redundant Fault-Tolerant PM Drive," *IEEE Transactions on Industrial Electronics*, vol. 65, no. 9, pp. 7279–7289, 2018.

[4] R. Z. Haddad and E. G. Strangas, "On the Accuracy of Fault Detection and Separation in Permanent Magnet Synchronous Machines Using MCSA/MVSA and LDA," *IEEE Transactions on Energy Conversion*, vol. 31, no. 3, pp. 924–934, 2016.

[5] R. Z. Haddad, C. A. Lopez, S. N. Foster, and E. G. Strangas, "A Voltage-Based Approach for Fault Detection and Separation in Permanent Magnet Synchronous Machines," *IEEE Transactions on Industry Applications*, vol. 53, no. 6, pp. 5305–5314, 2017.

[6] W. G. Zanardelli, E. G. Strangas, and S. Aviyente, "Identification of Intermittent Electrical and Mechanical Faults in Permanent-Magnet AC Drives Based on Time–Frequency Analysis," *IEEE Transactions on Industry Applications*, vol. 43, no. 4, pp. 971–980, 2007.

[7] H. Chen, J. He, X. Guan, N. A. O. Demerdash, A. M. EL-Refaie, and C. H. T. Lee, "High-Resistance Connection Diagnosis in Five-Phase PMSMs Based on the Method of Magnetic Field Pendulous Oscillation and Symmetrical Components," *IEEE Transactions on Industrial Electronics*, vol. 69, no. 3, pp. 2288–2299, 2022.

[8] B. M. Ebrahimi and J. Faiz, "Feature Extraction for Short-Circuit Fault Detection in Permanent-Magnet Synchronous Motors Using Stator-Current Monitoring," *IEEE Transactions on Power Electronics*, vol. 25, no. 10, pp. 2673–2682, 2010.

[9] S. Huang, A. Aggarwal, E. G. Strangas, K. Li, F. Niu, and X. Huang, "Robust Stator Winding Fault Detection in PMSMs With Respect to Current Controller Bandwidth," *IEEE Transactions on Power Electronics*, vol. 36, no. 5, pp. 5032–5042, 2021.

[10] A. Aggarwal, E. G. Strangas, and J. Agapiou, "Comparative Study of Offline Detection Methods of Static Eccentricity for Interior Permanent Magnet Synchronous Machine,"

in *2019 IEEE 12th International Symposium on Diagnostics for Electrical Machines, Power Electronics and Drives (SDEMPED)*, 2019, pp. 75–81.

[11] H. Ahmed and A. K. Nandi, "Compressive Sampling and Feature Ranking Framework for Bearing Fault Classification With Vibration Signals," *IEEE Access*, vol. 6, pp. 44 731–44 746, 2018.

[12] M. Tsypkin, "The Origin of the Electromagnetic Vibration of Induction Motors Operating in Modern Industry: Practical Experience—Analysis and Diagnostics," *IEEE Transactions on Industry Applications*, vol. 53, no. 2, pp. 1669–1676, 2017.

[13] J. Harmouche, C. Delpha, and D. Diallo, "Improved Fault Diagnosis of Ball Bearings Based on the Global Spectrum of Vibration Signals," *IEEE Transactions on Energy Conversion*, vol. 30, no. 1, pp. 376–383, 2015.

[14] A. Mohammed, J. I. Melecio, and S. Djurović, "Stator Winding Fault Thermal Signature Monitoring and Analysis by In Situ FBG Sensors," *IEEE Transactions on Industrial Electronics*, vol. 66, no. 10, pp. 8082–8092, 2019.

[15] O. Janssens, R. Van de Walle, M. Loccufier, and S. Van Hoecke, "Deep Learning for Infrared Thermal Image Based Machine Health Monitoring," *IEEE/ASME Transactions on Mechatronics*, vol. 23, no. 1, pp. 151–159, 2018.

[16] O. Janssens, R. Schulz, V. Slavkovikj, K. Stockman, M. Loccufier, R. Van de Walle, and S. Van Hoecke, "Thermal image based fault diagnosis for rotating machinery," *Infrared Physics & Technology*, vol. 73, pp. 78–87, 2015. [Online]. Available: https://www.sciencedirect.com/science/article/pii/S1350449515002297

[17] T. Goktas, M. Zafarani, K. W. Lee, B. Akin, and T. Sculley, "Comprehensive Analysis of Magnet Defect Fault Monitoring Through Leakage Flux," *IEEE Transactions on Magnetics*, vol. 53, no. 4, pp. 1–10, 2017.

[18] E. Mazaheri-Tehrani and J. Faiz, "Airgap and stray magnetic flux monitoring techniques for fault diagnosis of electrical machines: An overview," *IET Electric Power Applications*, vol. 16, no. 3, pp. 277–299, 2022. [Online]. Available: https://ietresearch.onlinelibrary.wiley.com/doi/abs/10.1049/elp2.12157

[19] G. C. Stone, "Condition monitoring and diagnostics of motor and stator windings – A review," *IEEE Transactions on Dielectrics and Electrical Insulation*, vol. 20, no. 6, pp. 2073–2080, 2013.

[20] B. M. Ebrahimi, J. Faiz, and M. J. Roshtkhari, "Static-, Dynamic-, and Mixed-Eccentricity Fault Diagnoses in Permanent-Magnet Synchronous Motors," *IEEE Transactions on Industrial Electronics*, vol. 56, no. 11, pp. 4727–4739, 2009.

[21] J. Hang, S. Ding, X. Ren, Q. Hu, Y. Huang, W. Hua, and Q. Wang, "Integration of Interturn Fault Diagnosis and Torque Ripple Minimization Control for Direct-Torque-Controlled SPMSM Drive System," *IEEE Transactions on Power Electronics*, vol. 36, no. 10, pp. 11 124–11 134, 2021.

[22] J. Hang, H. Wu, S. Ding, W. Hua, and Q. Wang, "A DC-Flux-Injection Method for Fault Diagnosis of High-Resistance Connection in Direct-Torque-Controlled PMSM Drive System," *IEEE Transactions on Power Electronics*, vol. 35, no. 3, pp. 3029–3042, 2020.

[23] I. Petrov, D. Egorov, J. Link, R. Stern, S. Ruoho, and J. Pyrhönen, "Hysteresis Losses in Different Types of Permanent Magnets Used in PMSMs," *IEEE Transactions on Industrial Electronics*, vol. 64, no. 3, pp. 2502–2510, 2017.

[24] M. J. Melfi, S. Evon, and R. McElveen, "Induction versus permanent magnet motors," *IEEE Industry Applications Magazine*, vol. 15, no. 6, pp. 28–35, 2009.

[25] W. Cao, B. C. Mecrow, G. J. Atkinson, J. W. Bennett, and D. J. Atkinson, "Overview of Electric Motor Technologies Used for More Electric Aircraft (MEA)," *IEEE Transactions on Industrial Electronics*, vol. 59, no. 9, pp. 3523–3531, 2012.

[26] S.-Y. Jung, C. C. Mi, and K. Nam, "Torque Control of IPMSM in the Field-Weakening Region With Improved DC-Link Voltage Utilization," *IEEE Transactions on Industrial Electronics*, vol. 62, no. 6, pp. 3380–3387, 2015.

[27] D. Nguyen, R. Dutta, M. F. Rahman, and J. E. Fletcher, "Performance of a Sensorless Controlled Concentrated-Wound Interior Permanent-Magnet Synchronous Machine at Low and Zero Speed," *IEEE Transactions on Industrial Electronics*, vol. 63, no. 4, pp. 2016–2026, 2016.

[28] L. Zhong, M. Rahman, W. Hu, and K. Lim, "Analysis of direct torque control in permanent magnet synchronous motor drives," *IEEE Transactions on Power Electronics*, vol. 12, no. 3, pp. 528–536, 1997.

[29] P. Perera, F. Blaabjerg, J. Pedersen, and P. Thogersen, "A sensorless, stable V/f control method for permanent-magnet synchronous motor drives," *IEEE Transactions on Industry Applications*, vol. 39, no. 3, pp. 783–791, 2003.

[30] D. Mohanraj, J. Gopalakrishnan, B. Chokkalingam, and L. Mihet-Popa, "Critical Aspects of Electric Motor Drive Controllers and Mitigation of Torque Ripple—Review," *IEEE Access*, vol. 10, pp. 73 635–73 674, 2022.

[31] Z. Wang, J. Chen, M. Cheng, and K. T. Chau, "Field-Oriented Control and Direct Torque Control for Paralleled VSIs Fed PMSM Drives With Variable Switching Fre-

quencies," *IEEE Transactions on Power Electronics*, vol. 31, no. 3, pp. 2417–2428, 2016.

[32] F. Niu, B. Wang, A. S. Babel, K. Li, and E. G. Strangas, "Comparative Evaluation of Direct Torque Control Strategies for Permanent Magnet Synchronous Machines," *IEEE Transactions on Power Electronics*, vol. 31, no. 2, pp. 1408–1424, 2016.

[33] T. Geyer and S. Mastellone, "Model Predictive Direct Torque Control of a Five-Level ANPC Converter Drive System," *IEEE Transactions on Industry Applications*, vol. 48, no. 5, pp. 1565–1575, 2012.

[34] T. Geyer, G. Papafotiou, and M. Morari, "Model Predictive Direct Torque Control—Part I: Concept, Algorithm, and Analysis," *IEEE Transactions on Industrial Electronics*, vol. 56, no. 6, pp. 1894–1905, 2009.

[35] H. Yao, Y. Yan, T. Shi, G. Zhang, Z. Wang, and C. Xia, "A Novel SVPWM Scheme for Field-Oriented Vector-Controlled PMSM Drive System Fed by Cascaded H-Bridge Inverter," *IEEE Transactions on Power Electronics*, vol. 36, no. 8, pp. 8988–9000, 2021.

[36] K. H. NAM, *AC Motor Control and Electrical Vehicle Applications*, 2nd ed. CRC PRESS, 2018.

[37] J. G. Cintron-Rivera, A. S. Babel, E. E. Montalvo-Ortiz, S. N. Foster, and E. G. Strangas, "A simplified characterization method including saturation effects for permanent magnet Machines," in *2012 XXth International Conference on Electrical Machines*, 2012, pp. 837–843.

[38] A. S. Babel, J. G. Cintron-Rivera, S. N. Foster, and E. G. Strangas, "Evaluation of a Parameter Identification Method for Permanent Magnet AC Machines Through Parametric Sensitivity Analysis," *IEEE Transactions on Energy Conversion*, vol. 29, no. 1, pp. 240–249, 2014.

[39] A. Shinohara, Y. Inoue, S. Morimoto, and M. Sanada, "Direct Calculation Method of Reference Flux Linkage for Maximum Torque per Ampere Control in DTC-Based IPMSM Drives," *IEEE Transactions on Power Electronics*, vol. 32, no. 3, pp. 2114–2122, 2017.

[40] G. Liu, "Virtual Signal Injected MTPA Control for DTC Five-Phase IPMSM Drives," *Journal of Power Electronics*, p. 956–967, 2019.

[41] S.-H. Kim, "Chapter 2 - Control of direct current motors," in *Electric Motor Control*, S.-H. Kim, Ed. Elsevier, 2017, pp. 39–93. [Online]. Available: https://www.sciencedirect.com/science/article/pii/B9780128121382000027

[42] E. G. Strangas, G. Clerc, H. Razik, and A. Soualhi, *Applications and Specifics*. Wiley-IEEE Press, 2022, pp. 125–344.

[43] J. G. Cintron-Rivera, S. N. Foster, and E. G. Strangas, "Mitigation of turn-to-turn faults in fault tolerant permanent magnet synchronous motors," *IEEE Transactions on Energy Conversion*, vol. 30, no. 2, pp. 465–475, 2015.

[44] J. Zhao, X. Guan, C. Li, Q. Mou, and Z. Chen, "Comprehensive Evaluation of Inter-Turn Short Circuit Faults in PMSM Used for Electric Vehicles," *IEEE Transactions on Intelligent Transportation Systems*, vol. 22, no. 1, pp. 611–621, 2021.

[45] R. Z. S. Haddad, "Fault detection and identification in Permanent Magnet Synchronous Machines," Ph.D. dissertation, Michigan State University, 2016. [Online]. Available: http://ezproxy.msu.edu/login?url=https://www.proquest.com/dissertations-theses/fault-detection-identification-permanent-magnet/docview/1845322228/se-2

[46] P. F. C. Gonçalves, S. M. A. Cruz, and A. M. S. Mendes, "Online Diagnostic Method for the Detection of High-Resistance Connections and Open-Phase Faults in Six-Phase PMSM Drives," *IEEE Transactions on Industry Applications*, vol. 58, no. 1, pp. 345–355, 2022.

[47] O. Thorsen and M. Dalva, "A survey of faults on induction motors in offshore oil industry, petrochemical industry, gas terminals, and oil refineries," *IEEE Transactions on Industry Applications*, vol. 31, no. 5, pp. 1186–1196, 1995.

[48] Y. Park, D. Fernandez, S. B. Lee, D. Hyun, M. Jeong, S. K. Kommuri, C. Cho, D. Diaz Reigosa, and F. Briz, "Online Detection of Rotor Eccentricity and Demagnetization Faults in PMSMs Based on Hall-Effect Field Sensor Measurements," *IEEE Transactions on Industry Applications*, vol. 55, no. 3, pp. 2499–2509, 2019.

[49] J. Hong, S. Park, D. Hyun, T.-j. Kang, S. B. Lee, C. Kral, and A. Haumer, "Detection and Classification of Rotor Demagnetization and Eccentricity Faults for PM Synchronous Motors," *IEEE Transactions on Industry Applications*, vol. 48, no. 3, pp. 923–932, 2012.

[50] M. Zhu, W. Hu, and N. C. Kar, "Torque-Ripple-Based Interior Permanent-Magnet Synchronous Machine Rotor Demagnetization Fault Detection and Current Regulation," *IEEE Transactions on Industry Applications*, vol. 53, no. 3, pp. 2795–2804, 2017.

[51] M. Ojaghi and J. Faiz, "An experimental/simulation investigation to mixed eccentricity fault diagnosis of induction motors under DTC," in *2014 IEEE International Conference on Industrial Technology (ICIT)*, 2014, pp. 143–148.

[52] S. Cruz and A. Cardoso, "Diagnosis of stator inter-turn short circuits in DTC induction motor drives," *IEEE Transactions on Industry Applications*, vol. 40, no. 5, pp. 1349–

1360, 2004.

[53] A. Berzoy, O. A. Mohammed, and J. Restrepo, "Analysis of the impact of stator interturn short-circuit faults on induction machines driven by direct torque control," *IEEE Transactions on Energy Conversion*, vol. 33, no. 3, pp. 1463–1474, 2018.

[54] I. M. Alsofyani, N. R. N. Idris, and K.-B. Lee, "Dynamic Hysteresis Torque Band for Improving the Performance of Lookup-Table-Based DTC of Induction Machines," *IEEE Transactions on Power Electronics*, vol. 33, no. 9, pp. 7959–7970, 2018.

[55] S. Mathapati and J. Bocker, "Analytical and Offline Approach to Select Optimal Hysteresis Bands of DTC for PMSM," *IEEE Transactions on Industrial Electronics*, vol. 60, no. 3, pp. 885–895, 2013.

[56] X. Chen, J. Hu, K. Chen, and Z. Peng, "Modeling of electromagnetic torque considering saturation and magnetic field harmonics in permanent magnet synchronous motor for HEV," *Simulation Modelling Practice and Theory*, vol. 66, pp. 212–225, 2016. [Online]. Available: https://www.sciencedirect.com/science/article/pii/S1569190X16000307

[57] A. Jidin, N. Idris, and A. Yatim, "Study on Stability and Performances of DTC Due to Stator Resistance Variation," in *2007 5th Student Conference on Research and Development*, 2007, pp. 1–6.

[58] G. Buja and R. Menis, "Steady-State Performance Degradation of a DTC IM Drive Under Parameter and Transduction Errors," *IEEE Transactions on Industrial Electronics*, vol. 55, no. 4, pp. 1749–1760, 2008.

[59] S. Moon, J. Lee, H. Jeong, and S. W. Kim, "Demagnetization Fault Diagnosis of a PMSM Based on Structure Analysis of Motor Inductance," *IEEE Transactions on Industrial Electronics*, vol. 63, no. 6, pp. 3795–3803, 2016.

[60] W. T. Thomson, *Motor Current Signature Analysis for Induction Motors*. John Wiley & Sons, Ltd, 2016, ch. 1, pp. 1–37. [Online]. Available: https://onlinelibrary.wiley.com/doi/abs/10.1002/9781119175476.ch1

[61] A. G. Espinosa, J. A. Rosero, J. Cusidó, L. Romeral, and J. A. Ortega, *IEEE Transactions on Energy Conversion, title=Fault Detection by Means of Hilbert–Huang Transform of the Stator Current in a PMSM With Demagnetization*, vol. 25, no. 2, pp. 312–318, 2010.

[62] C. D. Untaroiu and T. J. Adam, "Performance-Based Classification of Occupant Posture to Reduce the Risk of Injury in a Collision," *IEEE Transactions on Intelligent Transportation Systems*, vol. 14, no. 2, pp. 565–573, 2013.

[63] I. Ibraheem, "Linear and Quadratic Classifier to Detection of Skin Lesions "Epicuta-

neus"," in *2011 5th International Conference on Bioinformatics and Biomedical Engineering*, 2011, pp. 1–5.

[64] M. Z. Ali, M. N. S. K. Shabbir, X. Liang, Y. Zhang, and T. Hu, "Machine Learning-Based Fault Diagnosis for Single- and Multi-Faults in Induction Motors Using Measured Stator Currents and Vibration Signals," *IEEE Transactions on Industry Applications*, vol. 55, no. 3, pp. 2378–2391, 2019.

[65] C. Cortes and V. Vapnik, " Support-vector networks," *Machine Learning*, p. 273–297, 1995.

[66] G. Oluchi Anyanwu, C. I. Nwakanma, J.-M. Lee, and D.-S. Kim, "Optimization of RBF-SVM Kernel Using Grid Search Algorithm for DDoS Attack Detection in SDN-Based VANET," *IEEE Internet of Things Journal*, vol. 10, no. 10, pp. 8477–8490, 2023.

[67] C.-C. Chang and C.-J. Lin, "LIBSVM: A library for support vector machines," *ACM Transactions on Intelligent Systems and Technology*, vol. 2, pp. 27:1–27:27, 2011, software available at http://www.csie.ntu.edu.tw/ cjlin/libsvm.

[68] K. K. Prabhakar, C. U. Reddy, A. K. Singh, and P. Kumar, "Inverter switching frequency prediction in DTC of induction motor drive for an EV drivetrain," in *2017 IEEE Power & Energy Society General Meeting*, 2017, pp. 1–4.

[69] S. Moon, H. Jeong, H. Lee, and S. W. Kim, "Detection and Classification of Demagnetization and Interturn Short Faults of IPMSMs," *IEEE Transactions on Industrial Electronics*, vol. 64, no. 12, pp. 9433–9441, 2017.

[70] A. Shinohara, Y. Inoue, S. Morimoto, and M. Sanada, "Maximum Torque Per Ampere Control in Stator Flux Linkage Synchronous Frame for DTC-Based PMSM Drives Without Using q-Axis Inductance," *IEEE Transactions on Industry Applications*, vol. 53, no. 4, pp. 3663–3671, 2017.

[71] M. Drif and A. J. M. Cardoso, "Stator Fault Diagnostics in Squirrel Cage Three-Phase Induction Motor Drives Using the Instantaneous Active and Reactive Power Signature Analyses," *IEEE Transactions on Industrial Informatics*, vol. 10, no. 2, pp. 1348–1360, 2014.